Cooperative Manipulation Using a Magnetically Navigated Microrobot and a Micromanipulator

by

Xiaodong Zhang

A thesis
presented to the University of Waterloo
in fulfillment of the
thesis requirement for the degree of

Doctor of Philosophy

in

Mechanical and Mechatronics Engineering

Waterloo, Ontario, Canada, 2017

Examining committee Membership

The following served on the Examining Committee for this thesis. The decision of the Examining Committee is by majority vote.

External Examiner	Name: Gabor Fichtinger Title: Professor
Supervisor	Name: Mir Behrad Khamesee Title: Professor
Internal Member	Name: Jan P. Huissoon Title: Professor
	Name: James Tung Title: Assistant Professor
Internal-external Member	Name: John Mcphee Title: Professor

Author's Declaration

This thesis consists of material all of which I authored or co-authored: see Statement of Contributions included in the thesis. This is a true copy of the thesis, including any required final revisions, as accepted by my examiners.

I understand that my thesis may be made electronically available to the public.

Statement of Contributions

The material in Chapter 3 is related to the published journal paper that I worked with Dr. Mehrtash. The work is published in IEEE/ASME Transactions on Mechatronics in 2016. The title of the publication is Dual-axial motion control of a magnetic levitation system using hall-effect sensors.

In this work, I designed the experiment, analyzed the data, and prepared the manuscript. Dr. Mehrtash design the experiment and reviewed the manuscript. The work in Chapter 3 is the continuous research of Dr. Mehrtash's idea in: Motion control of a magnetically levitated microrobot using magnetic flux measurement. This work focuses on the 1D navigation of the magnetically levitated microrobot using magnetic flux measurement. This work was published in 2012 on Microsystem Technologies.

Abstract

The cooperative manipulation of a common object using two or more manipulators is a popular research field in both industry and institutions. Different types of manipulators are used in cooperative manipulation for carrying heavy loads and delicate operations. Their applications range from macro to micro. In this thesis, we are interested in the development of a novel cooperative manipulator for manipulation tasks in a small workspace. The resultant cooperative manipulation system consists of a magnetically navigated microrobot (MNM) and a motorized micromanipulator (MM). The MNM is a small cylinder permanent magnet with 10mm diameter and 10mm height. The MM model is MP-285 which is a commercialized product. Here, the MNM is remotely controlled by an external magnetic field. The property of non-contact manipulation makes it a suitable choice for manipulation in a confined space.

The cooperative manipulation system in this thesis used a master/slave mechanism as the central control strategy. The MM is the master side. The MNM is the slave side. During the manipulation process, the master manipulator MM is always position controlled, and it leads the object translation according to the kinematic constraints of the cooperative manipulation task. The MNM is position controlled at the beginning of the manipulation. In the translation stage, the MNM is switched to force control to maintain a successful holding of the object, and at the same time to prevent damaging the object by large holding force. Under the force control mode, the motion command to the MNM is calculated from a position-based impedance controller that enforces a relationship between the position of the MNM and the force.

In this research, the accurate motion control of both manipulators are firstly studied before the cooperative manipulation is conducted. For the magnetic navigation system, the magnetic field in its workspace is modeled using an experimental measurement data-driven technique. The developed model is then used to develop a motion controller for navigating of a small cylindrical permanent magnet. The accuracy of motion control is reached at $20\mu m$ in three degrees of freedom. For the motorized micromanipulator, a standard PID controller is designed to control its motion stage. The accuracy of the MM navigation is 0.8 μm.

Since the MNM is remotely manipulated by an external magnetic field in a small space, it is challenging to install an on-board force sensor to measure the contact force between the MNM and the object. Therefore, a dual-axial off-board force determination mechanism is proposed. The force is determined according to the linear relation between the minimum magnetic potential energy point and the real position of the MNM in the workspace.

For convenience, the minimum magnetic potential energy point is defined as the B_{max} in the literature. In this thesis, the dual-axial B_{max} position is determined by measuring the magnetic flux density passing through the workspace using four Hall-effect sensors installed at the bottom of an iron pole-piece. The force model is experimentally validated in a horizontal plane with an accuracy of 2 μN in the x- and y- direction of horizontal planes.

The proposed cooperative manipulator is then used to translate a hard-shell small object in two directions of a vertical plane, while one direction is constrained with a desired holding force. During the manipulation process, a digital camera is used to capture the real-time position of the MNM, the MM end-effector, and the manipulated object.

To improve the performance of force control on the MNM, the proposed dual-axial force model is used to examine the compliant force control of the MNM while it is navigated to contact with uncertain environments. Here, uncertain refers to unknown environmental stiffness. An adaptive position-based impedance controller is implemented to estimate the stiffness of the environment and the contact force. The controller is examined by navigating the MNM to push a thin aluminum beam whose stiffness is unknown.

The studied cooperative manipulation system has potential applications in biomedical microsurgery and microinjection. It should be clarified that the current system setup with 10mm $\times$ 10 mm MNM is not proper for this micromanipulation. In order to conduct research on microinjection, the size of the MNM and the end-effector of the MNM should be down-scaled to micrometers. In addition, the navigation accuracy of the MNM should also be improved to adopt the micromanipulation tasks.

Acknowledgements

I would like to thank my supervisor Professor Mir Behrad Khamesee for his continuous support and guidance during my PhD study and the completion of this thesis. Thanks to my colleagues Moein Mehrtash, Yuze Huang, Ehsan Asadi, Mohammad Mashagbeh, Heng Zhang, Thamir Al-Dulaimi, Roberto Ribeiro, David M. B. Dombroski, and Pratik Patel. I want to thank you all for the help in my research and life in the last four and a half years.

I would also like to thank the technical staff members in the Mechanical and Mechatronics engineering department for their support. Special thanks to Neil Griffett and Martha Morales for their assistance in my research.

I would like to thank my parents, and my sister and her two lovely daughters. They always encourage me and give me their best wishes.

Finally, I have to thank my wife Juan, and my cute daughter Xixi. They always stand behind me and cheer me up. My life is full of sunshine because of them.

Table of Contents

List of Tables

List of Figures

Chapter 1

Introduction

1.1 Introduction to Cooperative operation

Cooperative manipulation involves using two or more manipulators to conduct complex tasks such as carrying heavy loads and delicate manipulation those are difficult to accomplish by using a single manipulator.

In the last two decades, there has been a growing interest in research on cooperative manipulation. The limited working ability of a single robot promotes the research boom in multi robots or multi-arm robot manipulation. Many tasks that are very difficult or impossible to be done by a single robot could be fulfilled by the cooperative work of two or more manipulators. Such tasks include lifting/moving heavy or large loads, assembling parts, handling flexible objects, and operating in multiple degrees of freedom. Manipulation of objects in hazardous environments that are humanly inaccessible also benefits from the group work of multi-robots. Another popular application is the cooperative manipulation of a mechanical manipulator with people to help reduce human labor and to improve the efficiency of a single person.

Different types of robots/manipulators have been studied to accomplish specific cooperative manipulation tasks. We classify robots for cooperative tasks as fixed-base robot and moving-base robot. Fixed-base means the base of manipulators cannot be moved while the end-effector is executing commands. Arm robots belong to this type of robot. Moving-base robot means that the location of the whole body of the robot is changing when the robot is working. Mobile and aerial robots can be classified as moving-based robots.

Successful multi-manipulator manipulation systems exist both in industry and labs using arm manipulators [30] [63], mobile robots [106] [102], and aerial robots [31] [51].

Their applications range from the macro domain to the micro domain. Among them, micromanipulation and micro assembly with micro scale position and force accuracy are challenges. In [76], transportation of a relatively large object was done by a combination of four wheeled robots. In [68], manipulation and transportation of a common object in air was done by three aerial robots. In this research, the object was tied to aerial robots using three sections of cable and was capable of moving in five degrees of freedom. In [8], a dual-arm robot station was used to manipulate a large size object in a cooperative manner. The contribution of this research is the ability to work with humans and the capability of dealing with object size uncertainty. A microsurgical platform was proposed in [6] to assist eye surgery at Johns Hopkins University. This micro surgical platform was composed of cooperatively working EyeRobot2 and a da Vinci Master Manipulator for remote control by means of visualization feedback. Figure 1.1 shows examples of cooperative manipulation.

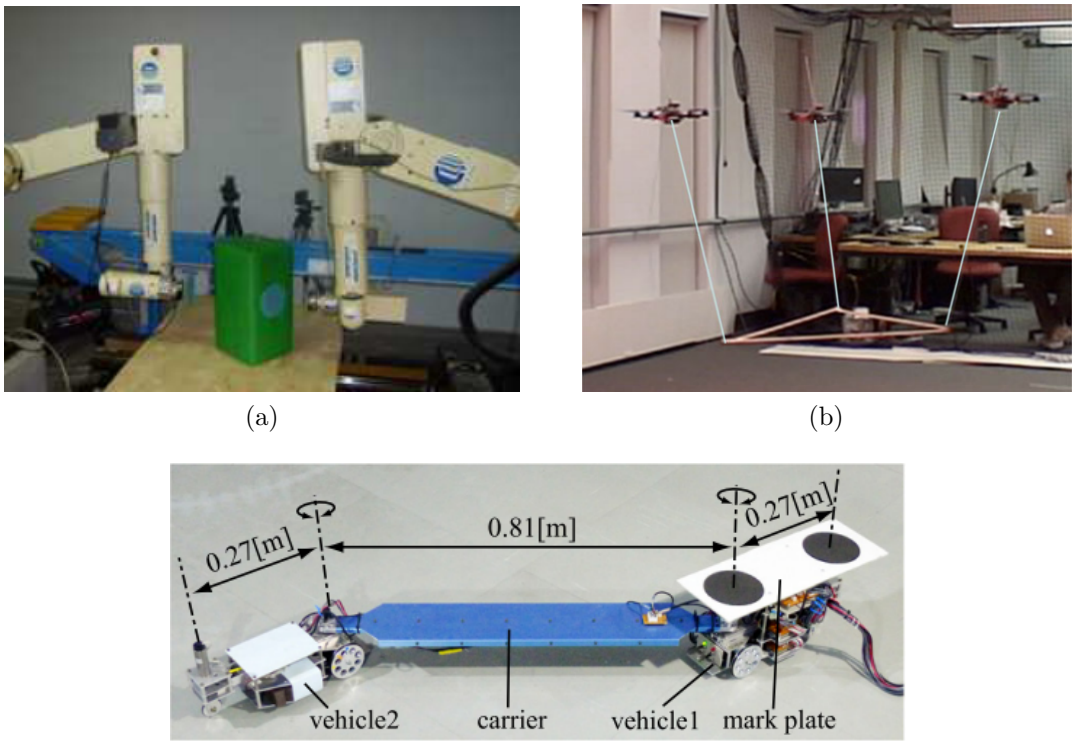

(a) (b)

(c)

Figure 1.1: Different cooperative manipulators a) arm robots [11], b) aerial robots [51] , c) car like robots [106]

Generally, cooperative manipulation is the manipulation of common objects using two or more manipulators. The manipulation work mainly focuses on moving an object from its original location to a desired position/orientation with special requirements: for example, tracking a special motion trajectory, and protecting the manipulated object from being damaged by the environment and other agents.

A central control scheme is the key to cooperative manipulation. There are several control mechanisms for the cooperative operation mechanism using multiple arm robots. They are the master/slave control, the external force control, and the internal force control. In the early stage of research on cooperative manipulation, the master/slave strategy was mostly applied [79] [48]. In the master/slave approach, the master manipulators are position-controlled and are commanded the desired motion trajectory of the held object. The slave manipulators are force-controlled to follow the motion of the object, while at the same time maintain a stable holding of the object. This approach does not take the environment interaction and the system dynamic into account. It can easily produce a higher external force, so it is limited to free-space operation tasks.

However, cooperative manipulations are not merely limited to free space. In many operation processes, the held object will contact with its external environment and encounter a large contact force if the planned trajectory is not consistent with the geometry of the environment. Then the challenge of cooperative manipulation is following the desired motion trajectory of the held object and at the same time protecting the object from being damaged by the large contact force between the object and its environments. Hybrid position/force control [84] is one solution that allows the object to contact with a controlled contact force. This technique has been applied to many cooperative manipulation studies [69] [107]. In [99], the author implemented this control mechanism to handle one constrained object by taking into consideration the dynamics of the object. The motion control strategy was applied in the tangent direction of the constrained surface, while compliant force control was implemented in the normal direction of the constrained surface. In [35], the author proposed combining the intelligent adaptive algorithm with a hybrid position/force technique to control cooperative manipulators. The advantage of the new method is that a precise dynamic model of the system is not required. The hybrid position/force control method is not as attractive as impedance control, which will be presented in the following, because this technique requires dividing the space into force- and position control sub-spaces. If the operating surface is not regular, the control system needs to keep switching coordinate system parameters at the object space, and the overall system becomes very complex.

When a manipulator system interacts with its external environment, large contact forces and moments can be avoided by enforcing a compliant behavior of the system.

Impedance control schemes have been proposed in cooperative manipulation to control the object-environment contact force [86]. By implementing impedance control, the object-environment interaction is complaint in all directions. At the manipulated object level, impedance control specifies a dynamic response of the system by enforcing the relation between the force on the object and its position. At the manipulators' end effector level in cooperative manipulation, an internal force exists between end effectors and the held object, but the position control scheme cannot regulate the internal force. In [9], the author proposed using impedance control to smooth the contact between the robot endpoint and the held object. The controller enforces a relation between the velocity of each manipulator and the internal force on the manipulated object. Impedance control on both internal- and external force was studied in [11]. There are two different type of impedance control: force-based impedance control and position-based impedance control. The force-based impedance controller is good for manipulators that have torque-controlled joint servomotors. For manipulators with only position-controlled joints, the position-based impedance controller is a better choice. The position-based impedance is very simple to implement, because it does not require the dynamics model of manipulators and environment.

In recent decades, there has been a lot of progress in the development of computer science and manufacturing, as well as in robotic control theories. This progress encourages researchers to implement advanced intelligent control systems with cooperative manipulation. Those control systems include but are not limited to fuzzy logic, parameter estimation, and neural networks. In [32], a distributed strategy is proposed in a multi-robot manipulation system to estimate the kinematic and inertial parameters of an unknown manipulated object. In [82], an adaptive controller based on on-line neural network learning was proposed for coordinated control of a multiple manipulator system manipulating a single rigid object. The neural network was employed to learn the existing unknown dynamics of the manipulators and the object. The position tracking and internal force on the object are controlled based on the learned dynamic model. In [35], similar work was done using a fuzzy logic algorithm.

In this research, we proposed using a magnetically navigated microrobot and a motorized micromanipulator to translate small size objects in a cooperative manner. A simplified schematic of the system is shown in figure 1.2. The motorized micromanipulator has a tip end-effector that is similar to an arm manipulator. The end-effector of the magnetically navigated microrobot works with the micromanipulator to manipulate an object as if there is an unseen arm holding the end effector. A simple master/slave strategy is introduced to the cooperative manipulation system.

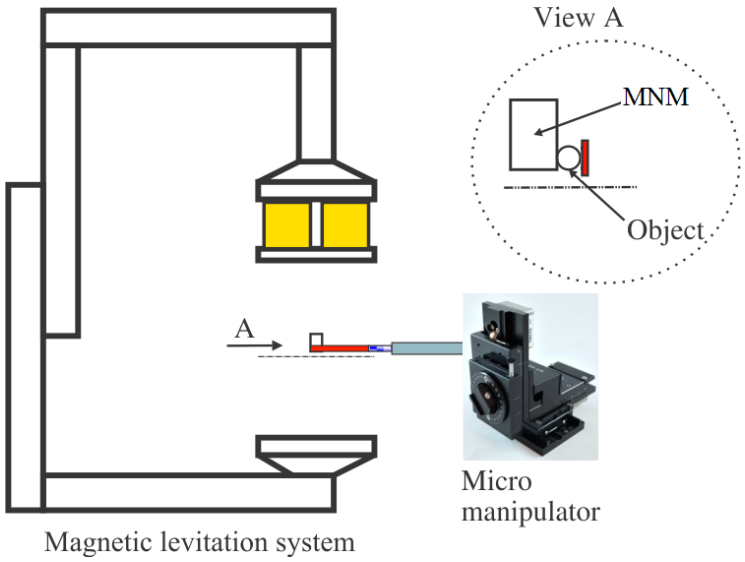

Figure 1.2: simplified schematic of the cooperative manipulation system in this research

1.2 Introduction to Magnetic Levitation

Levitation is a technique that uses different mediums to remotely manipulate an object. The main advantage of levitation is neglecting the mechanical connection between the manipulated object and its driving unit. Different techniques have been studied to realize the levitation of an object, such as acoustic levitation [101], air flow levitation [33], and magnetic levitation [78]. Among these, magnetic levitation technology has been widely studied. The fundamental principle of magnetic levitation is transferring the magnetic energy of a source unit into the kinematic energy of the manipulated object. The energy is transferred remotely from a magnetic energy source unit to the end-effector by means of magnetic flux. The magnetic source can be an electromagnet or a permanent magnet. Magnetic levitation has a promising future, because it has the benefit of isolation from external vibration, elimination of friction, no backlash, and it is wireless accessible. Up to now, magnetic levitation technology has been applied in vast areas. Such areas include Maglev transportation [38][60], wind tunnel testing [25], magnetic bearings [56], energy storage[96], academic education [110], medical surgery [14], and cell cultivation [95].

Magnetic levitation can be categorized into four different types based on the materials of the objects used in the levitating. Generally, the materials are classified into diamagnetic material, paramagnetic material, ferromagnetic material, and superconductor material according to the different relative permeability of the materials with respect to free space.

Therefore, magnetic levitation includes diamagnetic levitation [65][94], paramagnetic levitation, ferromagnetic levitation, and superconducting levitation[81][83]. Figure 1.3 shows the levitation using different techniques. Diamagnetic material has a relative permeability of $\mu < 0$. The relative permeability is $0 < \mu < 1$ for paramagnetic materials, and is $\mu > 1$ for ferromagnetic materials. Superconductors have zero relative permeability and can sustain unlimited current. In real applications, the most used material in magnetic study is ferromagnetic material. Diamagnetic levitation is not widely studied because a much stronger field is required to levitate the same quantity of ferromagnetic materials. Therefore, it is not economic. Superconducting levitation is a booming technique. However, the strict requirement of extremely low temperature to let materials have superconducting properties limits its application in real industries. Ferromagnetic and paramagnetic levitation, compared with the other two types, are relatively economic and easier in the sense of realization. For example, soft iron, a ferromagnetic material, can be easily magnetized and has the ability to enhance a magnetic field significantly, which decreases the current in electromagnets to produce the same strength of magnetic field. Permanent magnets have a relative permeability that is slightly greater than 1, but very strong magnetic energy can be stored inside. In this research, the magnetic energy is produced by six pairs of electromagnets with a soft iron core. These electromagnets are connected by an iron yoke and an iron pole-piece. The levitated robot is a small permanent magnet.

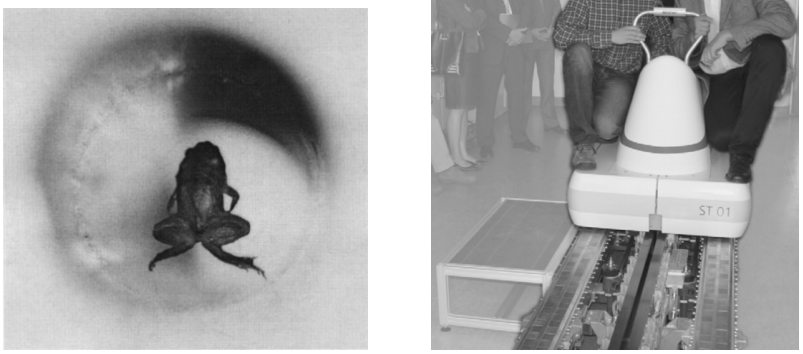

(a) (b)

Figure 1.3: Different magnetic levitations a) a floating frog which uses the principle of diamagnetic levitation [94], b) superconducting levitation [88]

1.2.1 Diamagnetic Levitation

Diamagnetic materials are considered nonmagnetic materials. Such substances include water, protein, DNA, wood, and graphite [65]. When a diamagnetic material is placed inside an external magnetic field, the induced current inside the diamagnetic material produces an induced magnetic field that is opposed to the existing external magnetic field. The interaction between the induced magnetic field and the source external magnetic field generates magnetic force to levitate the diamagnetic material.

In [94], the author explains the principle of the stable levitation of diamagnetic material in an external magnetic field produced by either electromagnets or permanent magnets. Diamagnetic levitation is contrary to Enshaw's law, which states that a single object cannot be levitated by a single magnet, because the minimum potential energy point is on the magnetic source body. However, the induced magnetic moment in diamagnetic materials produces a repelling force which moves the diamagnetic materials to the local minimum potential energy point of a plane. If this repelling force is strong enough to compensate for the gravity force, then levitation is achievable. This research also presents the theory of levitation of a magnet source (permanent magnet) between two graphite disc plates.

Electrode levitation has mostly been used in bioengineering for cell manipulation and droplet guiding. However, diamagnetic levitation has outstanding advantages over electrode levitation in these fields. Diamagnetic levitation is highly efficient for magnetic MEMS in the sense of cost effectiveness and no heat generation in the samples that are manipulated. Research has been conducted on validating the principle of micromanipulation using diamagnetic levitation. In [23], the author proposed using diamagnetic levitation for micro-positioning and trapping of diamagnetic micro-sized particles and micro-droplets. In this research, the levitation of micro droplets made of water, ethanol, and oil was achieved within the 1.6 mm bore of a cylindrical magnet and in micro machined bulk magnets.

1.2.2 Superconducting Levitation

In the real application of magnetic levitation using electromagnets, there is a conflict between the energy saving issue and the obtaining of a strong magnetic field. To produce a stronger field, more current is required to be supplied to conductors. However, higher current causes more heat waste inside the conductor. A superconductor is a perfect choice to balance both the requirements of energy saving and strong magnetic field production. Since superconductors have no electric resistance, they do not have heat loss and consume no electrical energy. Theoretically, the current in the superconductor can be unlimited. Therefore, it is possible to produce a very strong magnetic field as long as it is not saturated.

A very important application of superconducting levitation is the superconducting maglev train. This technology has been used in Japan, Germany, and China on high-speed trains. The maglev train is popular, because it eliminates friction between the train wheel and the rail tracks. In [81], the superconducting maglev train was introduced. On the train, there are superconducting magnets made from coils of superconducting wires. The superconducting magnets have a very strong magnetic field and make the propulsion of a huge train easier with less energy consumption. However, there ire also drawbacks for the superconducting maglev train. For example, the condition for making materials that have superconducting properties at a room temperature is challenging.

Superconductors are perfect diamagnetic materials because they reject any magnetic flux passing through. Therefore, superconductors can be used to levitate a small permanent magnet above them. The levitation is stabilized at any location. Research has been conducted on micromanipulation using superconducting levitation. Jose in [83] presents a new precise positioner using a superconducting technique for non-contact manipulation in cryogenic environments. The device is composed of two disc superconductors, one permanent bar magnet, two air-core electromagnets, and one optical position sensor. The superconductors provide initial levitation. The electromagnets work synchronously to adjust the position of the levitating permanent magnet to the desired position with the accuracy of $1\mu m$.

1.2.3 Ferromagnetic Levitation

Ferromagnetic levitation is one of the best choices for most applications because it addresses the issue of cost and it is easily implemented. Ferromagnetic materials have relative permeability $\mu > 1$. We can easily find a metal that has this special property. Numerous studies have been done on ferromagnetic theory and the control of ferromagnetic levitation. Therefore, rich knowledge is available for new applications. Ferromagnetic materials induce current to enhance the external magnetic fields. Because the induced current produces an induced magnetic field in the materials in the same direction as the external magnetic field, it is an attractive force between the magnetic field source and the ferromagnetic materials. The permanent magnet is a special ferromagnetic material. Permanent magnets are pre-magnetized by a strong magnetic field. They have high magnetic flux density on the surfaces. Placing permanent magnets in an external field does not change their magnetic moments.

Based on its different applications, ferromagnetic levitation can be classified into magnetic bearing, planar manipulator, magnetic navigation, and capsule drug delivery. Figure 1.4 shows examples of ferromagnetic levitation.

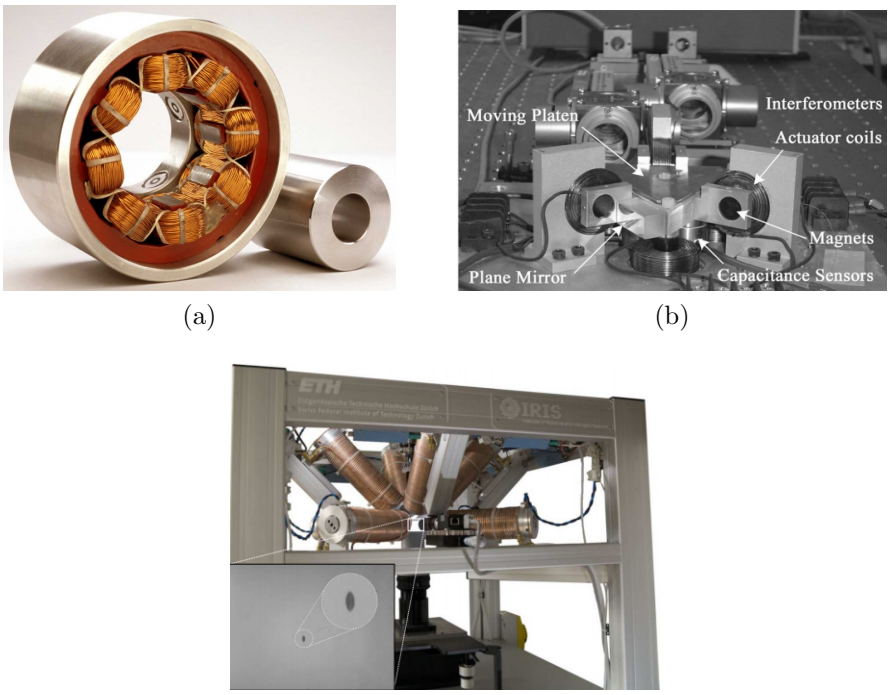

(a) (b)

(c)

Figure 1.4: Different ferromagnetic levitation applications a) magnetic bearing [1], b) magnetic planar positioner [90], c) magnetic navigation [59]

1.2.3.1 Magnetic Bearing

To overcome the drawback of mechanical wear, which is a common feature of regular mechanical bearings, a magnetic bearing was proposed. A magnetic bearing uses magnetic force to support the rotor. There is no contact between the rotor and the support. Therefore, there is no mechanical friction. The contactless property makes it a suitable solution for a super high-speed rotational machine.

Two types of magnetic bearings have been mostly studied in the past decades. They are the passive magnetic bearing and the active magnetic bearing. In the passive magnetic bearing, permanent magnets are used as magnetic energy source. There is no need to control and stabilize the rotor. Its stabilization is realized by carefully designing the structures of the stators and rotors. In an active magnetic bearing, the magnetic energy source is electromagnets. By implementing a closed-loop controller in the system and using rotor position feedback, the levitation can be actively stabilized.

In a passive magnetic bearing, both axial and radial magnetized permanent magnets are used in designing a system. In [93], the authors designed a radial passive magnetic bearing flywheel using radially magnetized permanent magnets. In this study, to stabilize the radial magnetic bearing, two radially magnetized permanent magnet arrays were mounted on the stator, and two radially magnetized permanent magnet arrays were mounted on the rotor. To have sufficient stiffness and damping built in the passive magnetic bearing, a special magnet array is designed and a jewel bearing is installed at the end of the rotor. In [39], the author proposed an axial passive magnetic bearing. This magnetic bearing has the ability to take loads both in axial and radial directions. It has axial magnetized permanent magnets on the stator and the rotor. In addition, it has iron poles to increase the magnetic field at the poles. The limitation of a passive magnetic bearing in real applications is the lack of damping. An active magnetic bearing, on the contrary, has the ability to provide high damping[29].

An active magnetic bearing (AMB) is an important element in high-speed equipment, such as flywheel systems, high-speed drives, turbo molecular pumps, and compressors. In general, an active magnetic bearing is composed of electromagnet coils, a ferromagnetic rotor, a power amplifier, a position controller, and position detection system. Like the passive magnetic bearing, there are both axial and radial active magnetic bearings. The most commonly used active magnetic bearing in industry has 8-poles [70] [21]. The advantage of using 8 poles is that the magnetic flux is decoupled. However, the greater number of poles result in more copper loss, a complex cooling system, and less space for sensor installation. Therefore, 6-pole [49], 4-pole [2], and a minimum of 3-pole [21] active magnetic bearings were developed. Although the limited space problem can be improved by using fewer poles structurally, the coupled magnetic flux in fewer poles structurally makes the control of the system more difficult. Besides the studies on the structural design, another very important aspect of active magnetic bearing research is the stabilization of levitation. The active magnetic bearing system is inherently unstable and highly nonlinear. Feedback control is necessary for stable and successful levitation, especially in a very high-speed situation. A large number of studies have been done on control of active magnetic bearings by applying classical and advanced control strategies such as PID control [16], sliding-mode control [22], ANFIS control [19], nonlinear smooth feedback control [20], and neural-fuzzy control [24]. A recent research topic on active magnetic bearings is self-sensing control. There are mainly two ways to eliminate position sensors from the control system. One is applying a state observer based on coil current measurement. The rotor position is estimated by using a state observer. The other is a coil inductance induced position estimation. By supplying high-frequency signals to coils, the position change of the rotor can be measured from the change of coil inductance caused by rotor displacement [85].

1.2.3.2 Planar positioner

Modern industry urges the research and the development of higher accuracy and multi-degree-of-freedom planar manipulator/positioners for delicate operation missions. The general solutions to this demand are designing lead-screw and piezoelectric actuators. Although there are many successful applications of these technologies, the disadvantages of friction and backlash make mechanical contact type manipulators not the best choice in micro/nano scale manipulation tasks. However, the magnetic levitation stages with the properties of no mechanical contact and higher positioning resolution are attracting more and more attention of researchers and companies[104] [90] [114].

Kim in [57] proposed a planar stage using four 3-phase linear permanent-magnet motors for the potential application of photo lithography A Halbach permanent magnet array was installed on the levitator to produce a levitation force and avoid a heating effect on the levitator. The system has 6-DOF motion ability. The translation range is 50mm $\times$ 50 mm $\times$ 400 μm. The orientation range with respect to the axis of the coordinate system is 600 μrad. This planar levitation system has a 5 nm rmse accuracy in translation motion and 0.025 μrad rmse in orientation motion.

In [17], a planar maglev positioning system was proposed for micromanipulation. The stator of the system was composed of 6 coils, in which three vertical coils were designed for vertical levitation and three horizontal coils were used to realize horizontal motion. Corresponding to the coils on the stator, 6 permanent magnets were installed on the levitator with the purpose of reducing mover mass and realizing non-contact manipulation. Each permanent magnet was located inside a coil. The levitator could be moved in 6-DOF in the Cartesian coordinate system. Since the system was designed to act as a planar table, only 7 mm $\times$ 7 mm translation range with 10 μm accuracy was studied in the paper, while the stability of translation in vertical direction orientation with respect to the three axes was discussed at the same time.

In [80], the author presented a new planar positioner using a magnetic levitation technique. Different from conventional planar levitation platforms, the new design considered levitating a group of coils horizontally over a permanent-magnet array. NdFeB magnets were placed in a special Halbach manner to produce concentrated magnetic field in x-, y-, and z-directions. The system had translation ranges of 15.4 cm in the x-direction and 20.32 cm in the y-direction with 8 μm accuracy. The rotation range and accuracy with respect to z-direction were 12.03° and 100 μrad.

1.2.3.3 Magnetic Navigation

Magnetic navigation is such a technology that a levitating object can be guided by an external magnetic field in hazardous and human inaccessible environments. The general investigation of designing a magnetic navigation system includes: a) Design a platform as an external magnetic field to transfer a magnetic energy source into the kinematic energy of a moving object - the scale of levitation robots range from macro to micro; b) Design robots for specific tasks, for instance, medical surgery robots [43] [37] and remote actuator [92]; c) explore control systems to realize active, stable, and multi degree of freedom control on a levitating robot using elaborate algorithms.

Khamesee in [54] proposed a magnetic levitation system to manipulate a microrobot in free space. The system used four pairs of electromagnets, a special pole-piece, and an iron yoke to produce the desired gradient magnetic field shape in the working volume. On the microrobot, were four micro scale permanent magnets distributed in a circular distribution to support the microrobot. The microrobot used a shape memory alloy wire as a micro hand to fulfill such tasks as pick and place. In the study, a classical PID controller was applied to realize a 3-DOF translation of the microrobot, and an adaptive controller was used for payload uncertainty operation. Laser position sensors were employed to measure the real-time position of the robot. The measured position was then fed back to the control system for stability control.

One challenge in the research of magnetic levitation systems is the multi-degree-freedom operation of a levitating object; specifically it is very difficult to realize free orientation of the object. The common solution to this challenge is applying an extra magnetic energy source for extra degrees of freedom. However, this not only increases the cost of the overall system, but also increases the complexity and limits the working ability of the system by reducing the working space.

An eye surgery micromanipulation system was presented in [59]. The platform was composed of six iron-core electromagnets, but without a yoke among electromagnets, and a micro size surgery robot. The electromagnets were installed in a hemisphere manner to generate a hemisphere shaped linear magnetic field in the working envelope. The microrobot was composed of two magnetized, electroplated, planar pieces, and could be operated in 5-DOF with 3-DOF translation and 2-DOF orientation. This system used a digital camera to capture the location of the operated microrobot. The system has been commercialized.

In [77], Muneaki presented a technology of using a planar electromagnet array to levitate a multi-permanent-magnet round shape robot. The robot could be manipulated in 6-DOF, with an unlimited rotation range in all directions. A motion tracker was used to track the location of magnets on the robot. Since there were multiple permanent magnets, a careful

magnet installation strategy was considered to avoid a tracking block of the robot using the motion tracker. The author also determined the minimum number of coils for reliable levitation based on the experimental result.

A potential application of magnetic navigation is translating inside nontransparent environments, such as a human body or a nontransparent box. The challenge of operating in these environments is detecting the position of the levitating object for stable navigation. Possible solutions to this challenge include x-ray and ultrasound images. However, these technologies are costly to implement and have potential harm to the human body. In [74], Moein and Khamesee proposed the art-of-concept of using Hall-effect sensors to assist navigation of a permanent magnet microrobot in a nontransparent environment. In this study, Hall-effect sensors were installed at the bottom of a pole-piece to measure the magnetic flux passing through the working volume. The position of the levitated microrobot was determined based on the measured magnetic flux pattern using Hall-effect sensors. Hall-effect sensors are inexpensive, and their performance satisfies the stable levitation requirement. Therefore, it is a good substitute.

1.3 Contribution of This Thesis

As mentioned in the previous section, the conventional manipulators, such as arm type manipulators, flying robots, and mobile manipulators, generally need a large space for manipulation. The requirement of large manipulation space limits the application and performance of conventional cooperative manipulators. This is even worse for micro manipulation tasks. In addition, the complexity of joint trajectory calculation makes the implementation of control system very challenging. Therefore, there is a need to develop a novel system that can complete cooperative manipulation tasks in a confined space and only require simple motion control schemes.

A magnetically navigated microrobot (MNM) usually consists of a magnetized body part and a microgripper. For example, the body part of the MNM shown in figure 1.5a has two pieces of permanent magnet and a photothermal microgripper. The microgripper is integrated to the permanent magnet to perform micromanipulation operations.

The MNM with an operating finger (microgripper) has been previously developed at the Maglev lab [27]. This thesis simply uses the body of such microrobots, which is a permanent magnet for navigation. Figure 1.5b shows the MNM used in this thesis. It is a cylindrical permanent magnet with 1.29T remnant magnetic flux density, 10mm diameter, and 10mm height. A black plastic cloth outside the MNM is for protect the permanent magnet when there is a sudden collision.

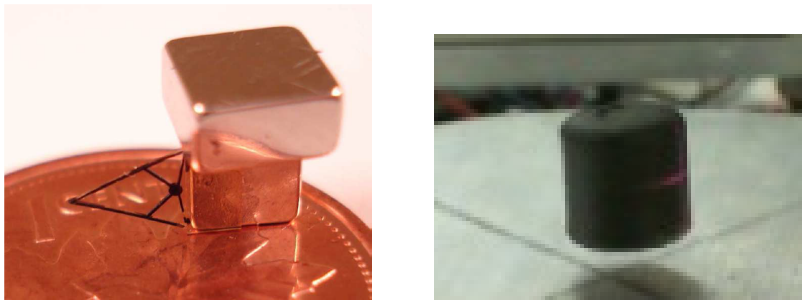

(a) (b)

Figure 1.5: Magnetically navigated microrobot a) The MNM has a permanent magnet body part and a microgripper [27], b) The MNM used in this thesis has only the permanent magnet body part

As the first contribution of this thesis, a novel cooperative manipulation system using a magnetically navigated microrobot (MNM) and a motorized micromanipulator (MM) is developed. There are two reasons for using the MNM. First, it is remotely manipulated without any mechanical connection between its end-effector and its energy source. Therefore, it is good for manipulation in a confined space. Second, the motion control of the MNM is very simple. To the best of our knowledge, this is the first work that uses an MNM to conduct the cooperative manipulation with another arm type manipulator.

The second contribution of this thesis is the dual-axial motion control and dual-axial off-board force determination using magnetic flux density measurement. This is the continuous work of Dr. Mehrtash, who proposed the method for navigating a small permanent magnet and measuring its pushing force on environment. Dr. Mehrtash validated both in one degree of freedom. To have more generous application for the proposed method, the two-degree-of-freedom model and validation is necessary. In this thesis, the 2D navigation model and 2D off-board force model are developed. Both navigation and force model are validated experimentally.

Previous research on magnetic levitation focused on the accurate positioning of a levitation microrobot. However, the disadvantage of only position control is not stable when there is a contact between the microrobot and its environment. In order to improve the stability and to explore the potential application of magnetic navigation, the force control using a position-based impedance controller is developed in this thesis. By applying force control on the MNM, we are able to regulate the pushing force on environment, which in turn improves the navigation stability and protects its environment from being damaged.

For the fourth contribution of this thesis, an adaptive algorithm is developed to es-

timate the parameters of environment when the MNM is pushing its environment. The position-based impedance controller requires a precise reference trajectory if one needs an accurate force tracking performance during the manipulation. The precise reference trajectory calculation is based on the knowledge of the environment that the MNM interacts with. However, the parameters of the environment, such as stiffness and deflection, are not always known. Therefore, an adaptive controller is designed to estimate the environment parameters. By implementing the adaptive algorithm, the impedance controller is capable of tracking the desired force smoothly and precisely.

1.4 Objective and Thesis Outline

In this thesis, the cooperative transportation of a small object in a 2D vertical plane using a motorized micromanipulator (MM) and a magnetic navigated microrobot (MNM) is studied. The cooperative manipulation mechanism is shown in Figure 1.6. The MM is a commercialized motion stage. The MNM system was previously developed at the University of Waterloo in the Maglev lab. To achieve this goal, we needed to solve the following issues: 1) studying the magnetic levitation system for accurate motion control of the MNM with three degrees of freedom, 2) measuring the contact force when the MNM is holding the object without installing a force sensor, and 3) controlling the holding force on the object during the manipulation.

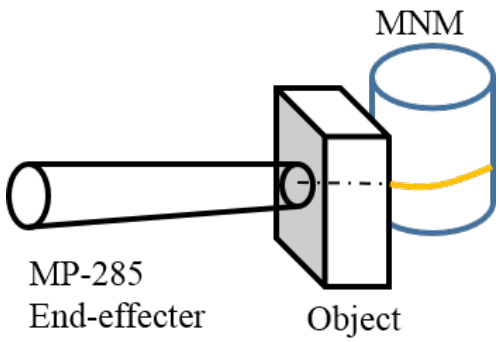

Figure 1.6: Two-micromanipulators cooperative manipulation system. The first micromanipulator is the motorized MP285, the second is the MNM

Since the new cooperative manipulation system consists of two manipulators, the development of the system starts with the research on two manipulators. The research on the magnetic levitation system is presented firstly. This includes the magnetic field modeling, MNM motion control, and dual-axial off-board force determination. The MM system is a

commercialized product. Its motion control is included in the cooperative manipulation system development. The overall flow chart of the thesis is shown in figure 1.7

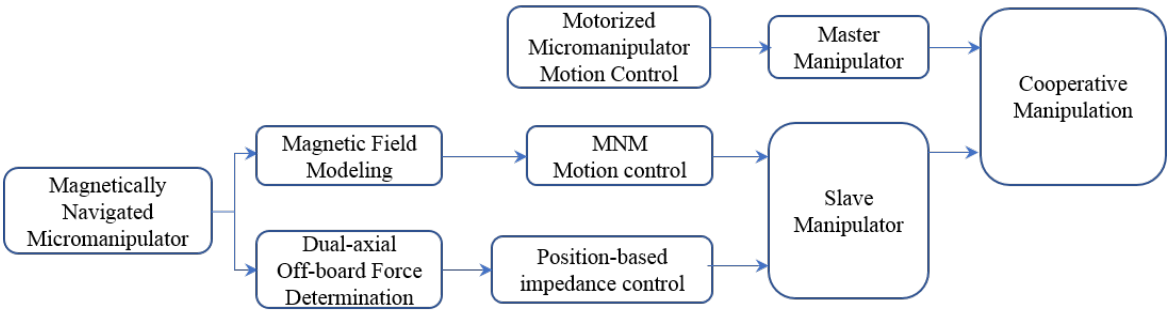

Figure 1.7: Flow chart of the thesis

According to the work flow chart of the research, the outline of this thesis is shown as follows:

Chapter 1 presents various mechanisms for cooperative manipulation and provides a brief introduction to the fundamentals of magnetic levitation. In addition, different types of magnetic levitation techniques and their applications are also introduced.

Chapter 2 introduces the magnetic levitation system used for levitating a magnetized object. The analytical model of the force on a magnetized object and the torque for changing the orientation of the object are presented later. In addition, the process of defining the magnetic field model in the working space is also introduced. The model is finally applied to obtain the dynamic model of a magnetized object.

Chapter 3 introduces a new mechanism for controlling the dual axial motion of an MNM using magnetic flux measurement. This technique is extended to the development of a dual-axial off-board force determination mechanism.

Chapter 4 describes the cooperative manipulation using a MM and an MNM. The system configuration, the image processing, and controller design are presented firstly. Then the system performance is experimentally validated by manipulation of small objects in two directions.

Chapter 5 presents the adaptive force control of the MNM in uncertain environments. A position-based impedance controller plus a robust adaptive algorithm is implemented to achieve the goal of the MNM's compliant motion.

Chapter 6 provides the conclusion and recommendations of the investigation through this thesis.

Chapter 2

Magnetic Levitation System

This chapter presents the analytical study on the magnetic levitation system, which is used to levitate the MNM in the cooperative manipulation. This includes the force and torque model on a magnetized object in an external magnetic field, the principle of magnetic levitation, and the modeling and control of the magnetic levitation system for accurate navigation.

2.1 Magnetic Force and Torque on a Magnetized Object

In this section, the principle of magnetic levitation is presented. The studied robot in the levitation system is a small permanent magnet (PM). The analysis in this chapter is based on assumption that the PM is uniformly magnetized.

2.1.1 Magnetic Field

The Maxwell equations are fundamental for electromagnetic field analysis. Specifically, in magnetic field analysis, Ampere's law and Gauss's law are mostly investigated. The magnetic field intensity $\mathbf{H}$ $(amperes/meter)$ of the magnetostatic field produced by source current with density $\mathbf{J}$ $(amperes/meter^2)$ can be expressed in Ampere's law:

$$\nabla \times \mathbf{H} = \mathbf{J} \tag{2.1}$$

where ∇ is the gradient operator. Since the magnetic field is conservative field, Gauss law for magnetostatic fields has the following format:

$$\nabla \cdot \mathbf{B} = 0 \tag{2.2}$$

where $\mathbf{B}$ is the magnetic flux density in units of $tesla$ or $Wb/meter^2$. In a medium that has a magnetic permeability μ, $\mathbf{B} = \mu\mathbf{H}$, the magnetostatic equations can be solved directly for the fields. However, it is often more convenient to obtain the field using the vector potential $\mathbf{A}$. Applying the differential identity$\nabla \cdot (\nabla \times \mathbf{A}) = 0$, leads to the following expression:

$$\mathbf{B} = \nabla \times \mathbf{A} \tag{2.3}$$

Applying the vector identity

$$\nabla \times \nabla \times \mathbf{D} = \nabla(\nabla \cdot \mathbf{D}) - \nabla^2\mathbf{D} \tag{2.4}$$

to equations (2.1) and(2.3) and imposing the Coulomb gauge $\nabla \cdot \mathbf{A} = 0$ result in Poisson's equation for magnetostatic fields:

$$\nabla^2\mathbf{A} = \mu\mathbf{J} \tag{2.5}$$

In the working space that is no current, the Laplace equation is often applied to calculate the magnetic field. This refers to the scalar potential method.

2.1.2 Magnetic Torque and Force on a PM

A small magnetic dipole in a steady state magnetic field can be represented by an infinitesimal current loop with a surface area of $\mathbf{S}$ and current i that can produce the same magnetic moment

$$m = i\mathbf{S} \tag{2.6}$$

A uniformly magnetized cylinder permanent magnet with magnetic moment $\mathbf{M}$ and volume V is composed of many infinitesimal magnetic dipoles that have the same magnetic moment m. Therefore, the calculation of the force and torque on the permanent magnet will start with the calculation of force and torque on a single infinitesimal current loop. Using the Lorentz force law, the force on an element $d\mathbf{l}$ of a conductor in an external steady magnetic field is given by:

$$d\mathbf{F} = id\mathbf{l} \times \mathbf{B} \tag{2.7}$$

where $d\mathbf{F}$ is a vector indicating the magnitude and direction of magnetic force on the conductor element, i is the scalar magnitude of the current in the conductor element, $d\mathbf{l}$ is a vector shows the length of the conductor element and the direction of the current, and $\mathbf{B}$ is the vector that indicates the flux density of the external magnetic field. The torque on the infinitesimal current loop is expressed as:

$$\mathbf{T} = i \oint_C [\mathbf{r} \times (d\mathbf{l} \times \mathbf{B})] \tag{2.8}$$

where $\mathbf{r}$ is the position vector of $d\mathbf{l}$ and the integration is around the loop. By using the identity:

$$\mathbf{r} \times (d\mathbf{l} \times \mathbf{B}) = d\mathbf{l}(\mathbf{r} \cdot \mathbf{B}) - \mathbf{B}(\mathbf{r} \cdot d\mathbf{l}) \tag{2.9}$$

Eq (2.8) can be written as

$$\mathbf{T} = i[\oint_C (\mathbf{r} \cdot \mathbf{B}) d\mathbf{l} - \mathbf{B} \oint_C \mathbf{r} \cdot d\mathbf{l}] \tag{2.10}$$

Applying the Stokes's theorem and the identity

$$\oint_C P d\mathbf{r} = \iint_S (\mathbf{n} \times \nabla P) dS \tag{2.11}$$

Eq (2.10) becomes

$$\mathbf{T} = i\Big(\iint_S [d\mathbf{S} \times \nabla(\mathbf{r} \cdot \mathbf{B})] - \mathbf{B} \iint_S (\nabla \times \mathbf{r}) \cdot d\mathbf{S} \Big) \tag{2.12}$$

where $d\mathbf{S}$ is a vector indicates the magnitude and normal direction of the current loop. Since $\nabla \times \mathbf{r} = 0$, $\nabla(\mathbf{r} \cdot \mathbf{B}) = \mathbf{B}$ for constant $\mathbf{B}$, and the magnetic moment m of an infinitesimal current loop exists, Eq (2.12) becomes

$$\mathbf{T} = i \iint_S d\mathbf{S} \times \mathbf{B} = i\mathbf{S} \times \mathbf{B} = m \times \mathbf{B} \tag{2.13}$$

The magnetic force on an infinitesimal current loop in the external magnetic field can be deduced using the virtual displacement method. Suppose the external magnetic force/-torque tries to rotate the current loop by $d\theta$, the work $d\mathbf{W}$ required to finish the process is the same as the increase in the current loop's potential energy dU

$$dU = d\mathbf{W} = \mathbf{T} d\theta = m\mathbf{B} sin\theta d\theta \tag{2.14}$$

Then integrating the incremental potential energy leads to the total potential energy of the current loop

$$U = \int_0^\theta m\mathbf{B} sin\theta d\theta = -m\mathbf{B} cos\theta = -m \cdot \mathbf{B} \tag{2.15}$$

If there is a translation motion caused by magnetic force $\mathbf{F}$, the work $d\mathbf{W}$ done by the force is equal to the decrease in potential energy dU, which means

$$d\mathbf{W} = \mathbf{F} \cdot d\mathbf{r} = -dU \tag{2.16}$$

where the complete differential $dU = \nabla U \cdot \mathbf{r}$. Then the general magnetic force on an infinitesimal current loop in the external magneto-static field is

$$\mathbf{F} = -\nabla U = \nabla(m \cdot \mathbf{B}) \tag{2.17}$$

The magnetization direction of the cylindrical permanent magnet used in this thesis is in the z-direction. In the Cartesian coordinate system, the following expressions are obtained

$$F_x = \mathbf{M}V\frac{d\mathbf{B}_z}{dx} \tag{2.18}$$

$$F_y = \mathbf{M}V\frac{d\mathbf{B}_z}{dy} \tag{2.19}$$

$$F_z = \mathbf{M}V\frac{d\mathbf{B}_z}{dz} \tag{2.20}$$

Therefore, the magnetic torque and force on a permanent magnet in an external magnetostatic field can be deduced using the virtual displacement method and potential energy method. The magnetic force on a permanent magnet with magnetization $\mathbf{M}$ in an external magnetostatic field is proportional to the magnetization of the permanent magnet and the gradient of the external magnetostatic field. Particularly, in this thesis, the magnetic force on the studied permanent magnet is related to the 3D gradient of the z-component magnetic field. In addition, the magnetic torque tries to align the permanent magnet parallel with the external magnetic field. However, in this research, the magnetic field in the workspace is uniform in the z direction. Therefore, it is assumed that the orientation of the levitated robot remains constant during the manipulation.

2.2 Principle of Magnetic Levitation

Active navigation of a magnetized object requires a controlled magnetic field source. Generally, the magnetic field can be generated by current-controlled electromagnets, permanent magnets held by a position-controlled manipulator, and Helmholtz coils. The use of a permanent magnet provides limited motion control accuracy, since it is challenging to adjust the position of a manipulator actively at the relatively high frequency necessary for stable levitation of a magnetized object. The magnetic field and its gradient are independent in a Helmholtz coils system. A system that uses Helmholtz coils is limited to 3D translation of an object.

Electromagnets are commonly used for multi-dimensional manipulation of a magnetized object. The magnetic field generated by electromagnets is controlled by current in the

electromagnets. The multi-degree freedom of motion of an object is achieved by setting up special configurations of multi-electromagnets. Since the strength of the magnetic field decays rapidly as the distance from the electromagnet increases, an iron-core is commonly used to significantly enhance the magnetic field strength outside the electromagnet. This enhanced magnetic field can then expand the workspace of the magnetized object.

A magnetic levitation system mainly consists of an energy source, a levitation robot, sensors, and a controller unit. Figure 2.1 shows the basic schematic of a magnetic levitation system for 1-D and 2-D levitation. The magnetic drive unit, consisting of one or more electromagnets, produces energy for levitation and manipulation. The levitation robot is a magnetized object. To save energy, the magnetized object is commonly made from ferromagnetic materials that have high magnetic permeability and from a permanent magnet that has strong remnant magnetic flux density. A gripper is installed on the magnetized object to perform special tasks. Earnshaw's theorem indicates that pure interaction between a magnetic energy source and a magnetized object cannot maintain a stable levitation. The feedback dynamics of the levitation robot are required. Therefore, a position sensor and controller unit are necessary. A single electromagnet can be used for the levitation of an object and motion in the vertical direction (Figure 2.1(a)). If multiple electromagnets are used, the vertical and the horizontal motions can be achieved simultaneously (Figure 2.1(b)). The horizontal motion is achieved by changing the current ratio in each electromagnet.

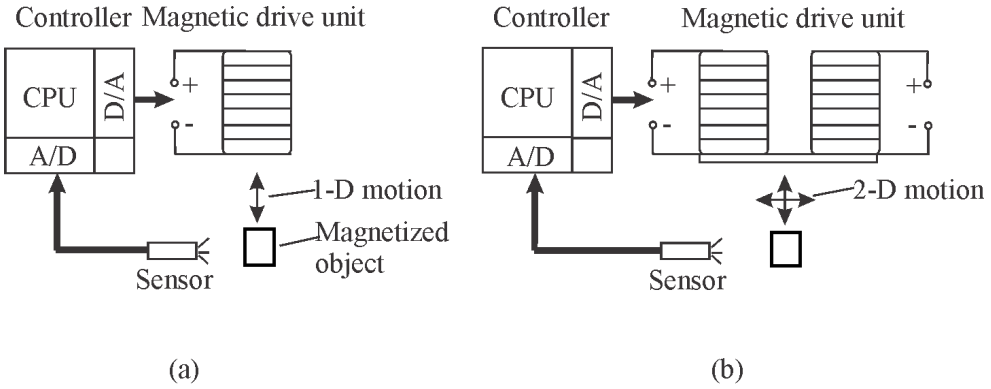

Figure 2.1: Schematic of magnetic levitation systems for 1-D and 2-D levitation [113]

In this thesis, the controlled external field, is produced by six identical electromagnets which were evenly distributed on a disc. According to the Biot-Savart Law, the magnetic field produced by a multi-layer finite length solenoid with iron core(Figure 2.2) at a random point in free space is [91]:

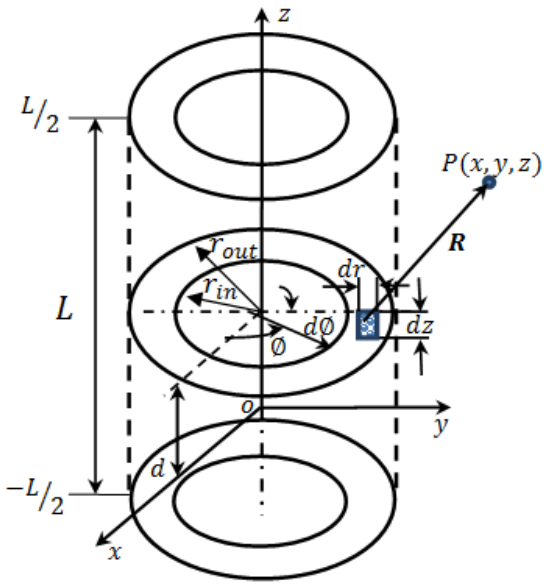

Figure 2.2: Multi-layer finite length solenoid

$$B_S(x,y,z) = \beta\frac{\mu_0\sigma I}{4\pi}\int_{r_{in}}^{r_{out}}\int_{\frac{-L}{2}}^{\frac{L}{2}}\int_0^{2\pi}\frac{r(-\sin\phi i+\cos\phi j)\times R}{|R|^3}d\phi dz dr \tag{2.21}$$

where $B_S(x,y,z)$ is the magnetic flux density of a single solenoid at point $P(x,y,z)$ in free space. β is the magnetic flux density factor of the soft-iron core effect in the enhancement of the magnetic field and σ is the winding density of the electromagnet. Its unit is turns per unit are. I is the current supplied to the electromagnet, r_{in} and r_{out} are the inner and outer radii of the electromagnet respectively. L is the height of the electromagnet. $R = (x - r\cos\phi)\mathbf{i} + (y - r\sin\phi)\mathbf{j} + (z - d)\mathbf{k}$ is the vector from the area of interest to point $P(x,y,z)$, and d is the vertical distance between the calculating surface and the origin of the coordinate system.

If there were six electromagnets, and they were evenly distributed on a disc as shown in figure 2.3, theoretically, the resultant magnetic flux density at any point in the free space would be the vector summation of the magnetic flux density generated by each electromagnet. The analytical expression is:

$$B_m(x,y,z) = \sum_{i=1}^{6} B_i(x,y,z) \tag{2.22}$$

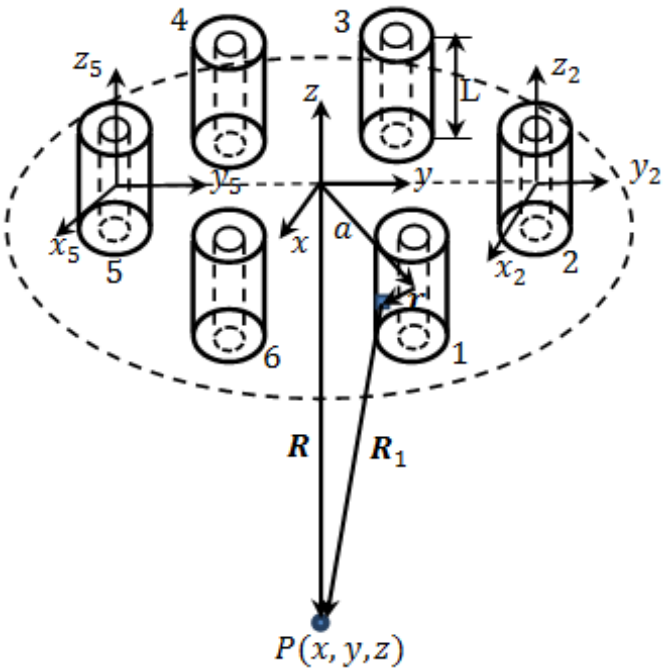

Figure 2.3: Multi-layer finite length solenoid [112]

where $B_m(x, y, z)$ is the magnetic flux density of multi electromagnets at point $P(x, y, z)$, i indicates the i^{th} electromagnet, $i = 1, 2, ..., 6$, $B_i(x, y, z)$ is the magnetic flux density of the i^{th} electromagnet at point $P(x, y, z)$.

In an actual situation the resultant magnetic flux density is slightly less than the analytical results because of the interaction between electromagnets. In this thesis, the system worked in the steady state, and the mutual inductance among electromagnets was negligible.

From equation 2.22, the z-component of the magnetic flux density is:

$$B_z(x, y, z) = \sum_{i=1}^{6} B_{zi}(x, y, z) \tag{2.23}$$

where

$$B_{zi}(x, y, z) = \beta \frac{\mu_0 \sigma I}{4\pi} \int_{r_{in}}^{r_{out}} \int_{\frac{-L}{2}}^{\frac{L}{2}} \int_{0}^{2\pi} \frac{r((y - y_i - r\sin\phi)\sin\phi + (x - x_i - r\cos\phi)\cos\phi j)}{|R|^3} d\phi dz dr \tag{2.24}$$

where $B_{zi}(x, y, z)$ is the z-component magnetic flux density of the i^{th} electromagnet at the point $P(x, y, z)$, and β is 3.15 here.

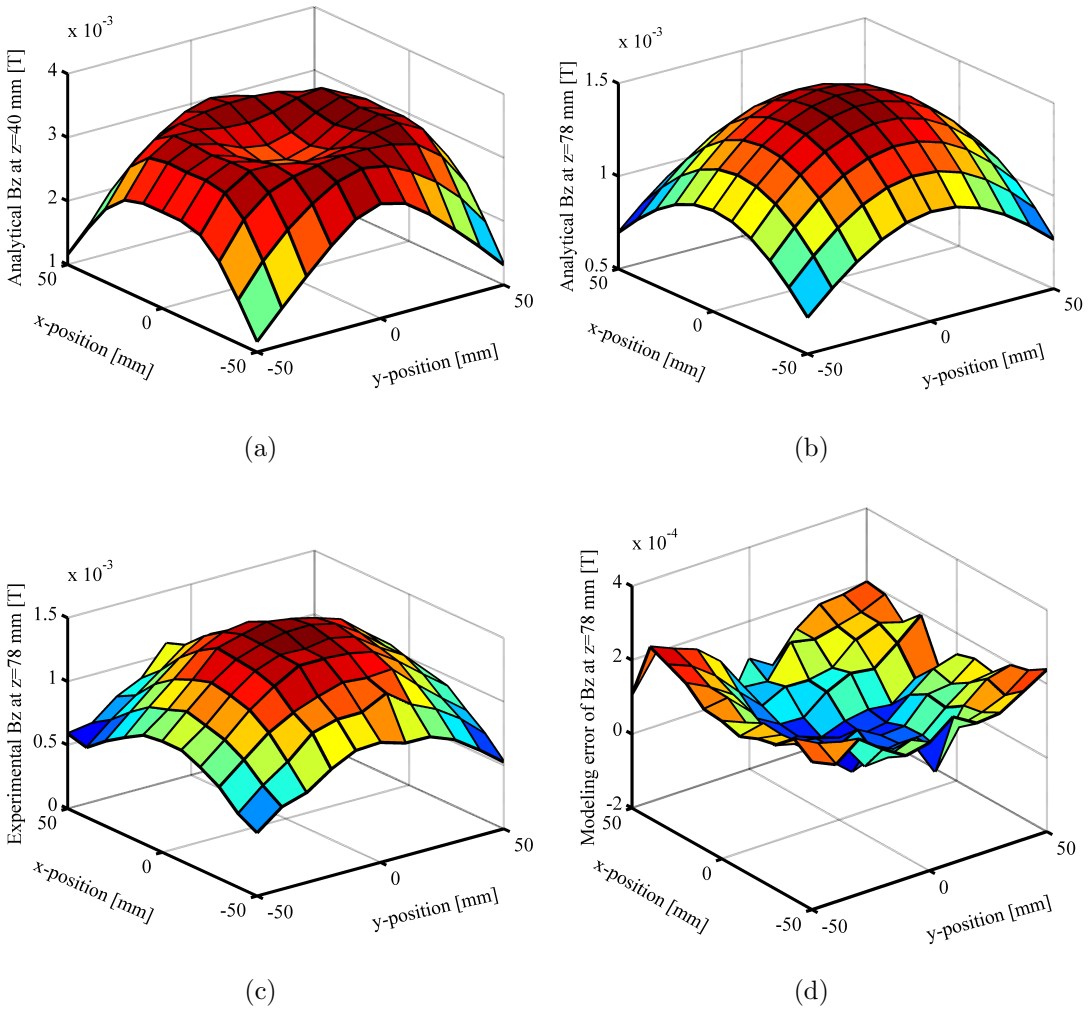

Figure 2.4: z-component analytical magnetic flux density in horizontal planes: (a) the plane was located at 40 mm below electromagnets; (b) the plane was located at 78 mm below electromagnets; (c) measured field at z=78 mm below electromagnets; (d) modeling error at z=78 mm.

Using equation 2.24, the z-component of the magnetic flux density was calculated in an

area of $100 \times 100mm^2$ in horizontal planes at different distances below the electromagnets (figure 2.3) powered by 1A dc. The result is shown in figure 2.4. Figure 2.4a is the magnetic flux density B_z at $z = 40mm$ below the bottom of the electromagnets. Figure 2.4b is the magnetic flux density B_z at $z = 78mm$ below the bottom of the electromagnets. The electromagnets used in the calculation model had the following geometric parameters: $N = 840turns$, $r_{in} = 10mm$, $r_{out} = 20mm$, and $L = 40mm$. The analytical field model is examined experimentally at $z = 78mm$ below a set of 6 electromagnets evenly distributed on a 13.5cm diameter disc. The experimental result is shown in figure 2.4c. Figure 2.4d shows the error between analytical and experimental results. The field analytical model is very accurate at locations close to the center of the working area, even though more error exists at locations far from the center. The minimum modeling error of $6\mu T$ is 0.4% of the maximum flux density 1.4mT. This indicates that the analytical model can be used for modeling the magnetic field of an area of $10 \times 10mm^2$. However, this model is valid only for iron-core electromagnets without connecting with the iron-yoke and the iron pole-piece.

2.3 Magnetic Drive Unit

To produce a sufficient magnetic levitation force, equations 2.18-2.20 indicate that a non-uniform external magnetic field is required to impose magnetic forces on a magnetized object. In the non-uniform magnetic field, there is a point that has the minimum magnetic potential energy. Khamesee [54] explained that the magnetized object tends to move toward the minimum magnetic potential energy point in the external magnetic field. This point, also known as the point that has the maximum magnetic flux density, is defined as the B_{max} point. A single electromagnet can generate a single B_{max} point on a horizontal plane below the electromagnet and can produce a magnetic gradient force to compensate for the gravity. However, the horizontal location of the B_{max} point cannot be changed. Therefore, only one-directional levitation is achievable using a single electromagnet.

To obtain the multi-dimensional levitation of a magnetized object, a combination of electromagnets is required. However, multiple electromagnets produce multiple B_{max} points, which make the levitation of a single magnetized object uncontrollable. Khamesee [55] proposed using an iron pole-piece to connect multiple electromagnets. The induced magnetization of the pole-piece produces a single B_{max} point below the electromagnets.

For the magnetic levitation system shown in figure 2.5, the magnetic field source consists of six identical electromagnets powered with DC. A disk shape soft-iron pole-piece connects the electromagnets and configures the magnetic field in the workspace. A soft-iron yoke is installed to generate a closed-loop magnetic circuit and to increase the magnetic field strength in the workspace. The relative permeability μ_r of both yoke and pole-piece is 4000.

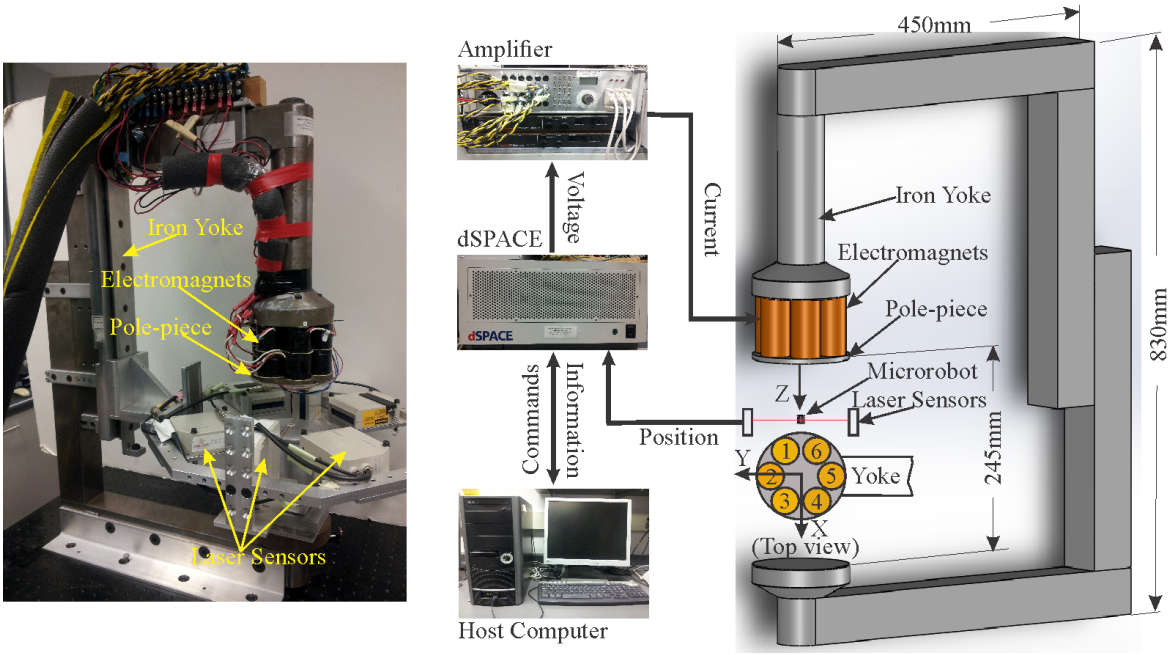

Figure 2.5: The schematic of the magnetic levitation system [113]

All electromagnets have a configuration of 840 turns of ♯22AWG wire, 20mm outer radius, 10mm inner radius, and 40mm length. Simulation results in Figure 2.6 are presented to show the concept of changing the B_{max} point location and the effect of the iron yoke on increasing the intensity of the magnetic field at z=55mm below the pole-piece.

As shown in figure 2.6(a) and (b), the location of the maximum magnetic flux density point in the workspace is located in the center of a horizontal plane if the electromagnets are equally loaded. Otherwise, the maximum magnetic flux density point moves toward the electromagnet that is loaded with more current. Figure 2.6(c) and (d) show that when an iron yoke is installed, the magnetic field intensity and the horizontal gradient of the magnetic field are increased significantly. The soft iron yoke also increases the vertical gradient of the magnetic field in the workspace, which in turn increases the levitation force on the levitated object. Figure 2.7 shows the vertical gradient of the magnetic field below the center of the pole-piece. It shows that the gradient of the magnetic field with the iron yoke is twice as high as the gradient of the magnetic field without an iron yoke.

The magnetic flux density in the air-gap of the levitation stage while electromagnets are equally loaded with one Ampere current is shown in figure 2.8. On planes that are close to the pole-piece, the B_{max} point is not unique. The stable levitation of a single

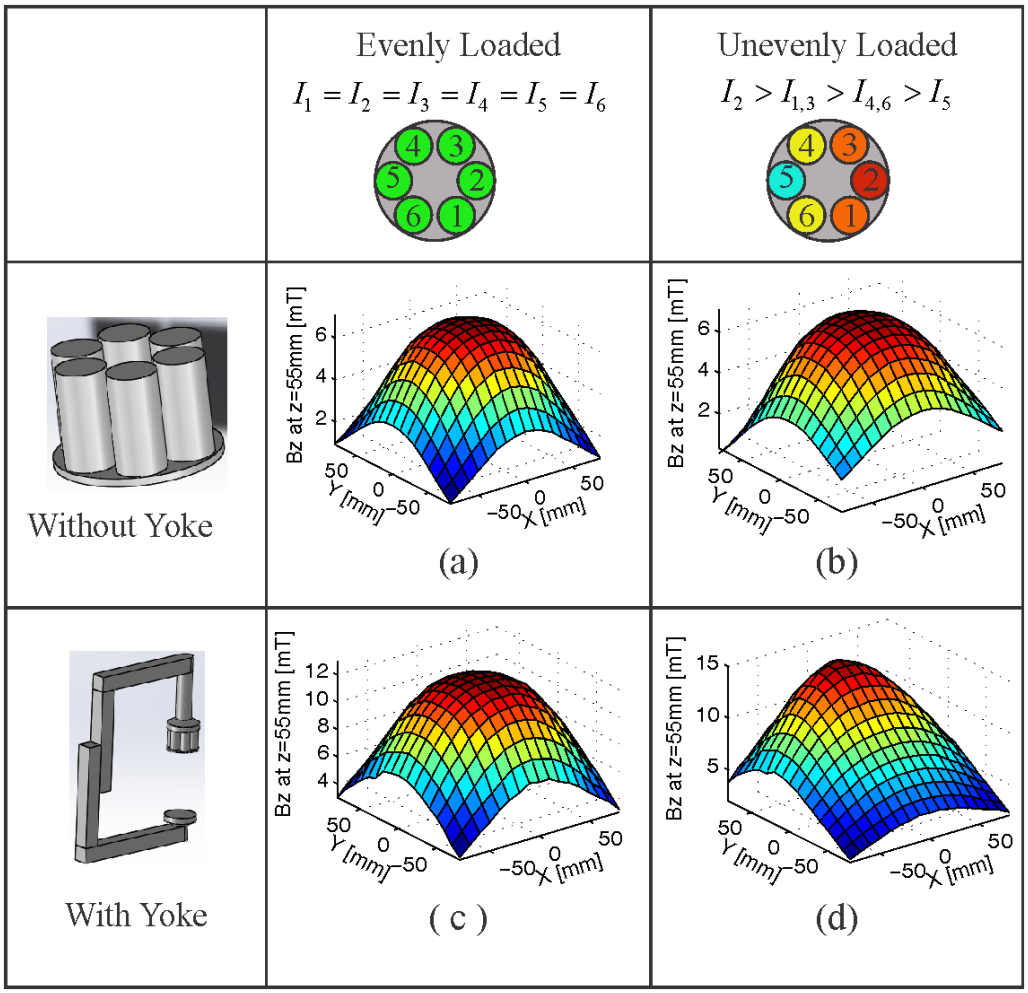

Figure 2.6: Demonstration of the qualitative performance of pole-piece and iron yoke [113]

magnetized object on these planes is not achievable. On planes that are relatively far from the pole-piece, only one B_{max} point exists. The stable levitation of a single magnetized object on these planes is achievable. The workspace of the developed magnetic levitation system is 65mm-95mm below the pole-piece. In this section, the gradient of the magnetic field is linear with respect to the distance from the pole-piece.

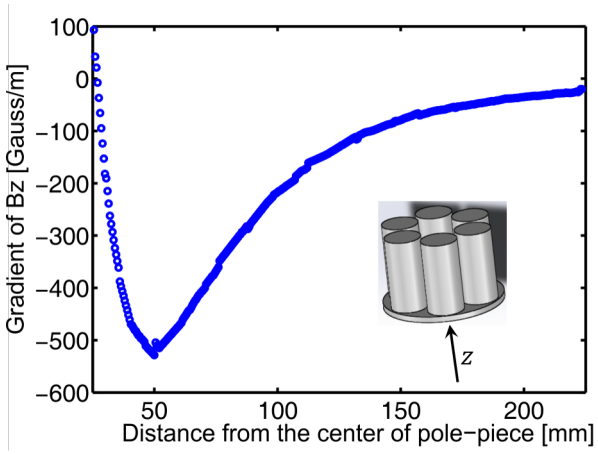

(a)

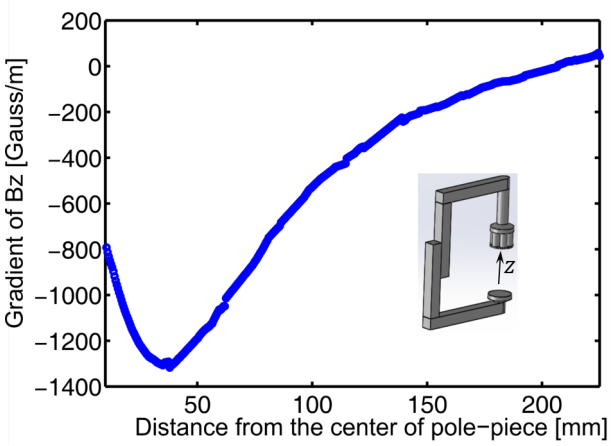

(b)

Figure 2.7: Vertical gradient of the magnetic field with and without iron yoke

2.4 Peripheral Equipment

The levitation can't be fulfilled by using only a MDU and a magnetized robot. Other peripheral equipment is necessary for stable levitation. Figure 2.5 indicates that the magnetic levitation system has a dSPACE controller, Laser-sensor position-detection system, current amplifier, and a communication computer.

The dSPACE real-time controller functions as the central control unit of the whole system. It has ControlDesk as a user interface, and is able to be programmed directly

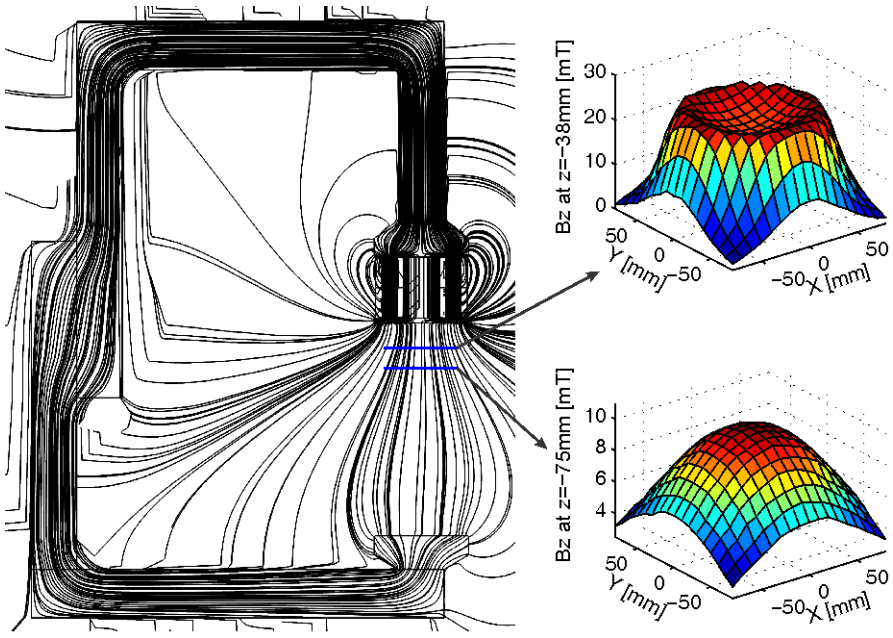

Figure 2.8: Qualitative analysis of the magnetic field in the workspace [113]

in Simulink software environment. The main board of the dSPACE controller is DS-1006 which has a quad-core AMD 2.2GHz Opteron processor. The main board is connected to a DS-2004 A/D board and a DS-2103 D/A board by Bus cable. The DS-2004 A/D board has 16 input channels, 16 bit resolution, and ±5V or ±10V input voltage range. The DS-2103 D/A board has 32 input channels, 14 bit resolution, and ±5V or ±10V output voltage range. The amplifier is combined with two Sorensen DCS40-30E DC power supplies are driven by the D/A board through an interface and output current to power the electromagnetic coils. The computer used for human-machine interface has a Intel Pentium D 3.20GHz CPU and 2.00GB of RAM. Windows XP professional Service Pack 3 operating system is installed on the computer.

The laser sensors used for detecting levitating robot position are LS-5041 purchased from the company KEYENCE. Three sets of laser sensors, installed surrounding the working space, are used to measure the three dimensional position of the levitating robot (see figure 2.9). The laser sensor has 1200 Hz scanning rate, ±10V analogue output range, and 0.2 mm-40 mm measurement range. The maximum resolution of position measurement depends on the size of the object that is measured (see figure 2.10)

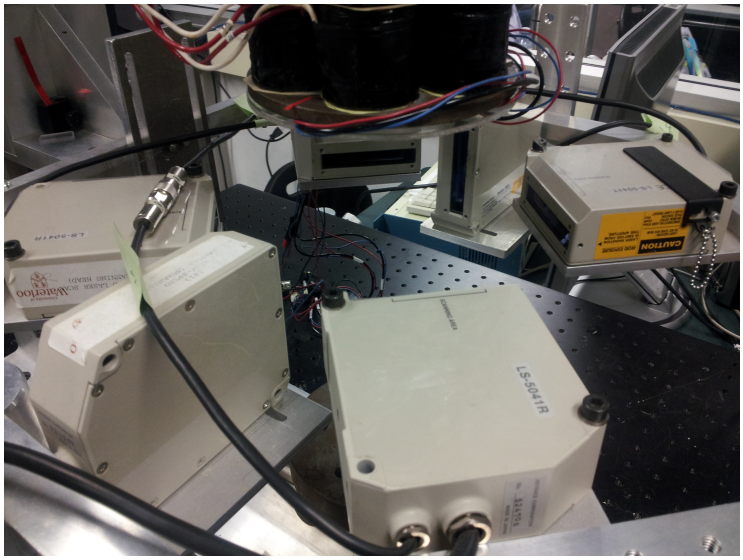

Figure 2.9: Laser sensor setup for measuring the 3D position of levitating robot

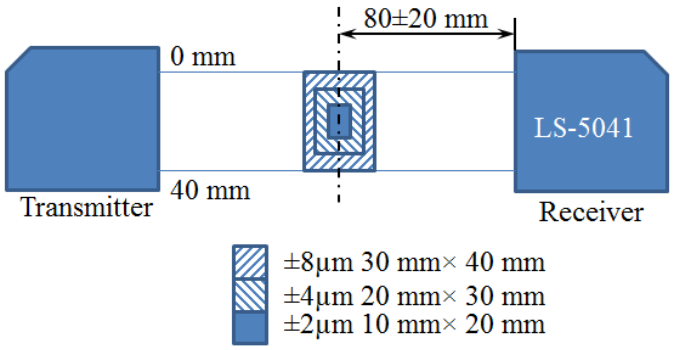

Figure 2.10: Accuracy mapping of the Laser sensor

2.5 Modeling of Magnetic Field in the Working Space

The presence of the iron yoke and the pole-piece make the process of finding the closed form of the magnetic field model in the working space of the levitating robot very challenging. The asymmetry in the geometry of the MDU simply produce an asymmetrical magnetic field. In addition, magnetizing the ferromagnetic materials brings high nonlinearity to the system. Therefore, in this thesis, the experimental method is used to find the magnetic field model in the working space. The experimental data driven method is then used to design the controller for position control. According to equations (2.18), (2.19), and (2.20), the

magnetic force on a magnetized object is determined by the z-component of the magnetic field produced by the MDU, so the z-component B_z of the magnetic flux density in the working space is measured.

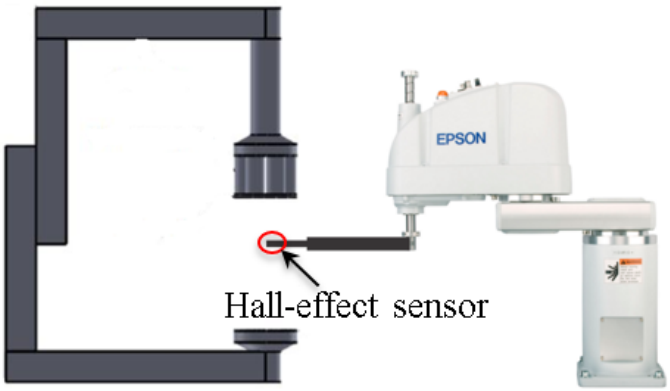

Figure 2.11: Experimental setup for magnetic field measurement in the workspace

The system setup for measuring the magnetic field in the workspace is presented in figure 2.11. During the magnetic field measurement, a LakeShore 421 Gauss meter was used. The Gaussmeter probe (a Hall-effect sensor installed at the head of the probe), held by an EPSON SCARA robot, was moved in the working space to detect the field. The measurement range is 0-200 mm from the center of the pole-piece in the vertical direction with a moving step of 10 mm. The measurement range is 50×50 mm^2 in horizontal planes with a total number of 4 planes which locate at 55mm, 65mm, 75mm, and 85mm below the pole-piece. The probe was moved at 10 mm steps during the measurement, which means that there are 121 measurement points in each horizontal plane.

In figure 2.5, the configuration of electromagnets is shown. Six pairs of iron-core coils are evenly distributed on a disc shape iron pole-piece. In the installation, coil 2 and 5 are installed along the y-axis. Coils 3, 4 and coils 1, 6 are symmetrically installed with respect to the y-z plane. The iron yoke is located in the positive direction of the y-axis, and close to coils 4, 5, and 6. The iron yoke has the effect of moving the minimum magnetic potential energy point towards the iron yoke in a horizontal plane. Figure 2.12 is the z component of magnetic flux density measured by a gauss meter at 75 mm below the pole piece while coil 1 is powered with 1A dc. From the projection plot in figure 2.13, it can be concluded that the z component magnetic field along the x-axis has a parabolic shape, which means that the field can be represented by a second order polynomial. At a specific y-axis position y_0, the z component magnetic field of coil 1 is:

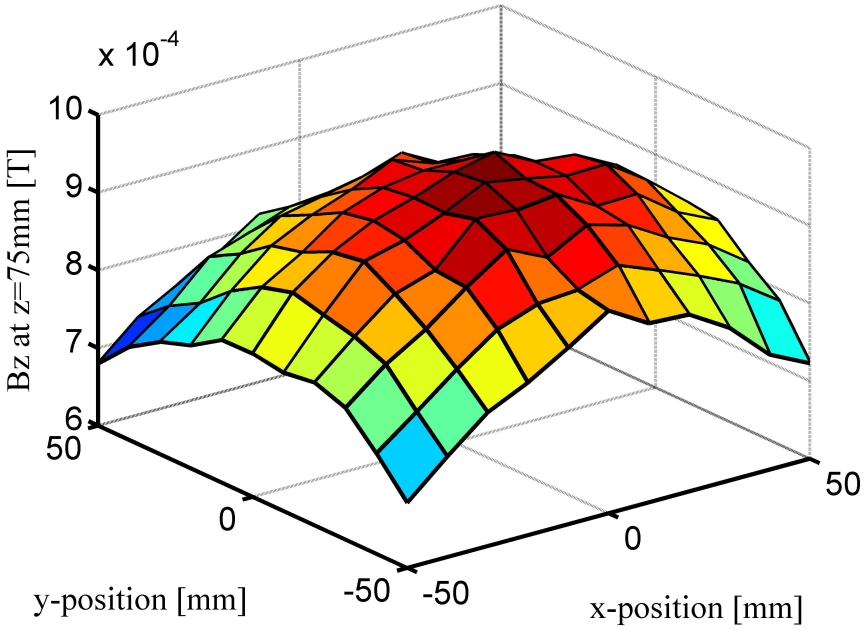

Figure 2.12: The z-component of magnetic flux density at z=75 mm below the pole piece while coil 1 is powered with 1A dc current

$$\mathbf{B}_{z1} = \left(a_{1x}x^2 + b_{1x}x + c_{1x}\right) I_1 \tag{2.25}$$

where $[a_x, b_x, c_x]$ can be determined based on the experimental data. The coefficient a_x can be treated as constant in a horizontal plane, but will change linearly with respect to the location in vertical direction. The coefficients b_x and c_x are second order polynomial in y axis of a horizontal plane. The coefficients of b_x and c_x polynomial also change linearly with respect to the vertical location.

$$a_{1x} = a_{az1}z + b_{az1} \tag{2.26}$$

$$b_{1x} = (a_{baz1}z + b_{baz1})y^2 + (a_{bbz1}z + b_{bbz1})y + (a_{bcz1}z + b_{bcz1}) \tag{2.27}$$

$$c_{1x} = (a_{caz1}z + b_{caz1})y^2 + (a_{cbz1}z + b_{cbz1})y + (a_{ccz1}z^2 + b_{ccz1}z + c_{ccz1}) \tag{2.28}$$

According to figure 2.14 and figure 2.15, the magnetic fields produced by coils 2 and 5 are symmetric about the y-z plane. So, in the second order polynomial model of coil 2 and 5, $b_{2x} = 0, b_{5x} = 0$. Similar to B_{z1}, the field representation of coil 2 is:

$$\mathbf{B}_{z2} = \left(a_{2x}x^2 + c_{2x}\right) I_2 \tag{2.29}$$

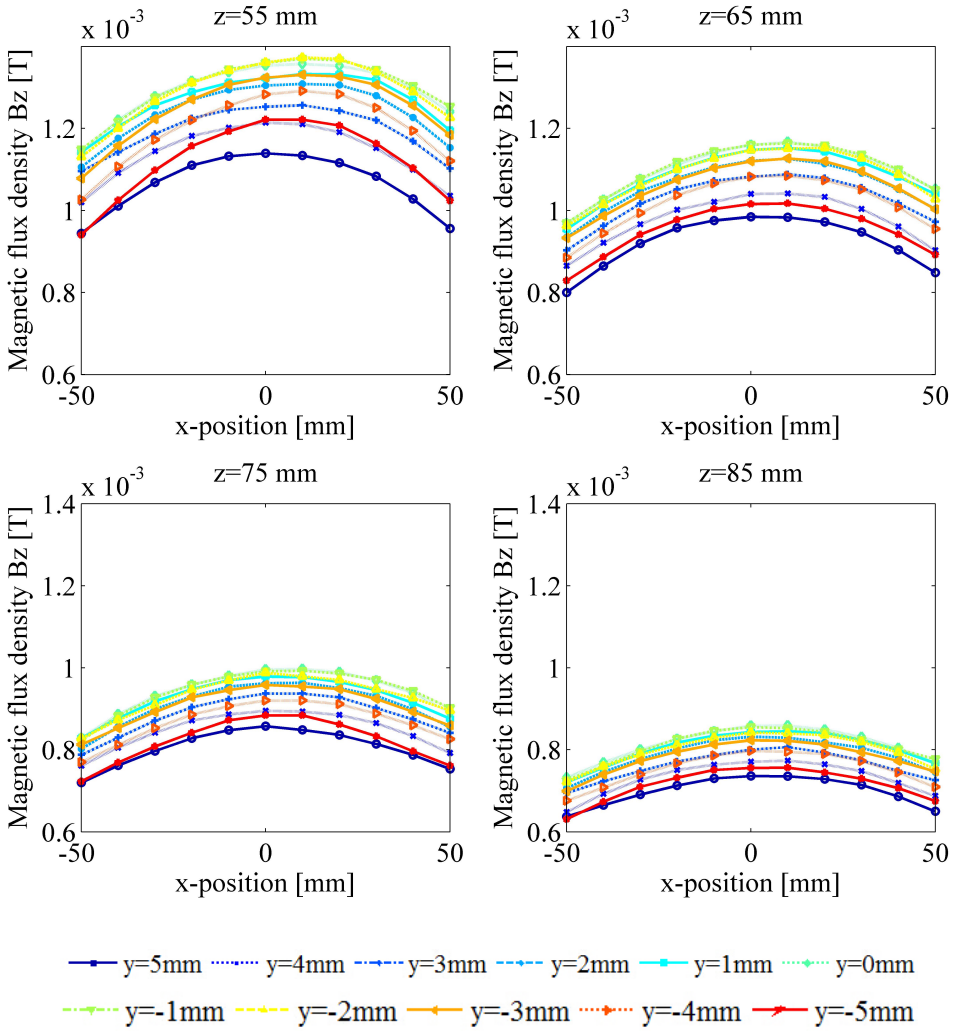

Figure 2.13: Magnetic flux density B_z at $z = 55mm$, $z = 65mm$, $z = 75mm$, and $z = 85mm$ below the pole-piece while coil 1 is powered with 1A current

where

$$a_{2x} = a_{az2}z + b_{az2} \tag{2.30}$$

$$c_{2x} = (a_{caz2}z + b_{caz2})y^2 + (a_{cbz2}z + b_{cbz2})y + (a_{ccz2}z^2 + b_{ccz2}z + c_{ccz2}) \tag{2.31}$$

Since coils 3 and 1 are symmetric about y-z plane, the coefficients of the magnetic field

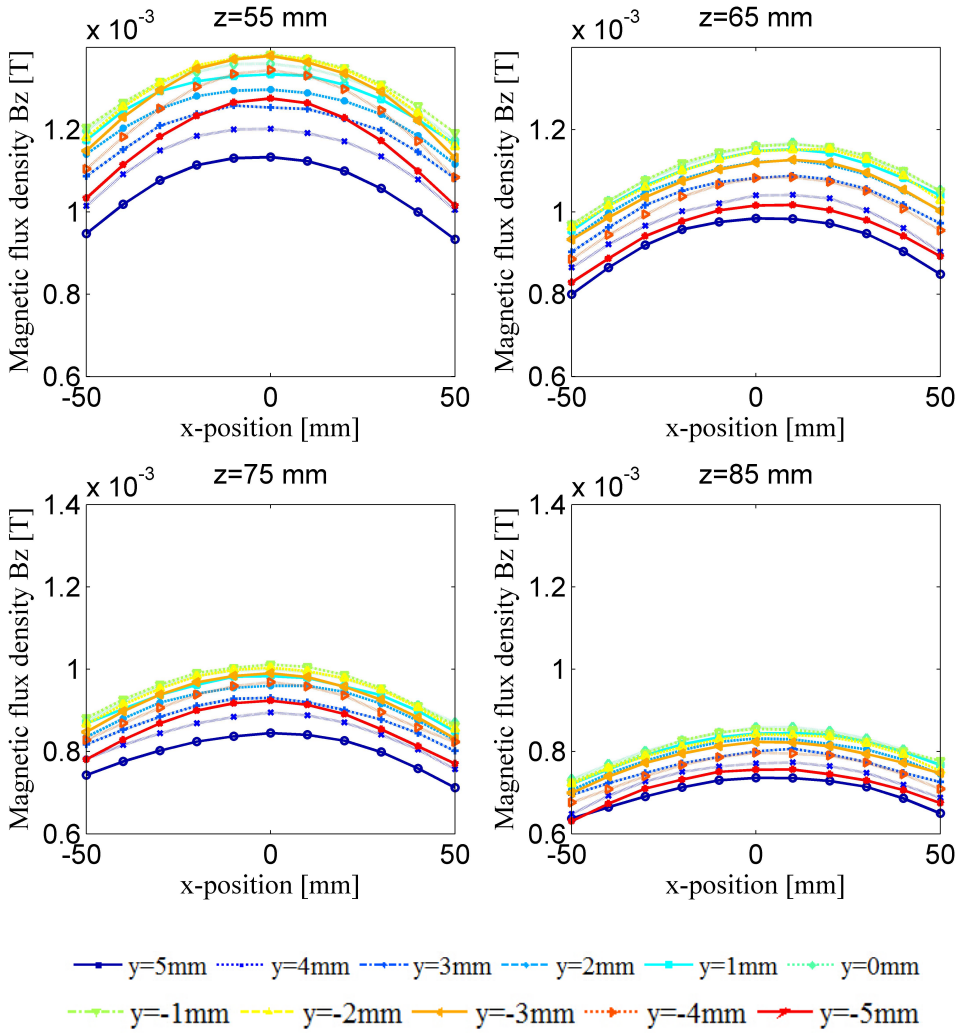

Figure 2.14: Magnetic flux density B_z at $z = 55mm$, $z = 65mm$, $z = 75mm$, and $z = 85mm$ below the pole-piece while coil 2 is powered with 1A current

model for coil 3 are: $a_{3x} = a_{1x}$, $b_{3x} = -b_{1x}$, and $c_{3x} = c_{1x}$.

Although coils 1,3 and coils 4, 6 are geometrically symmetric about the x-z plane, the existence of the iron yoke in the y-axis make the field asymmetric in the y-direction. Therefore, the field produced by coils 4, 5, and 6 needs to be modeled separately. The magnetic field of coil 4 is shown in figure 2.16. Similar to the modeling of coil magnetic

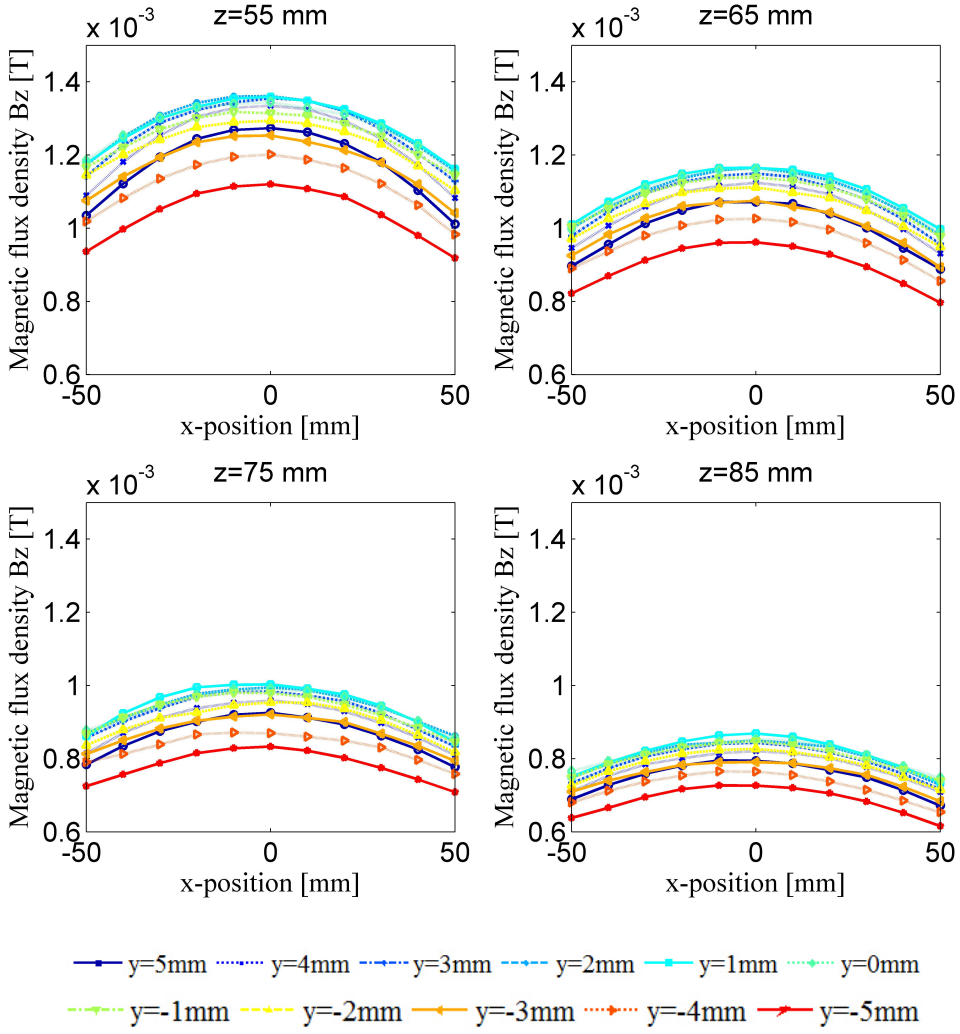

Figure 2.15: Magnetic flux density B_z at $z = 55mm$, $z = 65mm$, $z = 75mm$, and $z = 85mm$ below the pole-piece while coil 5 is powered with 1A current

field, the magnetic field of coil 4 can be modeled as:

$$\mathbf{B}_{z4} = \left(a_{4x}x^2 + b_{4x}x + c_{4x}\right) I_4 \tag{2.32}$$

$$a_{4x} = a_{az4}z + b_{az4} \tag{2.33}$$

$$b_{4x} = (a_{baz4}z + b_{baz4})y^2 + (a_{bbz4}z + b_{bbz4})y + (a_{bcz4}z + b_{bcz4}) \tag{2.34}$$

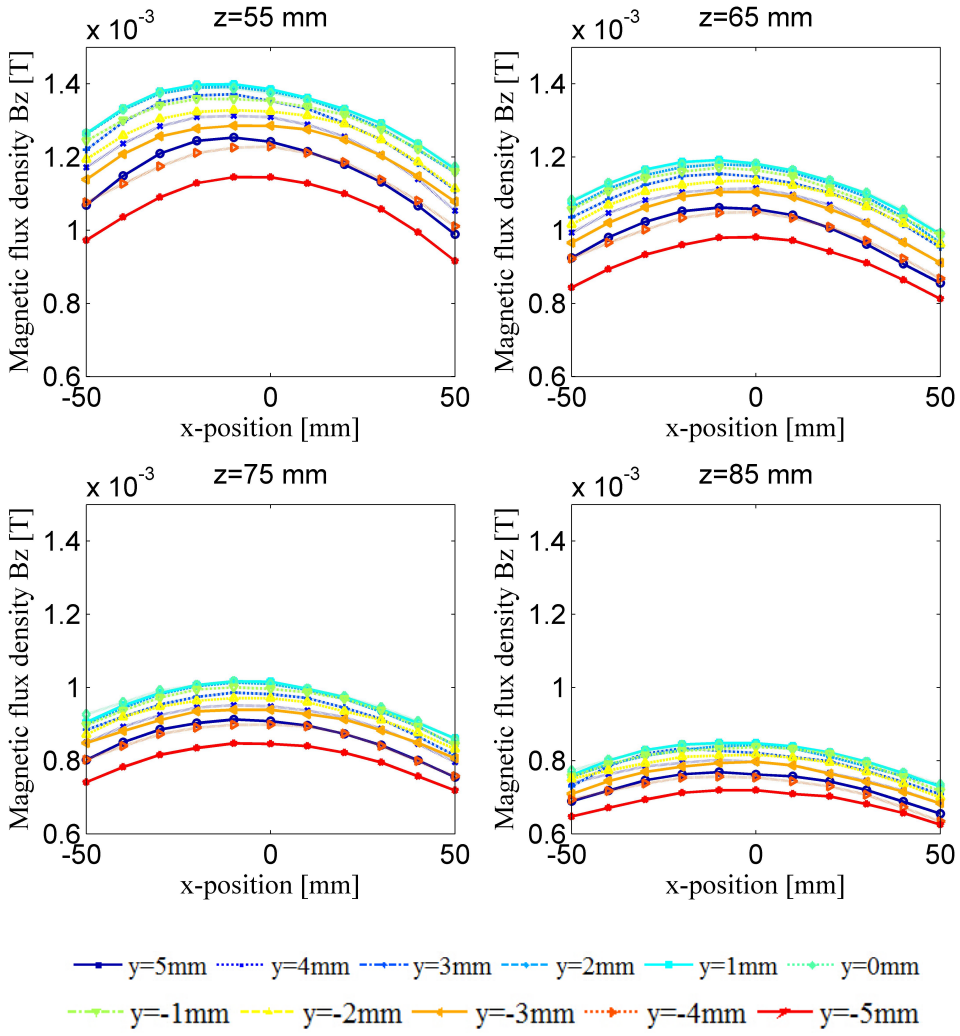

Figure 2.16: Magnetic flux density B_z at $z = 55mm$, $z = 65mm$, $z = 75mm$, and $z = 85mm$ below the pole-piece while coil 4 is powered with 1A current

$$c_{4x} = (a_{caz4}z + b_{caz4})y^2 + (a_{cbz4}z + b_{cbz4})y + (a_{ccz4}z^2 + b_{ccz4}z + c_{ccz4}) \tag{2.35}$$

Coefficients of the magnetic field model of coil 6 can be obtained in the same way as coil 3. We have $a_{6x} = a_{4x}$, $b_{6x} = -b_{4x}$, and $c_{6x} = c_{4x}$. The model format of the coil 5 field is the same as coil 2. However, the iron yoke effect makes it necessary to model separately

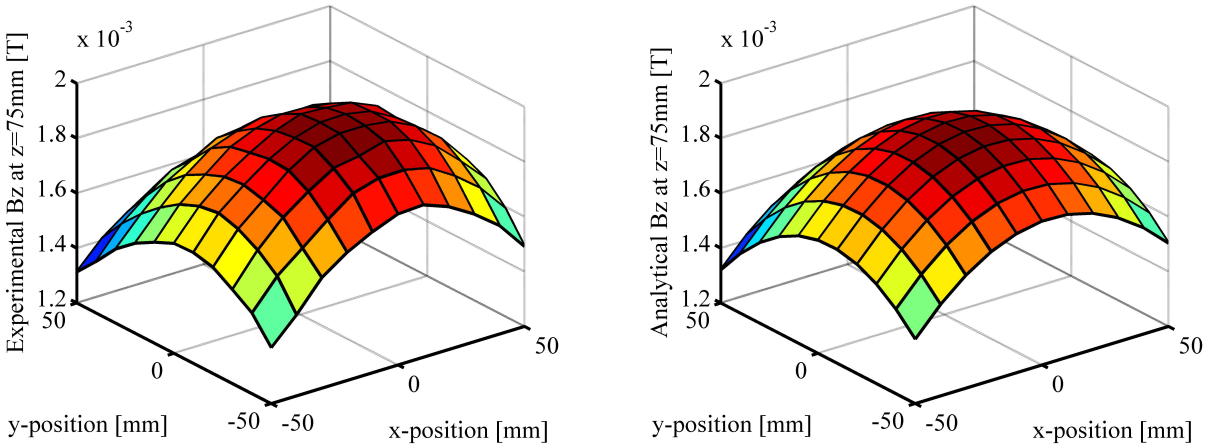

a b

Figure 2.17: Magnetic flux density B_z using fitting model and experimental method when coil 1 and 2 are powered with 1A dc current a) experimental measurement B_z, b) Analytical modeling B_z

the magnetic field of coils 2 and 5.

$$\mathbf{B}_{z5} = \left(a_{5x}x^2 + c_{5x}\right) I_5 \tag{2.36}$$

where

$$a_{5x} = a_{az5}z + b_{az5} \tag{2.37}$$

$$c_{5x} = (a_{caz5}z + b_{caz5})y^2 + (a_{cbz5}z + b_{cbz5})y + (a_{ccz5}z^2 + b_{ccz5}z + c_{ccz5}) \tag{2.38}$$

In the working space of the levitation robot, the total magnetic field is the summation of the magnetic field produced by each coil. According to the Biot-Savart law, the magnetic field produced by coils is proportional to the current in the coils, so the magnetic field can be modeled as:

$$\begin{aligned}\mathbf{B}_z = \sum_{i=1}^{6} \mathbf{B}_{zi} = &\left(a_{1x}x^2 + b_{1x}x + c_{1x}\right) I_1 + \left(a_{2x}x^2 + c_{2x}\right) I_2 \\ &+ \left(a_{1x}x^2 - b_{1x}x + c_{1x}\right) I_3 + \left(a_{4x}x^2 + b_{4x}x + c_{4x}\right) I_4 \\ &+ \left(a_{5x}x^2 + c_{5x}\right) I_5 + \left(a_{4x}x^2 - b_{4x}x + c_{4x}\right) I_6\end{aligned} \tag{2.39}$$

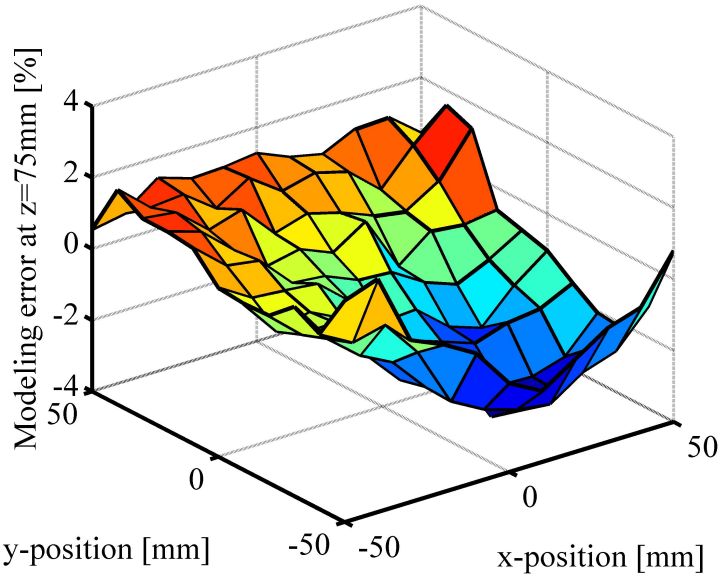

Figure 2.18: Modeling error of B_z at z=75mm

where $I_{1,2,...,6}$ are the currents in coils 1 to 6. The fitting model is validated experimentally when coil 1 and 2 are powered by 1A current at $z = 75mm$. The magnetic flux density B_z using the fitting model as well as measurement are shown in figure 2.17. The modeling error while coil 1 and 2 are powered is shown in figure 2.18. From the error surface plot, it shows that the fitting model is acceptable with modeling error less than 4% of the maximum 1.65mT magnetic flux density. Specifically, at the center of the working area, the modeling error indicates favorable accuracy.

2.6 Dynamics of Magnetic Levitation

The dynamics of the levitating magnetized object in the working volume can be analyzed using Newton's law. In the Cartesian coordinate system, the dynamics of the object in three directions are:

$$m\ddot{x} = F_x \tag{2.40}$$

$$m\ddot{y} = F_y \tag{2.41}$$

$$m\ddot{z} = mg - F_z \tag{2.42}$$

According to equation 2.18, 2.19, and 2.20, the force on a magnetized object in the working volume of the system is proportional to the gradient of z-component of the magnetic field where the robot stays. Using equation 2.39, the gradient of magnetic field in x and y directions is:

$$\begin{aligned}\frac{\partial B_z}{\partial x} =& \left(2xa_{1x} + b_{1x}\right) I_1 + 2xa_{2x} I_2 + \left(2xa_{1x} - b_{1x}\right) I_3 \\ &+ \left(2xa_{4x} + b_{4x}\right) I_4 + 2xa_{5x} I_5 + \left(2xa_{4x} - b_{4x}\right) I_6 \end{aligned} \tag{2.43}$$

$$\begin{aligned}\frac{\partial B_z}{\partial y} =& \left[2xy\left(a_{baz1}z + b_{baz1}\right) + x\left(a_{bbz1}z + b_{bbz1}\right) + 2y\left(a_{caz1}z + b_{caz1}\right) + a_{cbz1}z + b_{cbz1}\right] I_1 \\ &+ \left[2y\left(a_{caz2}z + b_{caz2}\right) + a_{cbz2}z + b_{cbz2}\right] I_2 \\ &+ \left[-2xy\left(a_{baz1}z + b_{baz1}\right) - x\left(a_{bbz1}z + b_{bbz1}\right) + 2y\left(a_{caz1}z + b_{caz1}\right) + a_{cbz1}z + b_{cbz1}\right] I_3 \\ &+ \left[2xy\left(a_{baz4}z + b_{baz4}\right) + x\left(a_{bbz4}z + b_{bbz4}\right) + 2y\left(a_{caz4}z + b_{caz4}\right) + a_{cbz4}z + b_{cbz1}\right] I_4 \\ &+ \left[2y\left(a_{caz5}z + b_{caz5}\right) + a_{cbz5}z + b_{cbz5}\right] I_5 \\ &+ \left[-2xy\left(a_{baz4}z + b_{baz4}\right) - x\left(a_{bbz4}z + b_{bbz4}\right) + 2y\left(a_{caz4}z + b_{caz4}\right) + a_{cbz4}z + b_{cbz4}\right] I_6 \end{aligned} \tag{2.44}$$

$$\begin{aligned}\frac{\partial B_z}{\partial z} =& \left(a_{ccz1}z + b_{ccz1}\right) I_1 + \left(a_{ccz2}z + b_{ccz2}\right) I_2 + \left(a_{ccz1}z + b_{ccz1}\right) I_3 \\ &+ \left(a_{ccz4}z + b_{ccz4}\right) I_4 + \left(a_{ccz5}z + b_{ccz5}\right) I_5 + \left(a_{ccz4}z + b_{ccz4}\right) I_6 \end{aligned} \tag{2.45}$$

From equation 2.43 and 2.44, we notice the nonlinear properties of the gradients, i.e., the coupling between position and currents in coils. The working area of the levitation is very small compared to the measurement space. Therefore, the model is linearized at the center $(0, 0, z_0, I_0)$ of the magnetized object's working volume using Taylor's series as:

$$\begin{aligned}\frac{\partial B_z}{\partial x} =& 2xI_0\left[2\left(a_{az1}z_0 + b_{az1}\right) + \left(a_{az2}z_0 + b_{az2}\right) + 2\left(a_{az4}z_0 + b_{az4}\right) + \left(a_{az5}z_0 + b_{az5}\right)\right] \\ &+ \left(a_{bcz1}z_0 + b_{bcz1}\right)\left(i_1 - i_3\right) + \left(a_{bcz4}z_0 + b_{bcz4}\right)\left(i_4 - i_6\right) \end{aligned} \tag{2.46}$$

$$\begin{aligned}\frac{\partial B_z}{\partial y} =& \left[2\left(a_{cbz1}z_0 + b_{cbz1}\right) + 2\left(a_{cbz4}z_0 + b_{cbz4}\right) + \left(a_{cbz2}z_0 + b_{cbz2}\right) + \left(a_{cbz5}z_0 + b_{cbz5}\right)\right] I_0 \\ &+ 2yI_0\left[\left(2a_{caz1} + a_{caz2} + 2a_{caz4} + a_{caz5}\right) z_0 + \left(2b_{caz1} + b_{caz2} + 2b_{caz4} + b_{caz5}\right)\right] \\ &+ \left(a_{cbz1}z_0 + b_{cbz1}\right) i_1 + \left(a_{cbz2}z_0 + b_{cbz2}\right) i_2 + \left(a_{cbz1}z_0 + b_{cbz1}\right) i_3 \\ &+ \left(a_{cbz4}z_0 + b_{cbz4}\right) i_4 + \left(a_{cbz5}z_0 + b_{cbz5}\right) i_5 + \left(a_{cbz4}z_0 + b_{cbz4}\right) i_6 \end{aligned} \tag{2.47}$$

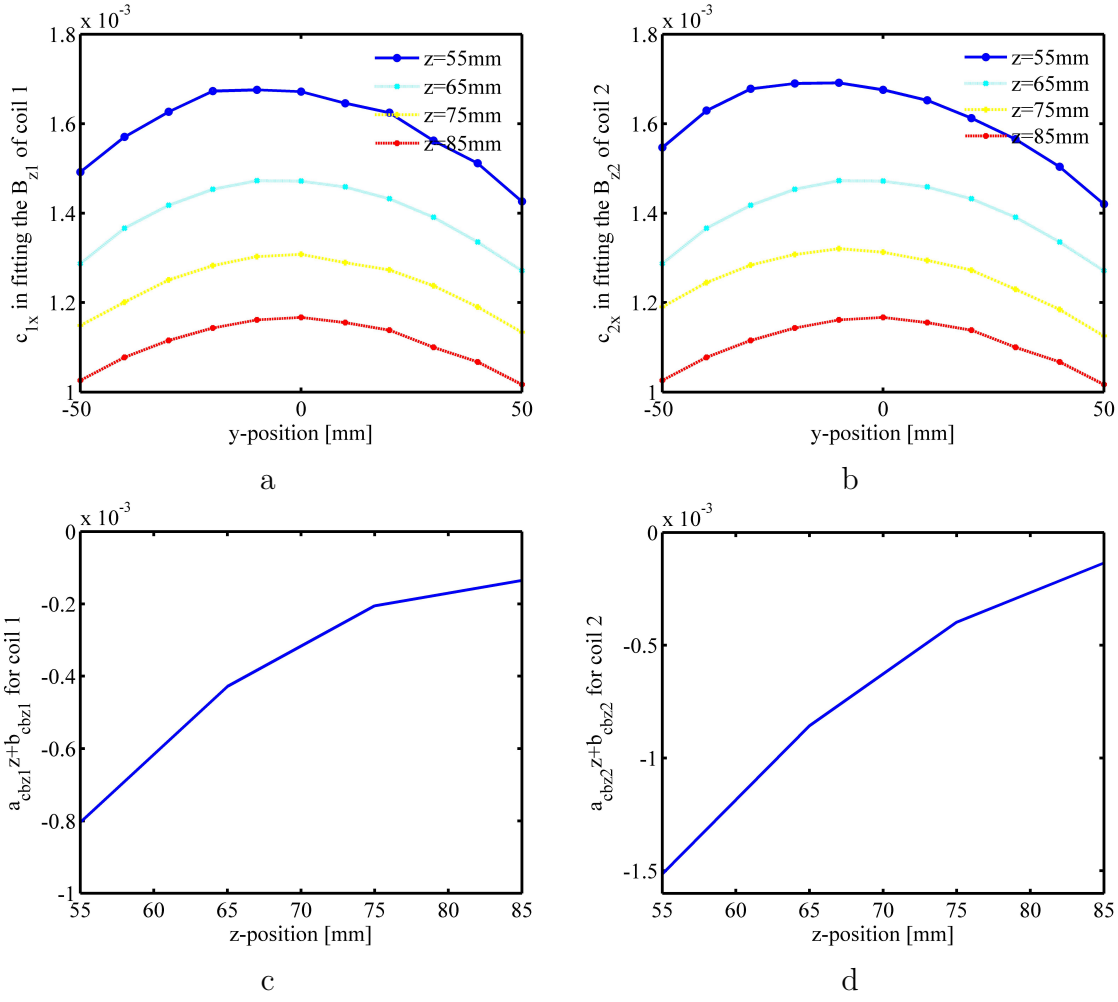

Figure 2.19: Coefficients of fitting model a) c_{1x} for fitting the z-component magnetic flux density while only coil 1 is supplied with 1A current, b) c_{2x} for fitting the z+-component magnetic flux density while coil 2 is supplied with 1A current, c) $a_{cbz1}z + b_{cbz1}$ in equation 2.47, d) $a_{cbz2}z + b_{cbz2}$ in equation 2.47

$$\frac{\partial B_z}{\partial z} = (a_{zz}z + b_{zz})\, I_0 + a_{zz} I_0\, (z - z_0) + (a_{zz}z_0 + b_{zz})\, (i_i + i_2 + i_3 + i_4 + i_5 + i_6) \quad (2.48)$$

where a_c, b_c are simplified coefficients.

Theoretically, it is reasonable to consider $a_{cbz1}z_0 + b_{cbz1} = -(a_{cbz4}z_0 + b_{cbz4})$, and $a_{cbz2}z_0 + b_{cbz2} = -(a_{cbz5}z_0 + b_{cbz5})$, since the geometric symmetric of coils 1, 2, 3 and

coils 4, 5, 6 with respect to x-z plane. From figure 2.19, it shows that $a_{cbz2}z_0 + b_{cbz2} \approx 2\left(a_{cbz1}z_0 + b_{cbz1}\right)$. Also $a_{bcz1}z_0 + b_{bcz1}$ can be considered the same as $a_{bcz4}z_0 + b_{bcz4}$ Then we can get models by simplifying equations 2.46 and 2.47:

$$\frac{\partial B_z}{\partial x} = 2xI_0\left(a_{xz}z_0 + b_{xz}\right) + \left(a_{xzi}z_0 + b_{xzi}\right)\left(i_1 - i_3 + i_4 - i_6\right) \tag{2.49}$$

$$\begin{aligned}\frac{\partial B_z}{\partial y} =& 2yI_0\left(a_{yz}z_0 + b_{yz}\right) \\ &+ \left(a_{yzi1}z_0 + b_{yzi1}\right)\left(i_1 + 2i_2 + i_3 - i_4 - 2i_5 - i_6\right)\end{aligned} \tag{2.50}$$

Substituting equations 2.49, 2.50, and 2.48 into equations 2.40, 2.41, and 2.42, the following second order dynamic models of the levitating magnetized object are given as:

$$\begin{aligned}m\ddot{x} =& P2xI_0\left(a_{xz}z_0 + b_{xz}\right) \\ &+ \left(a_{xzi1}z_0 + b_{xzi1}\right)\left(i_1 - i_3 + i_4 - i_6\right)\end{aligned} \tag{2.51}$$

$$\begin{aligned}m\ddot{y} =& P2yI_0\left(a_{yz}z_0 + b_{yz}\right) \\ &+ \left(a_{yzi1}z_0 + b_{yzi1}\right)\left(i_1 + 2i_2 + i_3 - i_4 - 2i_5 - i_6\right)\end{aligned} \tag{2.52}$$

$$m\ddot{z} = -a_{zz}I_0\left(z - z_0\right) - \left(a_{zz}z_0 + b_{zz}\right)\left(i_i + i_2 + i_3 + i_4 + i_5 + i_6\right) \tag{2.53}$$

where $P = MV$ is the total magnetization of the magnetized object integrated over its volume V.

2.7 Control of 3D Free Levitation

In this section, the method of controlling the levitation of a magnetized object in three directions is presented. Equation 2.42 indicates that the levitation in the vertical direction is internally unstable due to the presence of the gravity force. Therefore, feedback control is necessary for stable levitation. In this section, a combination of a feed-forward and a PID controller is studied. In free and stable levitation, there are gravity and magnetic forces on the robot. The magnetic force in the z-direction balances the gravity force. In the horizontal directions, there is no external force other than magnetic force. It is internally stable in the horizontal directions if the levitated robot stays at the minimum potential point.

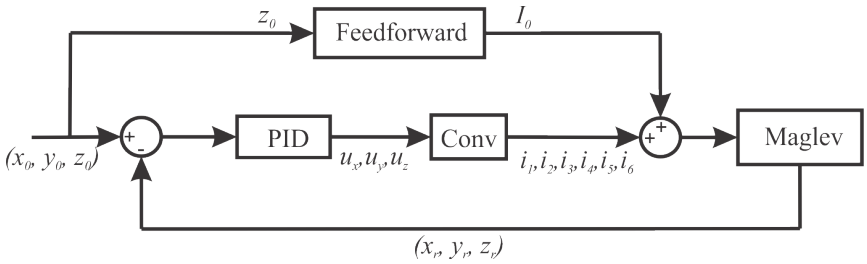

Figure 2.20: Schematic of control system

The control system is shown in figure 2.20. In this magnetic levitation system, the inputs to the levitation plant are currents in six-pair of coils. The feed-forward loop of the controller calculates the steady state current I_0 in all coils at specific levitation distances from the pole piece. From equation 2.42, the following expression is given while the levitation is stable:

$$mg = (a_{zc} z_0 + b_{zc})\, I_0 \tag{2.54}$$

which then gives the feed-forward current:

$$I_0 = \frac{mg}{a_{zc} z_0 + b_{zc}} \tag{2.55}$$

The control system schematic shows that the inputs to the plant are six different currents in six-pair of coils. However, there are only three outputs from the PID controller. Each PID output corresponds to one axis in the Cartesian coordinate system. The PID controller will adjust the currents in all coils. The parameters of the PID controller can be obtained by pole-placement or trial and error. From equations 2.40, 2.41, and 2.42, the following principle can be obtained:

$$\begin{bmatrix} u_x \\ u_y \\ u_z \end{bmatrix} = \underbrace{\begin{bmatrix} 1 & 0 & -1 & 1 & 0 & -1 \\ 1 & 2 & 1 & -1 & -2 & -1 \\ 1 & 1 & 1 & 1 & 1 & 1 \end{bmatrix}}_{\mathbf{A}} \begin{bmatrix} i_1 \\ i_2 \\ i_3 \\ i_4 \\ i_5 \\ i_6 \end{bmatrix} \tag{2.56}$$

The matrix A is not square. Its inverse matrix can not be calculated in a regular way. The pseudo-inverse method, which minimizes linear squared error, is applied in calculating

the conversion matrix to allocate the output of the PID controller into the input of each coils current. The conversion matrix using pseudo-inverse matrix is shown below:

$$\begin{bmatrix} i_1 \\ i_2 \\ i_3 \\ i_4 \\ i_5 \\ i_6 \end{bmatrix} = \underbrace{\begin{bmatrix} 0.25 & 0.0833 & 0.1667 \\ 0 & 0.1667 & 0.1667 \\ -0.25 & 0.0833 & 0.1667 \\ 0.25 & -0.0833 & 0.1667 \\ 0 & -0.1667 & 0.1667 \\ -0.25 & -0.0833 & 0.1667 \end{bmatrix}}_{\mathbf{Conv}} \begin{bmatrix} u_x \\ u_y \\ u_z \end{bmatrix} \tag{2.57}$$

The controller is implemented in the magnetic levitation system to realize the navigation of a small cylindrical permanent magnet in free space. The small permanent magnet has a $5mm$ diameter and a $5mm$ height. The remnant magnetic flux density B_r of the permanent magnet is $1.3T$. Since the diameter of the permanent magnet limits its horizontal translation range to $\begin{bmatrix} -5 & 5 \end{bmatrix} mm$, a special levitation robot was designed. The configuration of the robot is shown in figure 2.21. The new design of the robot extends the horizontal translation range to $\begin{bmatrix} -10 & 10 \end{bmatrix} mm$.

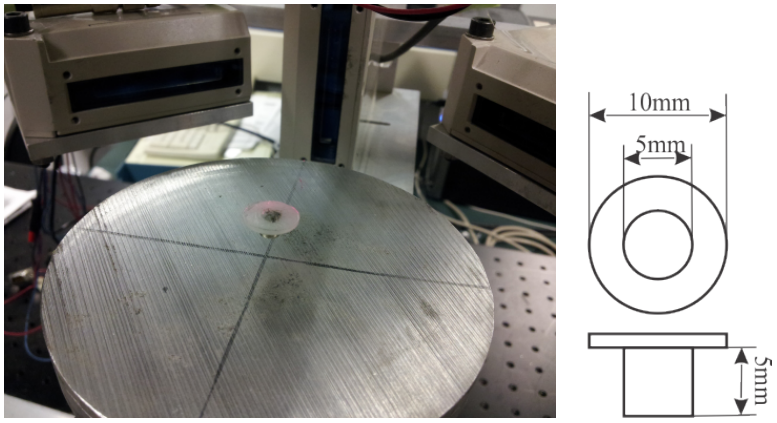

Figure 2.21: The new robot extends the horizontal translation range

The experimental results are shown in Figure 2.22. Experimental results show that the proposed controller works well in the working area. However, a cross-coupling effect also exists among the three axial motions. Specifically, the motion of the robot in the y-direction, which is the axis where the yoke is installed, affects the stability in the other

Table 2.1: Parameters of PID controllers

Controller	Kp	KI	KD
PID-x	1000	1500	0.1
PID-y	1000	1500	0.1
PID-z	450	2000	30

Table 2.2: Performance of PID controller

Parameter	Vertical	Horizontal
Rising Time [second]	0.055	2.55
Settling Time [second]	1.5	1.9
Overshoot [%]	35	0
Undershoot [%]	10	0

two directions. To solve this problem an LQG controller can be applied. Moein in [72] has already studied the use of an LQG controller to reduce the effect of cross-coupling. The PID parameters for three dimensional levitation are show in Table 2.1. Performance of the PID controller is shown in Table 2.2

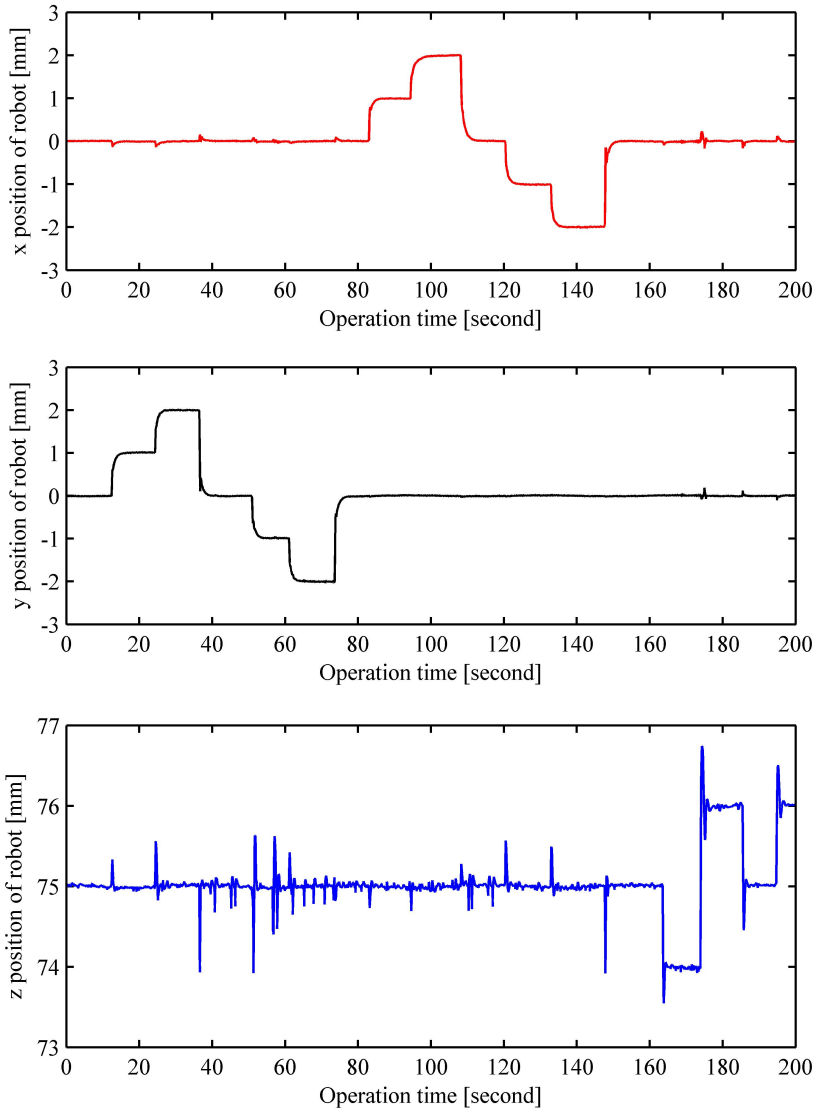

Figure 2.22: Three dimensional navigation of a small permanent magnet in free levitation

Chapter 3

Dual-axial Off-board Force on a Magnetized Object

This chapter introduces the principle and mechanism of determining the dual-axial contact force on a magnetically navigated microrobot (MNM) by measuring the magnetic flux density passing through the workspace using Hall-effect sensors. The MNM studied in this chapter is the same as the MNM described in the contribution clarification section in chapter 1. Due to the tiny size of the MNM and the remote manipulation property of levitation, it is very difficult to install an onboard sensor to measure the contact force on the microrobot. In addition, it is not energy efficient to levitate an extra mass. Therefore, an off-board force determination mechanism is proposed. By introducing the off-board force determination mechanism, we are able to calculate the contact force while the MNM is in contact with its environment. This in turn would help maintain a stable levitation and compliant touch. In the proposed method, no force sensor is directly attached to the microrobot. Its cost is extremely low. Here, the force mode in both x and y directions are analyzed and validated on a horizontal levitation plane. Due to the low sensitivity of the Hall-effect sensors and the inherent instability of levitation in the z-direction, which requires the dynamic information of the MNM, the magnetic flux measurement method cannot be used in z-direction navigation of the MNM. Therefore, the off-board force determination mechanism does not apply to the z-direction.

3.1 Dual-axial Motion Control Using Hall-effect Sensors

In this section, the technique of navigating the MNM using the magnetic flux measurement is firstly used to navigate a small permanent magnet in an optical beam block environment.

Stabilizing the inherent unstable dynamic of an MNM is one of the most important issues in the development of a magnetic levitation system. This can be achieved by regulating the current in the electromagnets based on position of the MNM or the electromagnets current feedback. Precision laser sensors are generally used for providing the position feedback of the MNM to the control system as an outer loop strategy. However, for a lower precision motion control a regulation of the electromagnets coil current can be used. To provide more robust position control both optical and current feedback can simultaneously be used as cascade control systems [98]. The optical-based device such as laser sensors or camera could provide sub-micron precision; however, they have limitation for operation in a non-transparent environment. For non-transparent working conditions, x-ray or ultrasound devices can be applied for the MNM navigation [13] [36]. The complexities, device cost, and environment restrictions (x-rays will be harmful to living cells and ultrasound penetration is environmentally depended) also limit the application of these devices for a redundant position determination system. The dynamics of the MNM can be controlled with an open loop strategy in a very limited workspace with low precision where there is the limitation of accurate position feedback such as optical blockage. However, the open-loop system is not appropriate for levitation systems with a huge number of electromagnets, since the magnetic field change is required to be modeled with change of current in each electromagnet.

To address the limitation of the optical blockage, use of magnetic flux measurement has a great deal of promise in determining the position of the MNM. Hall-effect sensors are generally used for magnetic flux measurement. So based on a measured magnetic flux, the location of a magnetized object can generally be determined. Additionally, the cost of a Hall-effect sensor is insignificant relative to a laser sensor, which decreases the implementation cost. Several studies were conducted on position measurement by means of using Hall-effect sensors to measure the magnetic field for the purpose of position determination. Such research includes: motor rotor angle estimation with hall sensors [7], two-dimensional position measurement of a moving magnet based on the direction of the magnetic field of the moving magnet [87], and 3-D rotor position prediction using three pairs of hall sensors for a magnetic bearing [108]. All of the listed applications used Hall-effect sensors to directly measure the field of a magnetized object in a small working air-gap between

the Hall-effect sensor and the object. For a magnetic actuation system with large air-gaps such as ours which is greater than 65 mm, it is very challenging to directly determine the location of the levitating magnetized object by measuring the magnetic field of the object. Particularly, the changing of the magnetic field of a small magnetized object is very difficult detect with a low sensitivity Hall-effect sensor at a distance greater than 65 mm. To solve this problem, Moein et al. in[74] proposed using the measured source magnetic field pattern in the working space to determine only the 1-D position of a small magnetized object.

This chapter is progress the study in [74], and a novel contribution is reported for determining the 2-D position of an MNM using the source magnetic field pattern in the working space [112]. In [74], a single-axis position determination mechanism has been reported. However, the complexity arises with the cross-coupling effect presents in a 2-D magnetic guided motion. A polynomial relation between the magnetic field pattern and the MNMs location was developed to reduce this effect. The order of the polynomial model was identified using the cross-validation method in the sense of minimum RMSE between the reference positions and the actual positions of the MNM. Moreover, a combined optical-magnetic position determination methodology is reported as another aspect of the novelty of this work in comparison with the previous study in [74].

3.1.1 Principle of Hall-effect Sensor Position Determination

In free levitation, the MNM stayed at the minimum potential energy point, which is the B_{max} point in the horizontal plane containing the MNM [75]. The lateral motion of the MNM was achieved by controlling the location of the B_{max} point horizontally in the working area. In this section, two examples are presented to show the concept of moving a single B_{max} point in 1-D and 2-D situations.

Figure 3.1 is an example of moving a single B_{max} in one direction. In this example, two electromagnets (N=840 turns) were connected by a soft iron pole-piece to produce a single B_{max} point at 78 mm below the pole-piece. In figure 3.1a, the currents in both coils were the same, so the B_{max} point stayed in the center between the two coils. In figure 3.1b, the currents in the two coils were different. The B_{max} point moved toward coil 1 which had more current. This example shows that by changing the current ratio in the two coils, the location of the B_{max} point could be changed. Similarly, 2-D motion of a single B_{max} point in a horizontal plane was achieved by tuning the currents in planar distributed electromagnets (N=840 turns). This was demonstrated by simulating the magnetic drive unit in the COMSOL Multiphysics software environment. The horizontal plane in consideration was located at z= 78 mm below the pole-piece. In figure 3.2a, all six coils were powered equally

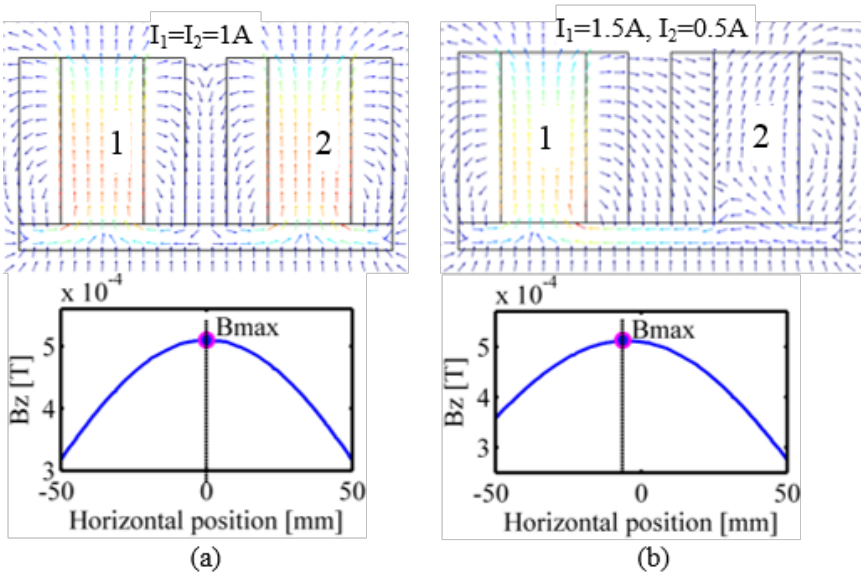

Figure 3.1: Changing the 1-D position of B_{max} point at 78 mm below the electromagnets: (a) the B_{max} was located in the center when the two coils were equally loaded, (b) the B_{max} point moved toward the coil that had more current[112]

with 1A dc current, so the B_{max} point was located at the center of the working space. In figure 3.2b, the location of B_{max} was changed to the third quadrant of the coordinate system by increasing the current in coils 2, 3, and 4 (figure 2.5), and decreasing the current in coils 1, 5, and 6 while keeping the total current $\sum_{i=1}^{6} I_i$ the same as in figure 3.2a.

Therefore, the location of B_{max} is related to the distribution of the magnetic field produced by electromagnets. If the magnetic field could be measured, the location of B_{max} in the horizontal plane could be determined,which in turn determined the location of the MNM.

3.1.2 Installation of Hall-effect Sensors

The installation of Hall-effect sensors plays a key role in the position determination technique. Figure 3.3 shows three different configurations of sensor installation (Inner, Mid, and Outer) where the distances between two Hall-effect sensors are 40 mm, 88 mm, and 120 mm, respectively. These three configurations were taken into consideration to optimize the performance of position estimation. The experimental results shown in figure 3.4 indicate that linear function can be fitted with Inner and Outer installation strategy, and third

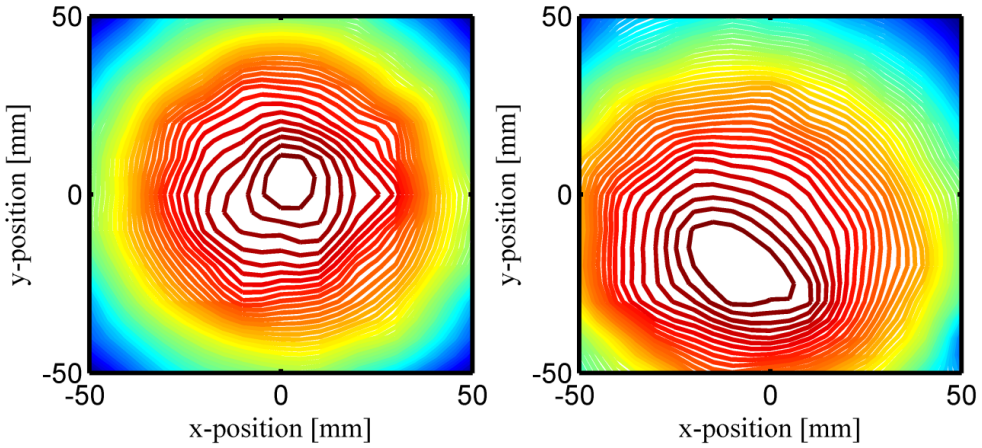

Figure 3.2: Changing the 2-D position of B_{max} point. This is the simulation result of the magnetic field at 78 mm below the pole-piece with different current ratio in electromagnets, but $\sum_{i=1}^{6} I_i$ was kept as constant: (a) $I_1 = I_2 = I_3 = I_4 = I_5 = I_6$, B_{max} was located at the center of the work area; (b) $2I_1 = 2I_5 = 2I_6 = I_2 = I_3 = I_4$, B_{max} was moved to the third quadrant[112]

order nonlinear function can be fitted with Mid installation. The results in [74] demonstrated that the Inner installation strategy had the best performance in that it provided minimum position estimation error.

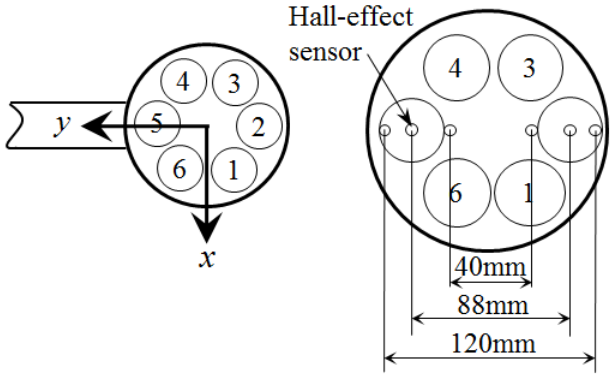

Figure 3.3: Configuration of Hall-effect sensors[112]

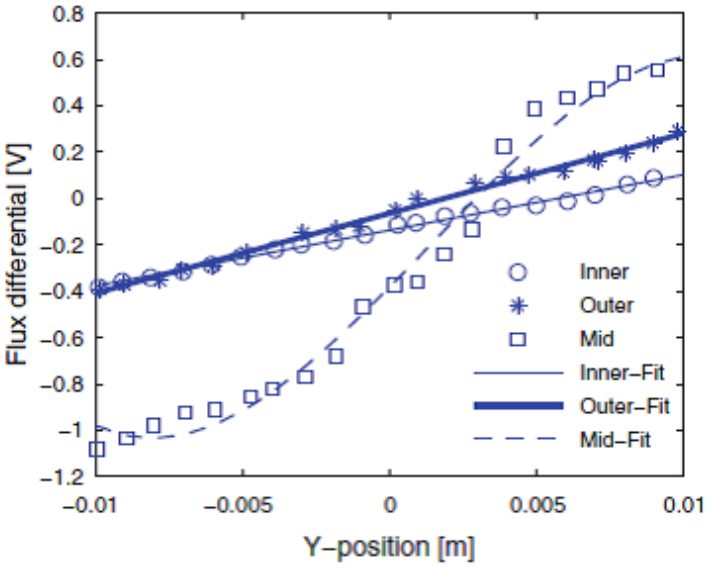

Figure 3.4: Performance of different Hall-effect sensor installation strategy [74]

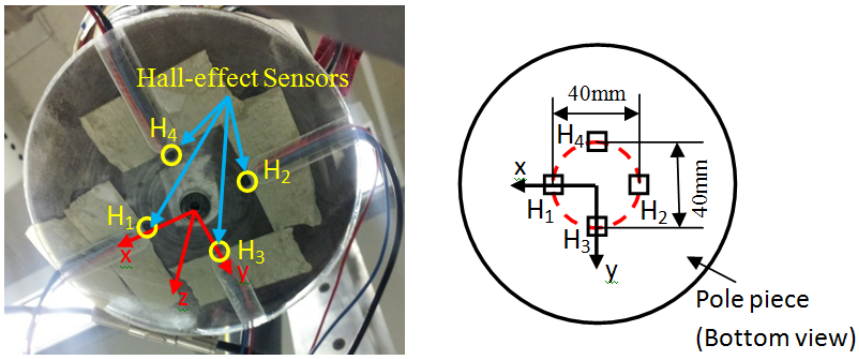

Figure 3.5: Installation of Hall-effect sensors in x and y directions (bottom view)[112]

As shown in figure 3.5, four Hall-effect sensors H1, H2, H3, and H4 were directly attached to the bottom of the pole-piece with the Inner installation strategy. H1, H2, H3, and H4 are the names of Hall-effect sensors as shown in figure 3.5. H1 and H2 were installed at two intersection points between the x-axis and a 40 mm diameter circle. H3 and H4 were installed at two intersection points between the y-axis and the same 40 mm diameter circle. The center of the circle was located at the center of the pole piece.

A linear Hall-effect sensor TLE4990, manufactured by Infineon, was used in the study.

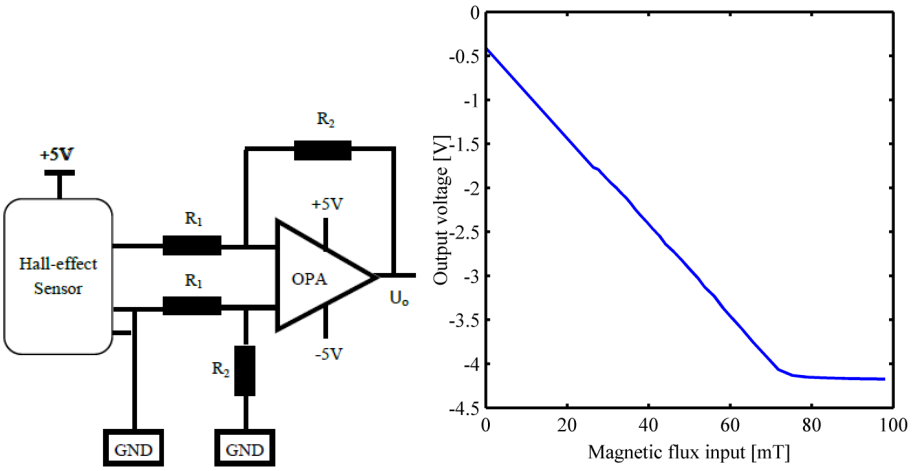

(a) (b)

Figure 3.6: (a) amplification circuit for Hall-effect sensor, (b) linear performance of selected Hall-effect sensor

The Hall-effect sensor had a linear working range of 13.5mT-204.5mT and 22mV/mT sensitivity. Its output in the linear working range was 0.3V-4.5V. During operation, the magnetic flux density leaked into the working space was 20mT-40mT, which was in the Hall-effect sensors lower working range. An amplifying circuit shown in figure 3.6a was designed to amplify the output of the Hall-effect sensor. The operational amplifier augments the output of the Hall-effect sensor with an amplification coefficient of 4.55. When the output of the Hall-effect sensor was 0.91 V, which corresponds to 70mT magnetic flux passing through the Hall-effect sensor, the output of the circuit saturated (figure 3.6b).

3.1.3 Mapping Between Magnetic Field Measurement and the MNM's Position

In this part, the process of determining the B_{max} point location in a horizontal plane using magnetic field pattern measurement is explained in detail. As discussed in section 4.2.1, the B_{max} point is the position of the MNM in free levitation situation. The position of the MNM can be measured using high resolution optical sensors, and the magnetic flux pattern in the working space can be described using the output of Hall-effect sensors. Therefore, the experimental method is feasible for developing a mapping model to estimate the location of the B_{max} point using the output of Hall-effect sensors and the accurate position of the MNM.

A laser position sensor system with $20\mu m$ resolution was used to control the motion of the MNM when the position of the MNM was collected during the measurement. The magnetic field pattern in the working space was described by the voltage output differential of Hall-effect sensors in both x- and y- directions. i.e., V_{dx} is the output voltage differential between H1 and H2 in the x-direction and V_{dy} is the output voltage differential between H3 and H4 in the y-direction. (H1, H2, H3, and H4 were defined in Section 4.2.2). During the measurement, the MNM was moved to 121 locations (11 by 11 points with displacement resolutions of 1 mm in both x and y directions) in a 10×10 mm^2 planar working area which located at 78 mm below the center of the pole-piece. There was one V_{dx} and one V_{dy} measurement at each location where the MNM was levitating. Therefore, 121 V_{dx} and 121 V_{dy} values were collected to define a mapping function.The measurement results are shown in figure 3.7. These figures indicate that the magnetic flux in the x-direction was symmetric with respect to y-z plane. However, it was asymmetric in the y-direction. This asymmetry was caused by the lower flux resistance of the soft iron yoke in the y-direction. Cross-coupling effect existed between these two directions. i.e., when the MNM was moving along the x-direction, not only the flux differential in x-direction was changed but also the flux differential in the y-direction was changed. The cross-coupling effect was intensified in areas that were far from the center of the working area.

The proposed mapping models are shown in equations 3.1 and 3.2. The inputs for both models were the output voltage differentials V_{dx} and V_{dy} of the Hall-effect sensors. In equation 3.1, the m^{th} order polynomial of V_{dx} and the n^{th} order polynomial of V_{dy} were mapped into the x-direction position estimation function. In equation 3.2, the r^{th} order polynomial of V_{dx} and the s^{th} order polynomial of V_{dy} were mapped into the y-direction position estimation function.

$$x = \begin{bmatrix} V_{dx}^{m} \\ \vdots \\ V_{dx}^{0} \end{bmatrix}^{\intercal}_{1\times(m+1)} \begin{bmatrix} 0 & \cdots & \cdots & 0 & p_{m0} \\ \vdots & \ddots & \ddots & p_{(m-1)1} & p_{(m-1)0} \\ \vdots & \ddots & \ddots & \vdots & \vdots \\ 0 & p_{1(n-1)} & \cdots & p_{11} & p_{10} \\ p_{0(n)} & p_{0(n-1)} & \cdots & p_{01} & p_{00} \end{bmatrix} \begin{bmatrix} V_{dy}^{n} \\ \vdots \\ V_{dy}^{0} \end{bmatrix}_{(n+1)\times1} \tag{3.1}$$

$$y = \begin{bmatrix} V_{dx}^{r} \\ \vdots \\ V_{dx}^{0} \end{bmatrix}^{\intercal}_{1\times(r+1)} \begin{bmatrix} 0 & \cdots & \cdots & 0 & q_{r0} \\ \vdots & \ddots & \ddots & q_{(r-1)1} & q_{(r-1)0} \\ \vdots & \ddots & \ddots & \vdots & \vdots \\ 0 & q_{1(s-1)} & \cdots & q_{11} & q_{10} \\ p_{0(s)} & p_{0(s-1)} & \cdots & q_{01} & q_{00} \end{bmatrix} \begin{bmatrix} V_{dy}^{s} \\ \vdots \\ V_{dy}^{0} \end{bmatrix}_{(s+1)\times1} \tag{3.2}$$

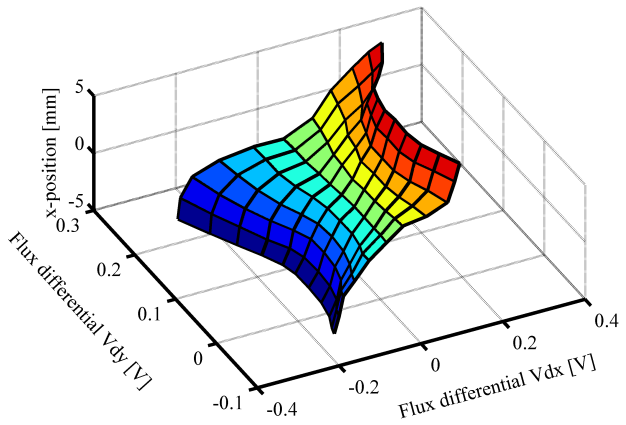

(a)

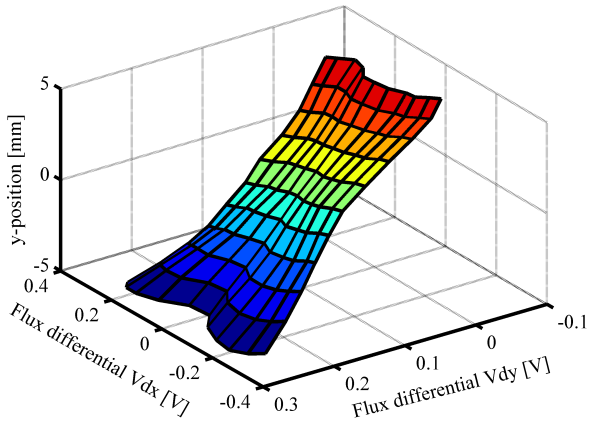

(b)

Figure 3.7: Surface plot of measurements: (a) flux differential in x- and y- direction vs. x-position; (b) flux differential in x- and y-direction vs. y-position [112]

where x and y are the estimated positions using the magnetic field measurement. $V_{dx}^{i}(i = 1, 2, ...n(m))$ is the i^{th} order of voltage differential in the x-direction. $V_{dy}^{j}(i = 1, 2, ...n(m))$ is the j^{th} order of voltage differential in the y-direction. p_{ij}, q_{kl} are the co-

efficients of mapping functions. For example, p_{ij} is the coefficient of the product of i^{th} order V_{dx} and j^{th} order V_{dy} in the x-direction position determination function. Similarly, q_{kl} is the coefficient of the product of the k^{th} order V_{dx} and l^{th} order V_{dy} in the y-direction position determination function. Coefficients of both mapping functions could be easily calculated in Matlab, if the orders of the mapping models were determined.

Cross-validation was demonstrated to be an efficient method in model selection [5]. In this study, 10-folds cross-validation method was used to select the best mapping orders. The root mean square errors (RMSE) of position prediction models using training data and testing data were compared to make a decision on the order of mapping model. The results are shown in figure 3.8. Figure 3.8a is the RMSE of the x-direction mapping model. Figure 3.8b is the RMSE of the y-direction mapping model. It can be concluded from the cross-validation results that a fourth order polynomial model is a reasonable choice for position determination in both x- and y-directions. The RMSE on the test data in the y-direction stopped decreasing at fourth order polynomial model and started increasing at fifth order. The RMSE on the test data in the x-direction did not reduce much after fourth order and started increasing at sixth order.

3.1.4 Experimental Validation

In this section, the proposed position determination method was validated experimentally. The proposed position determination mechanism in this paper is an open-loop strategy. An open-loop control of the vertical direction levitation of the Maglev system is internally unstable due to the presence of gravity. The stable levitation in this direction requires the MNMs dynamic information which can be obtained from sensors. However, the levitation system in this study is a large air-gap system, and the sensitivity of Hall-effect sensors decreases drastically with distance. The Hall-effect sensors cannot detect the MNMs magnetic field owing to the interference of electromagnets [61], therefore, laser sensor is used for z-axis motion control. In the future, if ultra-high sensitive Hall-effect sensors are provided to the system, 3-D motion control can be achieved in the same way. The 2-D position estimation method in this paper was validated in a horizontal plane at z=78 mm below the pole-piece. Before executing experiments in the horizontal plane, the MNM should be levitated to z=78 mm using laser sensor feedback systems.

The MNM in this study was a cylindrical PM with 10 mm diameter, and 10 mm height. The mass of the PM was 0.01kg. The remenant magnetic flux density of the PM is 1.3T. The schematic of the proposed control system is shown in figure 3.9. As shown in this figure, the laser sensors for horizontal position determination were replaced with Hall-effect sensor and position determination models.

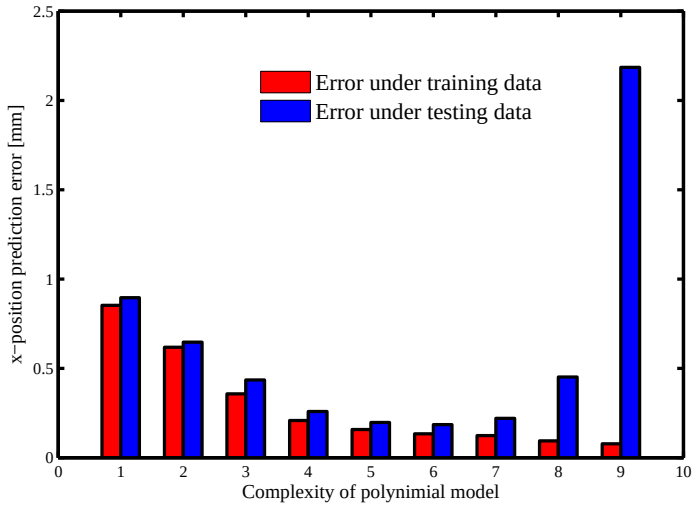

(a)

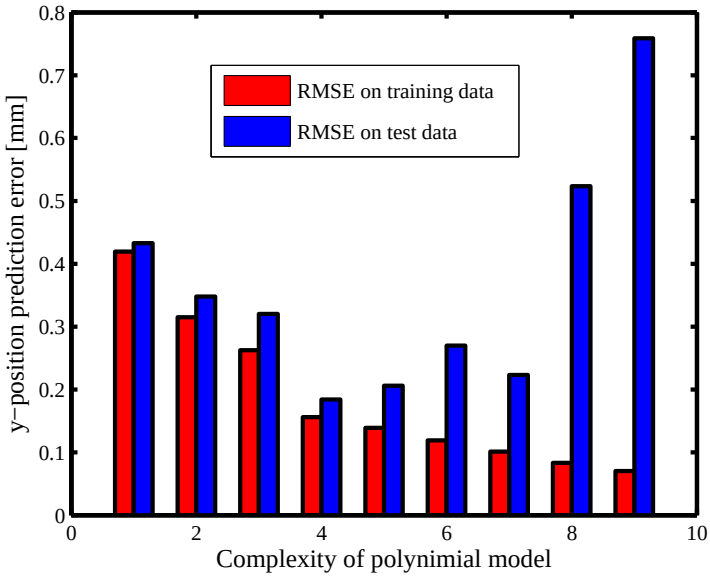

(b)

Figure 3.8: RMSE of x- and y-direction mapping models using 10-folds cross-validation method: (a) RMSE in x-direction, (b) RMSE in y-direction [112]

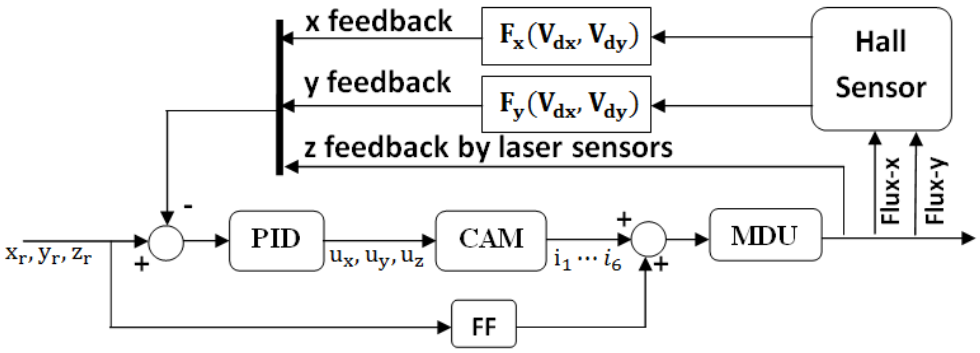

Figure 3.9: Schematic diagram of proposed 2-D Hall-effect sensor feedback control [112]

A PID feed-forward controller was applied to control the motion of the MNM. Mapping models were implemented in the control system to predict the x- and y-direction position of the MNM. The Hall-effect sensors measured the magnetic field in the working space. The measurement was then fed to the polynomial mapping model. The mapping models calculated the x- and y-direction position based on the measured flux differential. Then the calculated position was fed back to the controller to form a closed loop position controller. Sampling rate of the control system was 0.001s. The PID parameters used in the experiment are shown in Table 3.1.

Table 3.1: PID Parameters used in the experiment

Controller	x-axis	y-axis	z-axis
KP	200	200	85
KI	300	300	100
KD	1	1	6000

The performance of selected fourth-order models in each axis were validated experimentally by moving the robot by steps in two axial directions: 1) moving the robot by 1 mm step in the x-direction from -5 mm to +5 mm, while keeping y at a constant position 0 mm; 2) moving the robot by a 1 mm step along the y-direction from -4 mm to +4 mm, while keeping x at a constant position 0 mm. The experiment results are shown in figure 3.10.

As can be seen in figure 3.10, less vibration was observed at working points which are close to the center of the working area. At working points far from the center, huge error

occurred in the y-direction. The error made the levitation stopped at 4 mm from the center. The huge error at far working points was caused mainly by the modeling error and the low resolution of Hall-effect sensors.

Figure 3.11 shows the RMS error plots of experiments (a) and (b) shown in figure 3.10. The RMSE was calculated at all steady levitation points in the step response experiment shown in figure 3.10. Figure 3.11 shows that in the interval of [-4 4] mm along both x- and y-directions the RMS error of position estimation was less than 0.4 mm. Corresponding to the tracking experiments, large RMS error in both x- and y-directions occurred at operating points far from the center.

One important application of the proposed position determination mechanism is restoring the navigation of the MNM in cases when the laser beam is blocked by environments. The high-accuracy laser beam position measurement system is used when there is no laser beam blockage.

In another experiment, the proof-of-concept of switching the laser sensor based navigating mechanism to the magnetic flux based navigation method was evaluated. The configuration of the laser sensor system of the maglev system is shown in figure 3.12. The laser sensors system is composed of three pairs of laser sensors L1, L2, and L3. L3 measures the z-direction position. L1 and L2 are used to measure the horizontal position of the MNM. $x_p - y_p$ is the laser sensor coordinate. $x_m - y_m$ is the MNM coordinate system. The position of the MNM in the $x_m - y_m$ plane is determined by the outputs of both L1 and L2 using the following expressions:

$$\begin{cases} x_m = sin\frac{\pi}{4}(x_p - y_p) \\ y_m = -sin\frac{\pi}{4}(x_p + y_p) \end{cases} \tag{3.3}$$

$$\begin{cases} x_p = 2V_{L1} - 6 \\ y_p = 2V_{L2} - 6 \end{cases} \tag{3.4}$$

where V_{L1} and V_{L2} are the output voltages of L1 and L2.

In this experiment, the MNM was navigated along the y_m axis, and was kept at x_m=0 mm in the x_m axis, and at z=78 mm in the z_m axis. The position of the MNM can be measured by the laser sensor at the positive y_m axis. However, the magnetic flux position determination method was switched on when the MNM was moved to the negative y_m axis since the laser beam of L_2 was blocked by the environment near the y_m=0 mm location.

The experimental result is shown in figure 3.13. From start to 100 seconds, the MNM was navigated in the negative y_m axis (from 0 mm to -3 mm). The magnetic flux position

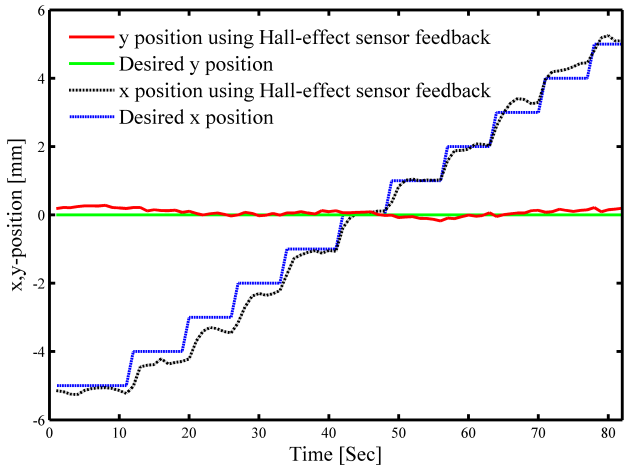

(a)

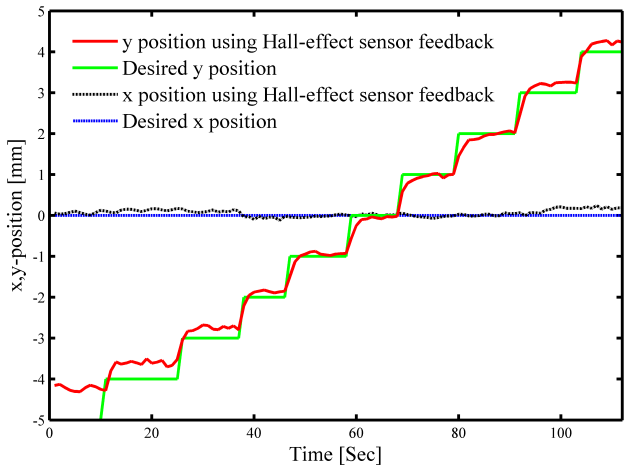

(b)

Figure 3.10: Tracking control using magnetic field measurement based position determination method: (a) The MNM was moved along the x axis, while keeping y at 0; (b) The MNM was moved along the y axis, while keeping x at 0 [112]

mechanism was switched on in this time period. After 100 seconds, the MNM was navigated in the positive y_m axis by laser sensors (from 0 mm to +3 mm). The position determination mechanisms were switched automatically by detecting the output of L_2. If the output of L_2 was constant, the system was switched to magnetic flux measurement method. The

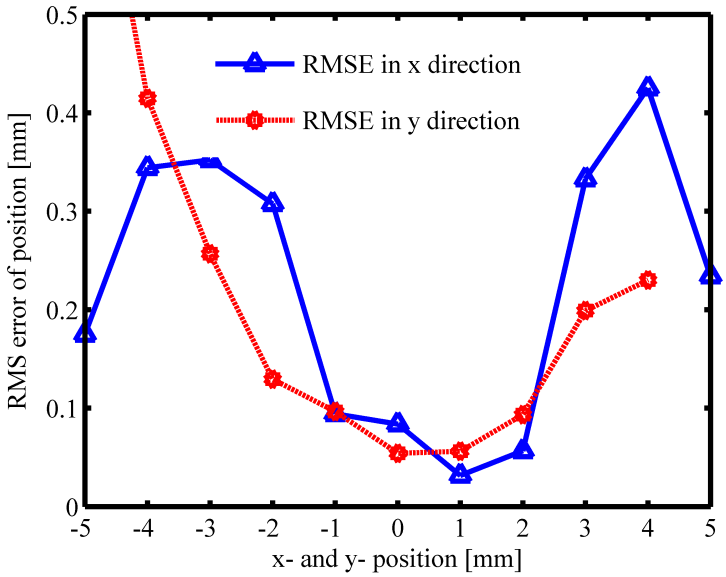

Figure 3.11: RMSE of horizontal position tracking using magnetic field measurement based fourth order polynomial position determination model [112]

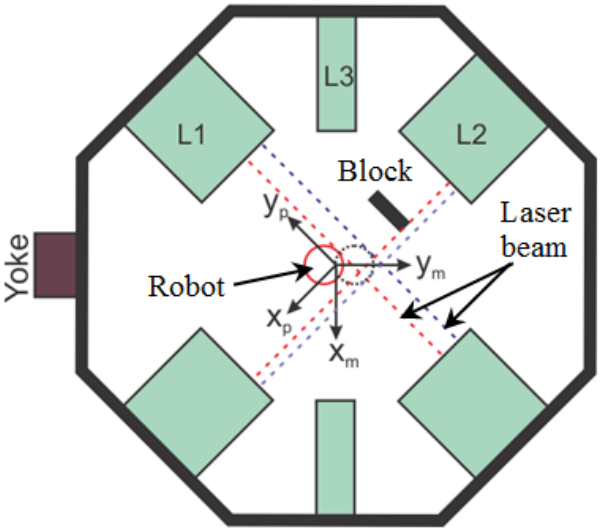

Figure 3.12: Configuration of laser sensors system[112]

output of L_2 in this experiment is shown in figure 3.14. It is shown that the output of L_2 is constant when its laser beam is blocked. Figure 3.15 shows photo shoots of the real process of navigating the MNM with laser beam blockage.

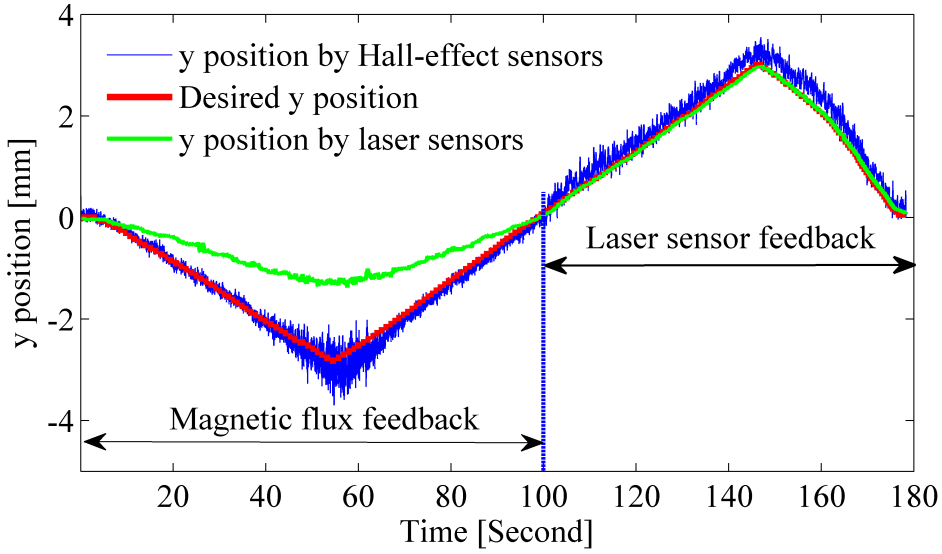

Figure 3.13: Experiment result of navigating the MNM from y_m=-3 mm to y_m= +3 mm. From start to 100 seconds, the MNM was navigated using magnetic flux feedback. From 100 seconds to the end, the MNM was navigated using laser sensor position feedback.[112]

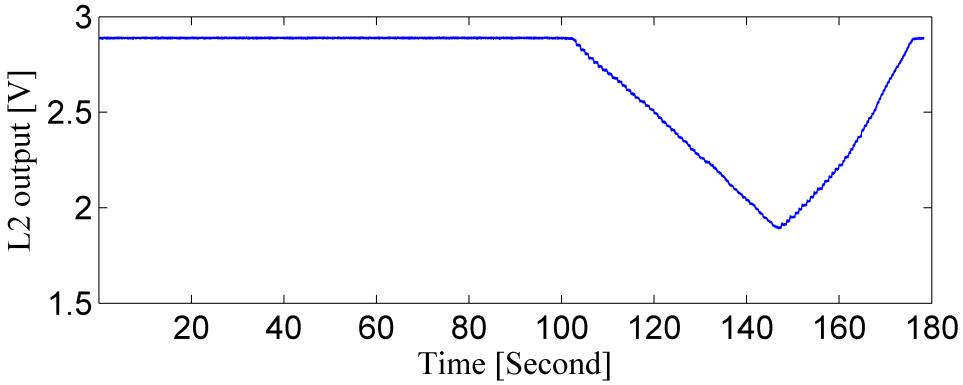

Figure 3.14: L_2 laser sensor output in the sensor switching experiment[112]

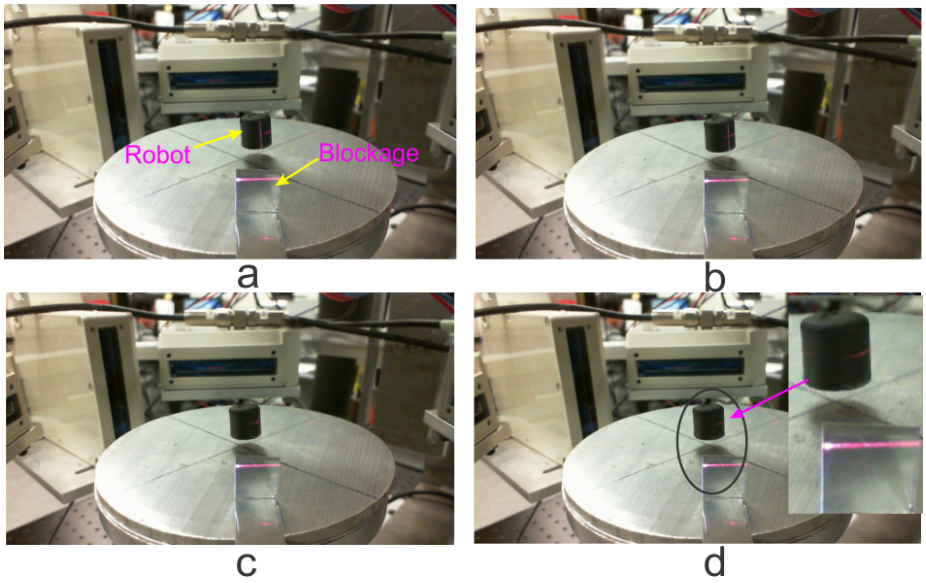

Figure 3.15: Photo shoots of the process of navigating the MNM in y axis. a) the MNM was located at y_m= -3 mm. L2 shot no laser beam on the MNM at this position; b) the MNM was located at y_m= -1 mm. L2 shot no laser beam on the MNM at this position; c) the MNM was located at y_m= 1 mm. L2 shot laser beam on a small area of the MNM at this position; d) the MNM was located at y_m= 2 mm. At this position, L2 shot laser beam on a larger area of the MNM.[112]

3.2 Dual-axial Off-board Force Determination Using Magnetic Flux Measurement

3.2.1 Principle of Off-board Force Determination

In the steady state of a contact-free levitation, the levitated microrobot stays at the minimum magnetic potential energy point on a horizontal plane. This minimum magnetic potential energy point is the location of B_{max} Point (x_{max}, y_{max}). However, when the microrobot is in contact with its environment, the microrobot is not stabilized at the B_{max} position. In this situation, the environment exerts contact force on the microrobot. The contact force hinders the MNM from being navigated to the B_{max} point. Meanwhile, the magnetic field produced by the magnetic drive unit exert an equal and opposite magnetic force that tries to move the microrobot toward the B_{max} point. Figure 3.16 explains the principle of off-board force determination. First the MNM is commanded to navigate to

the desired B_{max} point. However, owing to the existence of the obstacle, the real position of the MNM is different from the desired B_{max} location. The principle is that the contact force on the microrobot is linear to the distance between the real position of the levitated microrobot and the location of the B_{max} point.

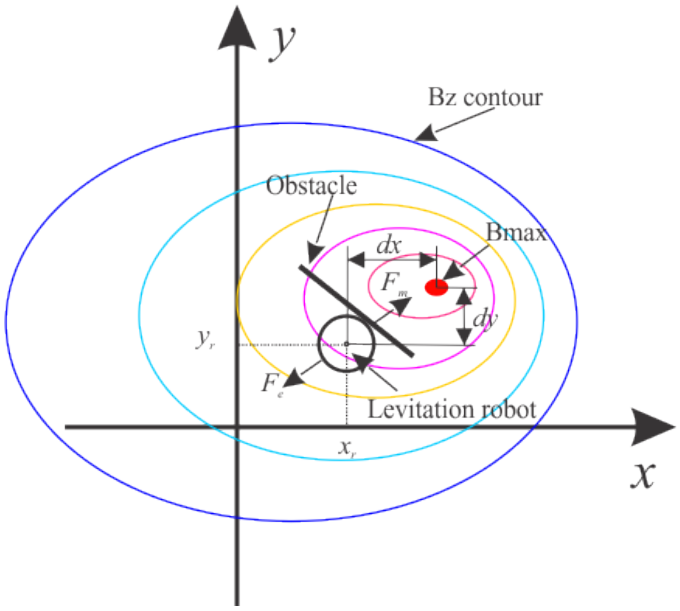

Figure 3.16: The concept of determining dual-axial forces on the MNM in a horizontal plane

3.2.2 Magnetic Force Modeling

Using equations 2.18, 2.19, 2.43, and 2.44, and applying simplification based on geometry symmetry, when the MNM is levitated at (x, y, z_0) in the workspace, the horizontal magnetic forces on the environment can be modeled as:

$$
\begin{aligned}
F_x = P\frac{\partial B_z}{\partial x}\,|_{(x,y,z_0)} = & 2x\left[a_{1x}(I_1+I_3+I_4+I_6)+a_{2x}(I_2+I_5)\right] \\
& + y^2\left(a_{baz1}z_0+b_{baz1}\right)\underbrace{(I_1-I_3-I_4+I_6)}_{Cx_{max}} \\
& + y\left(a_{bbz1}z_0+b_{bbz1}\right)\underbrace{(I_1-I_3+I_4-I_6)}_{0} \\
& + \left(a_{bcz1}z_0+b_{bcz1}\right)(I_1-I_3-I_4+I_6)
\end{aligned} \tag{3.5}
$$

$$
\begin{aligned}
F_y = P\frac{\partial B_z}{\partial y}\,|_{(x,y,z_0)} = & 2xy\left(a_{baz1}z_0+b_{baz1}\right)\underbrace{(I_1-I_3-I_4+I_6)}_{Cx_{max}} \\
& + x\left(a_{bbz1}z_0+b_{bbz1}\right)\underbrace{(I_1-I_3+I_4-I_6)}_{0} \\
& + 2y\left[\left(a_{caz1}z_0+b_{caz1}\right)(I_1+I_3+I_4+I_6)+\left(a_{caz2}z_0+b_{caz2}\right)(I_2+I_5)\right] \\
& + \left[\left(a_{cbz1}z_0+b_{cbz1}\right)(I_1+I_3+I_4+I_6)+\left(a_{cbz2}z_0+b_{cbz2}\right)(I_2+I_5)\right]
\end{aligned} \tag{3.6}
$$

From figure 3.16, the real position of the MNM can be expressed as $(x_{max}+dx, y_{max}+dy, z_0)$. Substituting the new position expression into equations 3.5 and 3.6, and applying zero force at the B_{max} point, the following expressions are obtained:

$$
\begin{aligned}
F_x = & 2dx\left[a_{1x}(I_1+I_3+I_4+I_6)+a_{2x}(I_2+I_5)\right] \\
& + (2y_{max}dy+dy^2)a_{b1x}Cx_{max}
\end{aligned} \tag{3.7}
$$

$$
\begin{aligned}
F_y = & 2a_{b1x}Cx_{max}y_{max}dx \\
& + 2dy\left[a_{c1x}\left(I_1+I_3+I_4+I_6\right)+a_{c2x}\left(I_2+I_5\right)+2x\right]
\end{aligned} \tag{3.8}
$$

According to equations 2.51, 2.52, and 2.53, at $z = z_0$ levitation plane, the magnetic levitation system holds the following constraints:

$$
I_1+I_2+I_3+I_4+I_5+I_6 = C_1 \tag{3.9}
$$

$$I_2 + I_5 = C_2 \tag{3.10}$$

Then the mangetic force model can be simplified as:

$$\begin{aligned} F_x =& 2dx\left[a_{1x}(C1 - C2) + a_{2x}C2\right] + C_{x2}x_{max}ydy \\ =& C_{x1}dx + C_{x2}x_{max}ydy \end{aligned} \tag{3.11}$$

$$\begin{aligned} F_y =& 2dy[a_{c1x}(C1 - C2) + a_{c2x}C2 + 2x] + C_{y1}x_{max}y_{max}dx \\ =& C_{y1}x_{max}y_{max}dx + (C_{y2} + 4x)dy \end{aligned} \tag{3.12}$$

In equations 3.11 and 3.12, parameters C_{x1}, C_{x2}, C_{y1}, and C_{y2} are constant at a specific levitation height z_0. These parameters can be identified off line by introducing a cantilever force sensor in the experiment. The force model indicates that the magnetic force on the robot is related to the B_{max} point location, MNM real position, and their difference. As discussed in the previous chapter, the B_{max} point can be determined using the magnetic flux based position determination method. In this levitation system setup, the real position of the MNM is measured using high precision laser beam position sensors. In the following section, the magnetic force models are validated experimentally.

3.2.3 Force Calibration and Experimental Validation

In order to validate the dual-axial force model proposed in the above section, two high-accuracy laser sensors and two aluminum alloy cantilevers are used to measure the real contact force. The mechanism of force measurement is shown in figure 3.17. In this figure, l_x and l_y are laser beam sensors used to detect the deflection of the cantilever beam in the x and y directions. dx, dy are the deflection of the cantilever.

The current facilities in the Magnetic microrobotic lab only satisfy one directional force model validation at one time. We validate the model in y-direction. The force model validation in the x-direction can be done in the same way. In the validation experiment, the MNM is kept at x=0 and z= 78 mm below the pole piece. The force in x-direction $F_x = 0N$ and the B_{max} location in x-direction is $x_{max} = 0mm$. For this working condition, as per figure 3.4, the position determination model is simply a linear model and not a higher order polynomial equation. New fitting data is plotted here in figure 3.18. As shown in the linear plot, the B_{max} location in the y axis can be calculated based on:

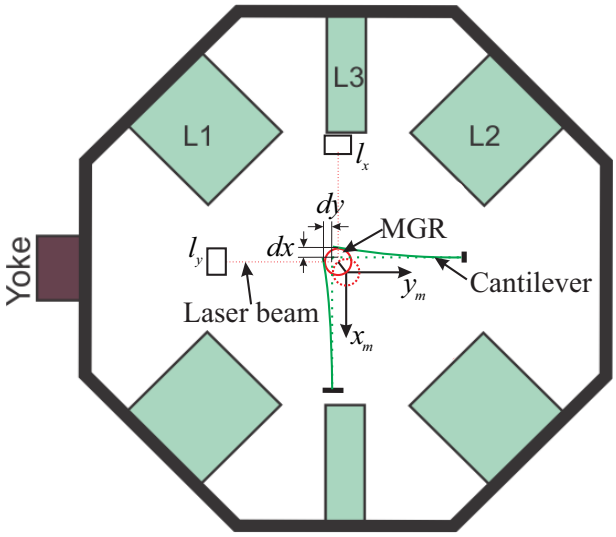

Figure 3.17: The mechanism of magnetic force measurement in 2D situation using two sets of laser beam deflection sensors

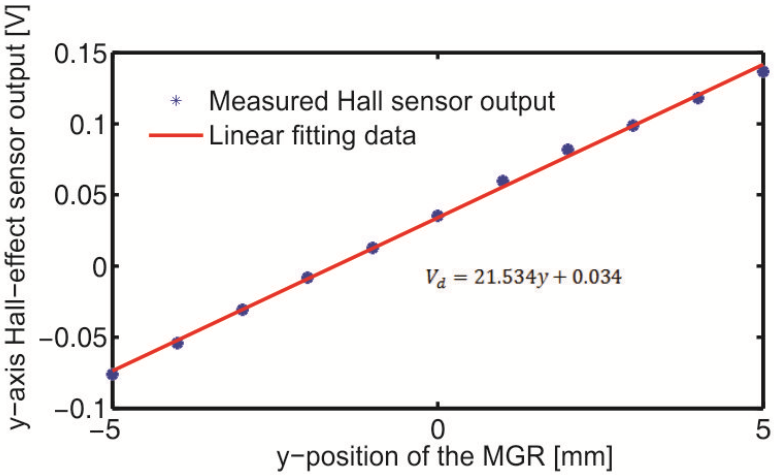

Figure 3.18: Linear fitting of hall-effect sensor output

$$y_{max} = aV_{dy} + b \tag{3.13}$$

Then the force model F_y is modified as:

$$F_y = C_{y2}dy \tag{3.14}$$

where $dy = y_r - y_{max}$ is the distance between the B_{max} point and the MNM's real position.

The experimental setup is shown in figure 3.19a. During the procedure of identifying the force model, an Aluminum alloy 1200 cantilever was used as force sensor. The dimension of the cantilever is $60mm \times 3mm \times 0.0762mm$. A high accuracy laser-beam sensor is used to measure the deflection of the cantilever at its tip.

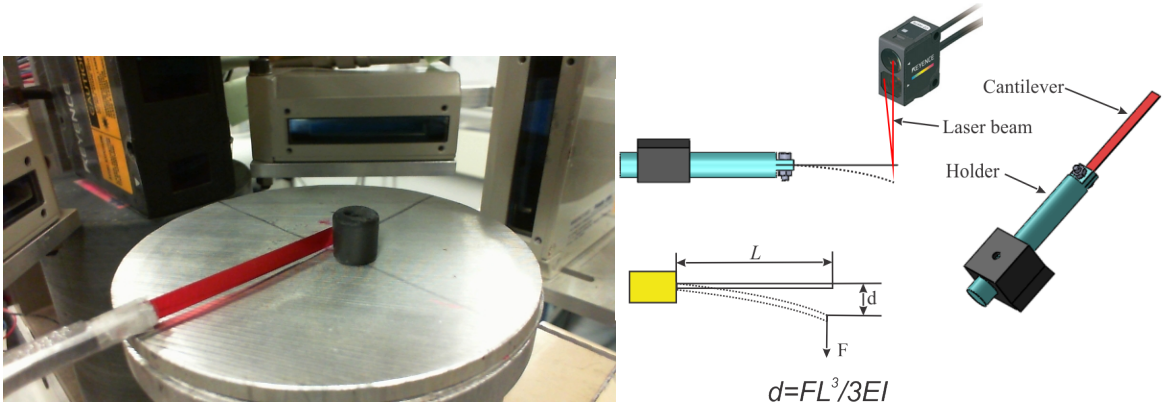

(a) (b)

Figure 3.19: (a) Experiment setup for identifying contact force model parameter using aluminum cantilever and (b) Principle of measuring force using a cantilever

The mathematic equation for calculating the force on a cantilever beam based on its deflection is:

$$F = \frac{3dEI}{L^3} \tag{3.15}$$

where d is the deflection of the cantilever beam, E is the elastic modulus of aluminum alloy 1200, I is the area moment of inertial, and L is the length. The accuracy of measuring force using a cantilever beam depends on the accuracy of the deflection measurement using the laser beam sensor and also depends on the accuracy of locating the deflection measurement point on the cantilever.

In the experiment, the MNM is commanded to push the cantilever in 3 steps and then come back to the zero position in 4 steps. The original location of the cantilever is $y = -0.3mm$. So the MNM and the cantilever are already in contact with each other when the MNM is located at $y = 0mm$. The deflection of the cantilever beam is $d = 0.3mm$ (figure 3.20). The contact force on the cantilever is plotted in figure 3.22. The accuracy of

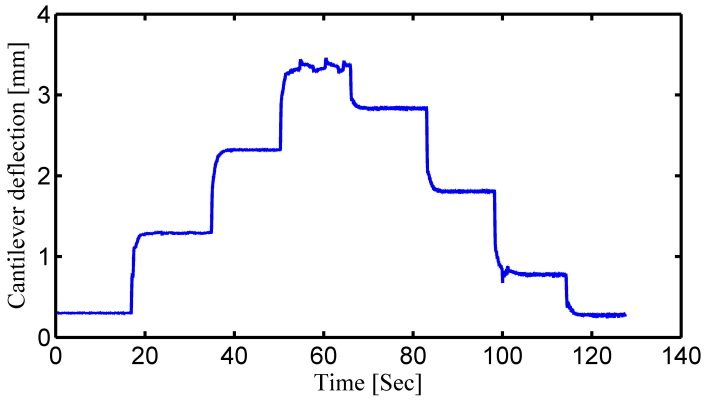

Figure 3.20: Deflection of cantilever in the force compare experiment

the cantilever deflection force is $5\mu N$. Using the Hall-effect sensors output in y-direction and equation 3.13, the y_{max} position is compared to the real MNM position in figure 3.21. Combining the measured contact force using the cantilever, the calculated y_{max}, and the MNM's real position, the magnetic force is calculated using equation 3.14. The calculated force shown in figure 3.22 has an accuracy of $2\mu N$. The coefficient value in equation 3.14 is $C_{y2} = 0.1036$. The accuracy of magnetic force determination using the magnetic flux measurement can be further improved by improving the mapping between hall-effect sensor output and measured force using the cantilever beam. For example, using a high sensitivity Hall-effect sensor and a more accurate cantilever beam deflection model can improve the accuracy of force determination.

The proposed force determination method is also validated in the x direction while the levitated microrobot is kept in the y=0 line at the horizontal plane of $z = 78mm$. The force measurement and the force calculation is compared in figure 3.23. The accuracy in the x direction force is 0.54 μN.

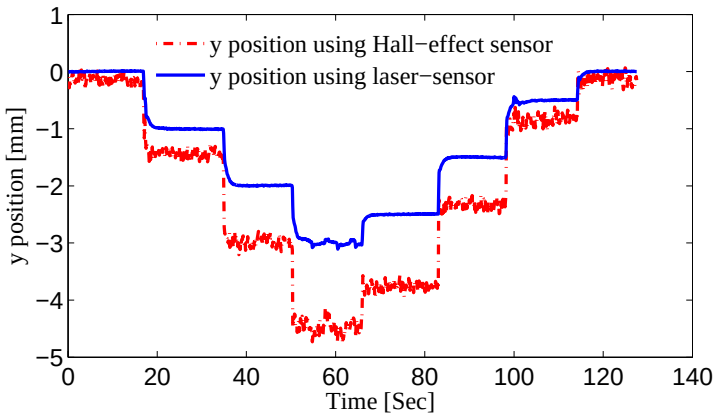

Figure 3.21: B_{max} position using magnetic flux measurement and the real position of MNM using laser-beam sensors

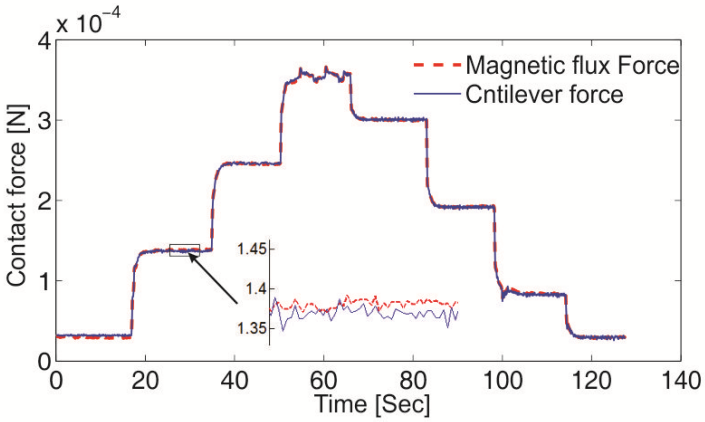

Figure 3.22: Comparison between measured force based on cantilever deflection and calculated force based on distance between B_{max} location and MNM real position

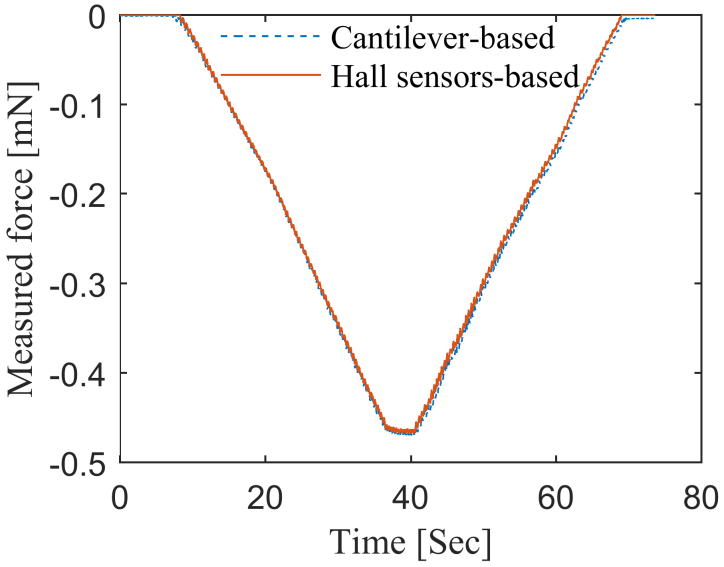

Figure 3.23: Force determination model validation in the x direction[111]

Chapter 4

Cooperative Operation using a Magnetic Navigated Microrobot and a Motorized Micromanipulator

4.1 Introduction

This chapter presents the cooperative manipulation using the magnetic navigated microrobot described in the contribution section of chapter 1. The system developed in this chapter aims to realize a compliant and dexterous manipulation of small objects in a confined space. In the current study, we used a magnetically navigated microrobot (MNM) and a motorized micromanipulator (MM) to perform cooperative manipulation. To achieve this goal, we need to solve the following issues: 1) measuring the contact force when the MNM is holding the object without installing a force sensor, and 2) controlling the holding force on the object during the manipulation.

The MNM studied in this chapter is the same as the MNM described in the contribution clarification section in chapter 1. The MNM is remotely manipulated without any mechanical connection between the end-effector and its drive unit. Therefore, it is challenging to install an on-board force sensor. The off-board force determination mechanism presented previously is used in this chapter.

Another issue in micromanipulation using the MNM and the MM is maintaining a proper holding force on the manipulated object. The holding force is known as the internal force [9]. Several approaches have been proposed to address the issue for multi-manipulator systems [50][28][35]. Fundamentally, it simultaneously controls the motion and the internal

holding force of the manipulated object. Researchers in [40] have considered the external contact force between the manipulated object and its environment. However, this is not the case for the current paper, as we manipulate the object in air media (free space). A position-based impedance controller is used in this research to regulate the contact force between the MNM and its environment.

4.2 System Setup

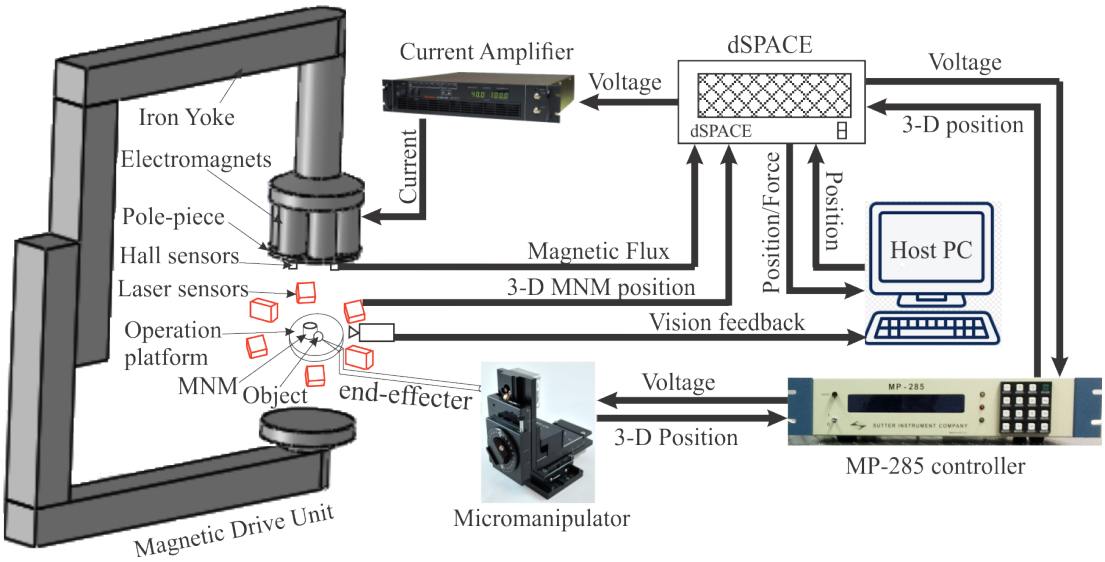

Figure 4.1: Schematic of the two-manipulator cooperative manipulation system

The schematic of the cooperative manipulation system is shown in figure 4.1. The system mainly contains three units: the *executive unit*, the *sensory unit*, and the *control unit*. The *executive unit* in the working envelope consists of an operation platform, the object, the MNM, and the MM. The operation platform is used for supporting small objects which are manually placed on the platform. The MNM is levitated by the magnetic drive unit. An aluminum end-effector collaborates with the MNM to manipulate the small objects. The end–effector is fixed on the motion stage of the micromanipulator. The *sensory unit* contains three pairs of high-resolution laser sensors for measuring the real-time three-dimensional position of the MNM. A digital camera is used to capture the location of the small object. Four Hall-effect sensors are installed at the bottom of the pole-piece of the MDU to measure the magnetic flux passing through the workspace. The *control unit* contains a dSPACE controller, a current amplifier, an MP-285 controller, and

a 3.2GHz host computer. The dSPACE controller acts as a central processing unit to firstly calculate the robots position based on position feedback from the laser sensors, and secondly to output current commands to a current amplifier for driving the electromagnets. The host computer is used for both real-time communication with the controller and for monitoring the operation.

4.3 Cooperative Manipulation Controller Design

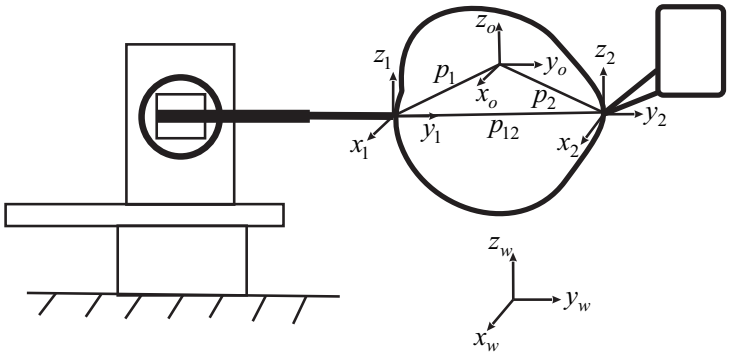

Figure 4.2: Two-micromanipulators cooperative manipulation system. The first micromanipulator is the motorized MP285, the second is the MNM

Suppose that there are n position controlled manipulators rigidly holding an object (figure 4.2). The force on the manipulated object applied by manipulators can be decomposed into internal grasping force F_I and motion inducing force F_m [9]. The internal force does not contribute to the motion of the manipulated object. Mathematically, the applied force can be expressed as:

$$F = F_I + F_m \tag{4.1}$$

For rigid holding, there is no slip induced friction force. Each manipulator applies force and torque on the object. Then the net force at the object coordinate system is:

$$F_o = J_o^T F = [J_{o1}^T J_{o2}^T ... J_{on}^T] F \tag{4.2}$$

where $F_o = [F_{ox} \quad F_{oy} \quad F_{oz} \quad \tau_{ox} \quad \tau_{oy} \quad \tau_{oz}]^T$, $F = [F_{o1}^T \quad F_{o2}^T ... F_{on}^T]^T$.
$F_{oi} = [f_{xi} \quad f_{yi} \quad f_{zi} \quad \tau_{xi} \quad \tau_{yi} \quad \tau_{zi}]^T$ is the force and torque of the ith manipulator on the

object at the contact point, and

$$J_{oi}^T = \begin{bmatrix} I_3 & 0_3 \\ r_{oi} & I_3 \end{bmatrix} \tag{4.3}$$

where r_{oi} is the skew symmetric matrix of vector p_i from the origin of the object frame to the contact point of the ith manipulator, and

$$r_{oi} = \begin{bmatrix} 0 & -p_{zi} & p_{yi} \\ p_{zi} & 0 & -p_{xi} \\ -p_{yi} & p_{xi} & 0 \end{bmatrix} \tag{4.4}$$

Since the internal force does not contribute to the motion of the object, the net internal force is zero. Therefore, by combining equations 4.1 and 4.2, the motion inducing and internal force can be obtained as:

$$F_m = J_o^{\dagger T} J_o^T F \tag{4.5}$$

and

$$F_I = \left(I - J_o^{\dagger T} J_o^T\right) F \tag{4.6}$$

where $J_o^{\dagger T}$ is the generalized inverse of J_o^T.

If two manipulators grasp the object using friction point contact, the manipulator applies only the press force, and no moment on the manipulated object then the Jacobian of the object is:

$$J_o^T = \begin{bmatrix} I_3 & I_3 \\ r_{o1} & r_{o2} \end{bmatrix} \tag{4.7}$$

The rank of the Jacobian matrix is five, which means that the rotation of manipulated object about any axis on the line between two contact points is uncontrollable [10]. In order to guarantee rigid holding we increase the contact area between the end-effectors of both manipulators and the manipulated object. A palm-shaped end-effector with multi-point contact also works for improving the manipulation stability. In this thesis, we used surface type end-effectors and a flat surface object to guarantee rigid holding (figure 4.3).

In this research, the MP285 motorized micromanipulator has three prismatic joints. It applies no torque to the manipulated object. The same apply to the magnetic navigated manipulator. Therefore, the force on the object by all manipulators is $F = [F_{o1}^T \quad F_{o2}^T] = [f_{x1} \quad f_{y1} \quad f_{z1} \quad f_{x2} \quad f_{y2} \quad f_{z2}]^T$. If we could assume that the contact points of the two manipulators on the manipulated object are at the same horizontal and vertical level, then

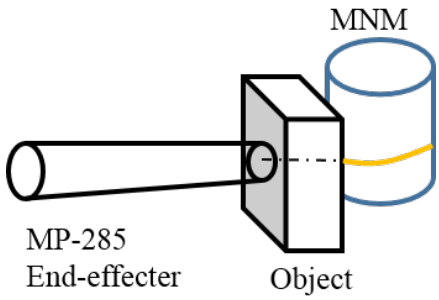

Figure 4.3: Two-micromanipulators holding a cubic object cooperatively. The MP285 has a palm shape end-effector, the MNM has a needle shape end-effector

the net moment caused by force on the object is zero . Based on this assumption, the Jacobian matrix in equation 4.7 can be reduced to:

$$J_o^T = \begin{bmatrix} I_3 & I_3 \end{bmatrix} \tag{4.8}$$

Using MM and the MNM, the manipulated object has three degrees of freedom in translation if the object is not constrained by environment. A proof-of-concept study on the translation of a small square object in the x-direction is studied in this thesis. Both manipulators have uncoupled control over translation in three directions. Therefore, the unique control of manipulation in the x-direction is feasible.

4.4 System Kinematics

Figure 4.4 shows the basic configuration of the cooperative manipulation system. For proof of concept, the two-dimensional configuration of the manipulation system is presented here. The procedure is similar in the third direction. $O_C - x_C z_C$ is defined as the camera coordinate frame whose origin O_C is located at the upper left corner of the image capture plane. The x- and z-axis are in parallel with the horizontal and vertical edge of the image plane. $O_L - x_L z_L$ is defined as the magnetic navigation coordinate frame, whose origin O_L is located at the center of the iron pole-piece bottom, and points in the gravity force direction. Define $O_M - x_M z_M$ as the coordinate frame of the micromanipulator The origin O_M is located at the origin of the motion stage. The x- and z-axis of the three coordinate frames are in parallel, and in the same image-capturing plane.

The relation between the magnetic navigation coordinate $[x_L O_L z_L]$ and the camera coordinate $[x_C O_C z_C]$, and the relation between the MM coordinate $[x_M O_M z_M]$ and the

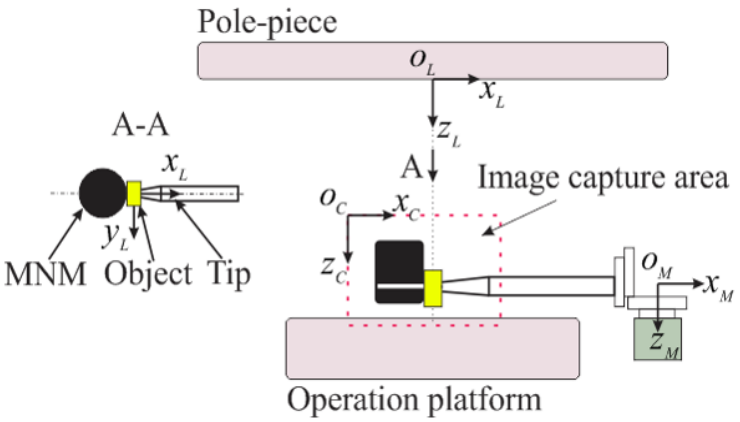

Figure 4.4: Configuration of the cooperative manipulation system

camera coordinate are given as:

$$[x_L z_L] = [x_C + x_{LC} z_C + z_{LC}] \tag{4.9}$$

$$[x_M z_M] = [x_C - x_{MC} z_C - z_{MC}] \tag{4.10}$$

where, $x_C, z_C, x_L, z_L, x_M, z_M$ are the real position of the object, the MNM, and the end-effector of the MM in the camera coordinate frame. x_{LC}, z_{LC} are the distance between the origins of the magnetic navigation coordinate frame and the camera coordinate frame in the x- and the z-directions. x_{MC}, z_{MC} are the distance between the origins of the micromanipulator coordinate frame and the camera coordinate frame in the x- and the z-direction.

4.5 Motion Control of Micromanipulators

In this section, the motion control mechanism of both micromanipulators are introduced. Both micromanipulators in this research are position controlled. First, the dynamic modeling and the position control of the motorized micromanipulator is presented. Secondly, the motion control mechanism of the magnetically navigated microrobot is introduced.

4.5.1 Motorized Micromanipulator

The MP285 motorized micromanipulator is fabricated by Sutter Instrument. The micromanipulator system is composed of a table-box controller and a motorized motion stage. The controller powers the stage and can exchange micromanipulator state information

with a host computer through an RS232 communication port. The motion stage has three degrees of freedom (x, y, and z). In each degree of freedom, the motion range is $25.4mm$, and the accuracy of motion control is $0.2\mu m$. There are mainly two types of input to the controller: pulse mode and analog voltage mode. The pulse mode input is supplied by a hand-held encoder. In this thesis, the analog mode is used. With the analog mode, a feedback controller can be implemented to control the motion of the stage. In the analog voltage input mode, the controller accepts a $0V - 5V$ voltage input. The speed of the stage is proportional to the input voltage and is limited to a maximum of $0.6mm/s$ in all directions. Specifically, when the input voltage is $2.5V$, the speed of the stage is zero. The voltage-speed model is shown in Figure 4.5.

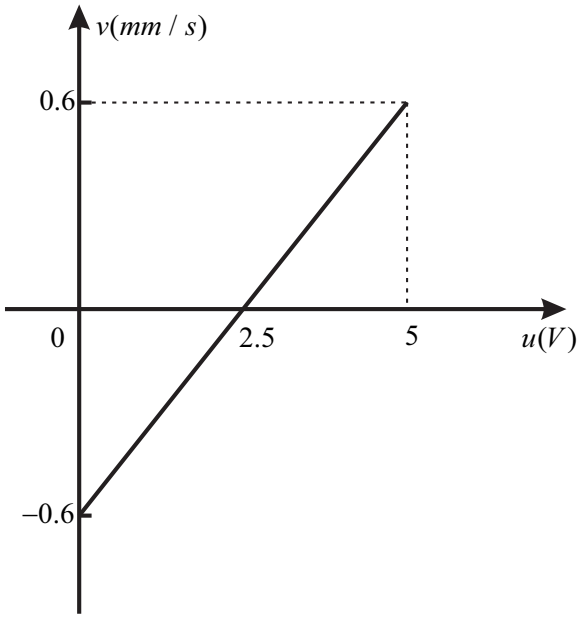

Figure 4.5: Linear relation between voltage input and micromanipulator speed

Therefore, the micromanipulator in each degree of freedom can be simply modeled as:

$$y = \int 0.24(u - 2.5)dt \tag{4.11}$$

where y is the position of the micromanipulator stage in y direction, u is the voltage input to the controller.

The MP285 micromanipulator is position controlled. Standard PID controllers are implemented to control the motion in three directions. The parameters of the PID controller

are $K_p = 85$, $K_I = 10$, and $K_D = 0.1$. The parameters of the PID controller can be tuned using both pole-placement and trial and error methods. The micromanipulator has the same dynamic model in all degrees of freedom, so only one PID controller is designed. It can be implemented to control motion in the other two freedoms. The step response of motion control in the y-direction is studied and plotted in figure 4.6.

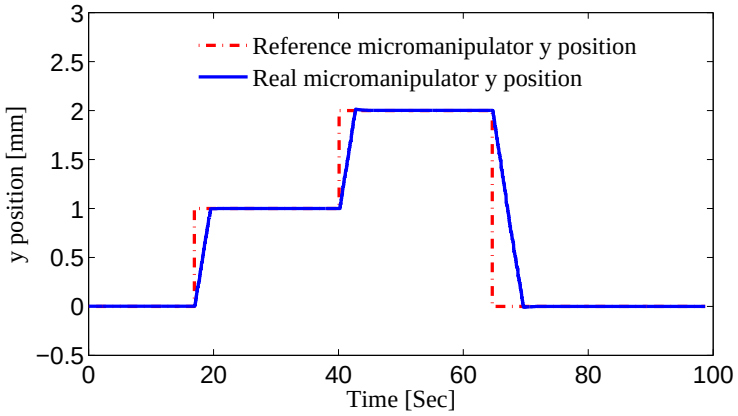

Figure 4.6: Step response of MP285 micromanipulator stage in y direction

The step motion response of the MP285 micromanipulator shows that the system with a PID has fast response performance, $0.8\mu m$ steady state positioning error that is very accurate, and almost zero overshoot. The same PID controller is used in the cooperative manipulation of a small object using the micromanipulator and the magnetic navigated manipulator.

4.5.2 Motion Control of the Magnetically Navigated Microrobot

The dynamics of the magnetically navigated microrobot in contact with environments has been provided in chapter 5. Please refer to equations 5.1-5.3. As presented in chapter 2 and chapter 3, the magnetically navigated microrobot studied in this chapter is position controlled by a PID plus feed-forward controller. The MNM is capable of closely tracking the desired motion trajectory with an accuracy of $10\mu m$ [71]. To track a force trajectory, the desired position command to the MNM's position controller should be obtained from a target impedance controller that relates position error to force tracking error. The same position-based impedance controller is presented in the following section.

4.5.2.1 Position Based Impedance Control

In the majority of the literature, research has been conducted on force based impedance control of manipulators by introducing an outer torque feedback loop at the joint space. This methodology is appropriate for manipulators with torque controlled electrical actuators at joints. However, most commercialized robots emphasize the accuracy of following position trajectory, and do not provide a force control mode. Therefore, force based impedance control was impossible with these manipulators. Alternatively, position-based impedance control is proposed to achieve compliant interaction of position controlled manipulators [62][41]. It is a position controller with set points regulated by a force feedback loop. The position-based impedance control is simple in that no robot dynamics are required. It only requires the controlled manipulator to have an accurate position tracking capability.

It is assumed that the microrobot closely tracks the desired position trajectory. To track a force trajectory, the desired position command to the manipulators position controller should be obtained from a target impedance controller that relates position error to force tracking error.

The generalized target impedance controller is [15][105]:

$$M(\ddot{y} - \ddot{y_r}) + B(\dot{y} - \dot{y_r}) + K(y - y_r) = K_f(F - F_r) \tag{4.12}$$

where M, B, K, and K_f are target impedance parameters. y, and y_r represent the actual and reference position of the MNM in the y direction. F and F_r are defined as the actual and reference contact force. The desired position trajectory is available by solving the target impedance model 4.12. If all the parameters M, B, K, K_f of the impedance model 4.12 are well defined, the impedance control objective can be achieved if the real position of the MNM closely tracks the desired position x_d which is determined by the following expression:

$$M(\ddot{y_d} - \ddot{y_r}) + B(\dot{y_d} - \dot{y_r}) + K(y_d - y_r) = K_f(F - F_r) \tag{4.13}$$

In free levitation state, the desired contact force $F_r = 0$, the impedance holds for $y_d = y_r$, then the impedance is a position controller. However, the desired position y_d has to be calculated from dynamic model 4.13 in contact condition. Using a Laplace transfer function, the desired trajectory is calculated as shown in equation 4.14. It is clear that the free levitation state is a special situation of the contact model.

$$y_d(s) = \frac{K_f(F - F_r)}{Ms^2 + Bs + K} + y_r(s) \tag{4.14}$$

4.5.2.2 Steady state error analysis

The stability of the closed-loop system when the MNM is in contact with its environment depends on the dynamics of the environment and the parameters of the MNM's impedance. The dynamics of environment in the task space can be modeled using a second order linear equation:

$$M_e\ddot{y} + B_e\dot{y} + K_e(y - y_e) = F \tag{4.15}$$

where y_e is the equilibrium position of the environment in the situation of zero contact force. M_e, B_e, K_r represent the inertial, damping, and stiffness of the environment respectively.

Substituting equation 4.15 into equation 4.13, the closed-loop dynamic of the impedance control during contact manipulation is expressed as:

$$(M - K_f M_e)\ddot{y} + (B - K_f B_e)\dot{y} + (K - K_f K_e)y = M\ddot{y_r} + B\dot{y_r} + Ky_r - K_f(F_r + K_e y_e) \tag{4.16}$$

The system is asymptotically stable if M, B, K, and $-K_f$ are chosen as positive.

In steady state, the acceleration and speed of the MNM are zero, i.e., $\ddot{y} = 0, \dot{y} = 0$. The closed-loop impedance 4.16 becomes:

$$(K - K_f K_e)y = Ky_r - K_f(F_r + K_e y_e) \tag{4.17}$$

According to equation 4.17 and the environment dynamic model 4.15, the steady state position error and force error of the impedance is:

$$e_p = (K - K_f K_e)^{-1}[K_f K_e(y_r - y_e) - K_f F_r] \tag{4.18}$$

$$e_f = K_f^{-1}K(K - K_f K_e)^{-1}[K_f K_e(y_r - y_e) - K_f F_r] = K_f^{-1}Ke_p \tag{4.19}$$

From the steady state position and force error model, it shows that the performance of impedance control depends on the stiffness of the environment and parameters of the impedance model. A comprised performance between position and force can be achieved by tuning the stiffness parameters K and K_f.

Suppose that the environment that the MNM in contact with is soft, i.e., the stiffness K_e is small. If the stiffness of the desired impedance holds for $K \gg K_f$, then the impedance emphasis is on position control. However, the force control is emphasized if the environmental stiffness K_f is relatively large (i.e., hard contact) and the impedance stiffness $K \ll K_f$.

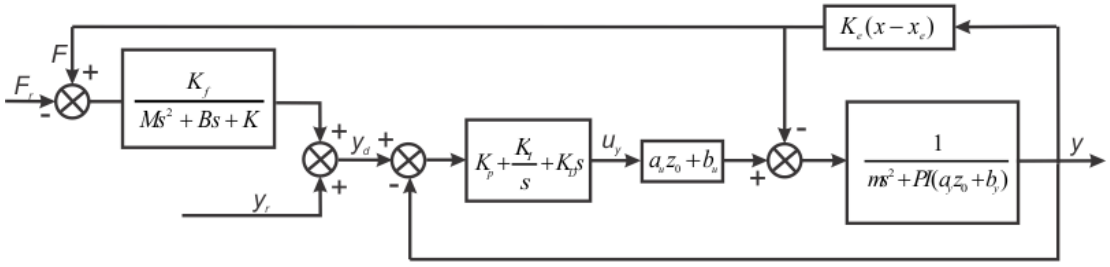

Figure 4.7: Impedance control mechanism with a PID controller

4.5.2.3 Impedance controller performance validation on the MNM

The overall position based impedance control schematic for the MNM is shown in figure 4.7

Validation experiments were conducted to show the effect of impedance parameters on the accuracy of position and force trajectory tracking in the y direction of the coordinate system defined in figure 2.5. In these experiments, the MNM is levitated at $z = 78mm$ below the pole-piece and is in contact with a cantilever beam that has a stiffness factor of $K_e = 0.106$. Three experiments are conducted: 1) $K = 0.106, K_f = 20$, the MNM is commanded to track a step force trajectory. The results shows that the impedance enhances force tracking with an error of $2\mu N$ between desired and real contact force. The position error changes under different force trajectories (figure 4.8); 2) $K = 0.106, K_f = 20$, the MNM is commanded to track a step position trajectory. The same as the first experiment, the impedance enhances force tracking with an error of $5\mu N$ between desired and real contact force (figure 4.9); 3) $K = 10, K_f = 1$, the MNM is commanded to track a step position trajectory. Different from previous experiments, the impedance enhances positioning tracking with error of $5\mu m$ between desired and real MNM position. The force error changes with respect to different location of the MM (figure 4.10).

From the experimental results, it is concluded that a compromised performance of positioning and force tracking is achievable by carefully tuning the stiffness factors K and K_f. However, if the environmental stiffness factor K_f is infinite, the impedance is only capable of maintaining force tracking. But a K that is less than K_e results in sustained oscillation, even though the system is over damped. During the experiments, parameters M and B are tuned to study their effect on the impedance control. Based on observation, increasing M slows the system response, decreasing B results in oscillation. The value of M and B used in experiments are $M = 0.01$ and $B = 0.5$. It is also noted that there is significant over shoot on force trajectory while the system is following a position trajectory (figure 4.9). Future work could be smoothing the over shoot to better protect the MNM

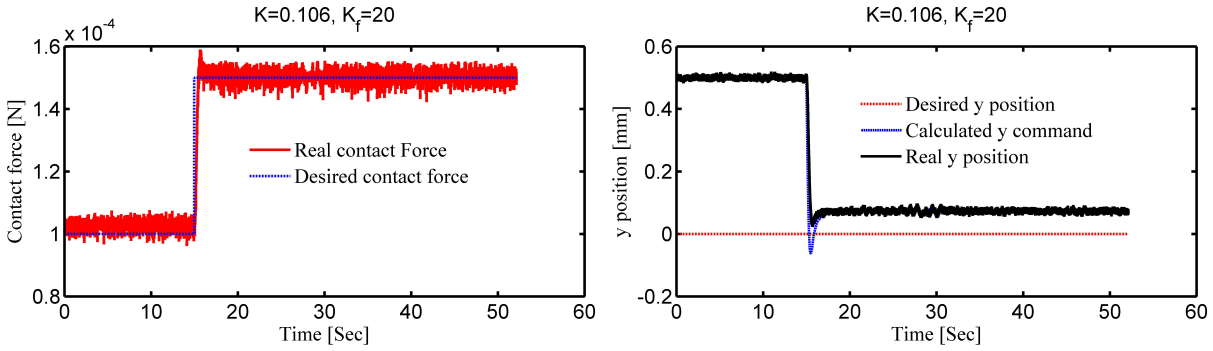

(a) (b)

Figure 4.8: Force trajectory tracking while $K = 0.106$ and $K_f = 20$: (a) force tracking, (b) positioning tracking

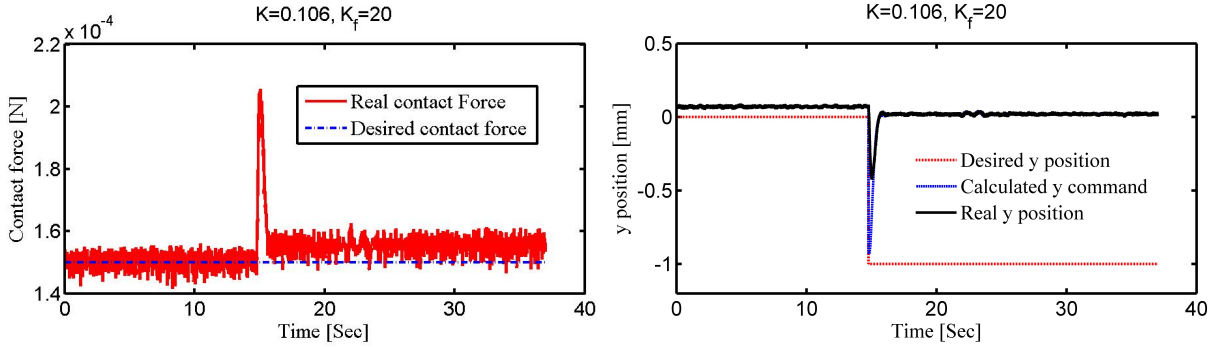

(a) (b)

Figure 4.9: Position trajectory tracking while $K = 0.106$ and $K_f = 20$: (a) force tracking, (b) positioning tracking

and manipulated object.

During the cooperative manipulation, the manipulated object is rigidly held by the two micromanipulators. Therefore, the reference trajectory of the MNM can be calculated from the real time position of the tip. According to the definition of the coordinate system shown in figure 4.4, the reference trajectory of the MNM in the levitation coordinate system is

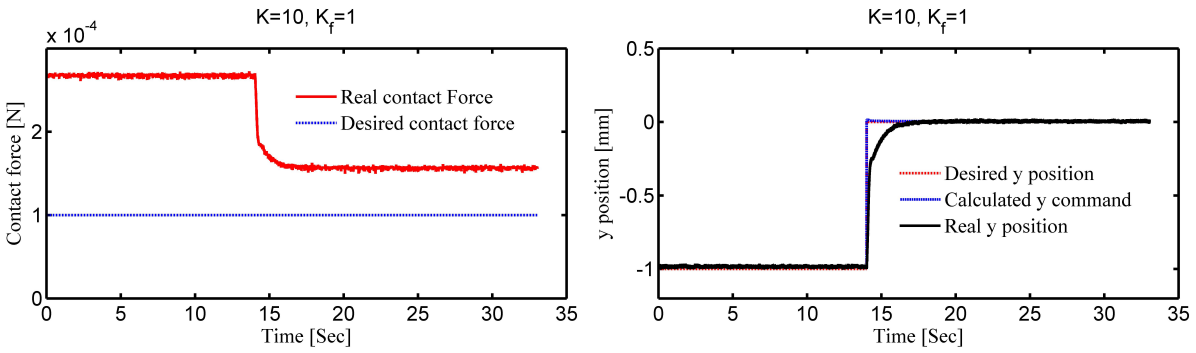

Figure 4.10: Position trajectory tracking while $K = 10$ and $K_f = 1$: (a) force tracking, (b) positioning tracking

expressed as:

$$\begin{bmatrix} x_r \\ \dot{x}_r \\ \ddot{x}_r \end{bmatrix} = \begin{bmatrix} x_M - R - R_m + x_{LC} - x_{MC} \\ \dot{x}_M \\ \ddot{x}_M \end{bmatrix} \tag{4.20}$$

where $x_M, \dot{x}_M, \ddot{x}_M$ are the real-time position, speed, and acceleration of the MM's end-effector in the x-direction, R is the thickness of the manipulated sphere object, and R_m is the radius of the MNM. The reference speed and acceleration for the impedance controller are the same as the speed and the acceleration of the MM's end-effector. The position-based impedance controller for the MNM is shown in figure 4.11. The feed-forward part of the controller calculates the current I_0 shown in the MNM's dynamic model in equations 5.1-5.3.

The cooperative manipulation in this chapter is conducted in the x-direction of the coordinate system shown in figure 2.5. Then, the desired position trajectory of the MNM calculated from its target impedance controller is:

$$x_d = x_r + K_d^{-1}[M_d(\ddot{x}_r - \ddot{x}_d) + B_d(\dot{x}_r - \dot{x}_d) - K_f(F - F_r)] \tag{4.21}$$

where, M_d, B_d, K_d, K_f are positive definite inertial, damping stiffness, and force parameters of the target impedance model; x_r and x_d indicate the reference and actual trajectory of the MNM end-effector; F is the actual contact force applied to the environment by the MNM, and F_r is the reference contact force that the MNM tracks. In a free levitation situation, the reference and real contact force are chosen as zero. Then the impedance controller becomes a position controller.

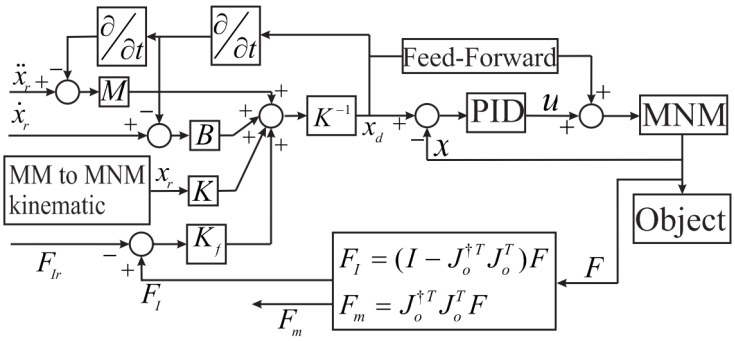

Figure 4.11: Schematic of position-based impedance control for x-direction motion of the MNM

4.6 Cooperative Manipulation Controller Design

4.6.1 Image Processing

Computer-vision-based automotive manipulation has been widely implemented in industrial and bio-engineering processes [3][18][97]. Owing to the limitation of conventional sensors in detecting the position of a micro-object, image-based position determination is popular in micromanipulations such as cell injection [44] and micro-chip fabrication [4]. In cooperative manipulation, a digital camera is commonly installed to capture the position of the object being manipulated. The captured image serves as position/force feedback for precise operation and dynamic control.

In this research, a charge-coupled device (CCD) camera GC2450 manufactured by Allied Vision is used to capture the 2-D position of the manipulated object and the two end-effectors in the workspace. The image processing procedure is as follows: The camera first captures a grayscale image of the area of interest. The obtained image is convolved with a low pass Gaussian filter to reduce the noise, as shown in figure 4.12(a). Then the grayscale image is converted to a binary image for reducing the processing time (figure 4.12(b)). To find the real-time location of the magnetically navigated end-effector, the object, and the micromanipulator end-effector, the correlation-based pattern matching method is implemented. The real time image is used to compare with target images to find the positions of the object and micromanipulators. Figure 4.12(c) and figure 4.12(d) show the image processing results and the target images. Since the dimension of the MNM is very large relative to the dimension of the captured image which is 540 × 340 pixels, tracking the motion of the entire MNM is time consuming. Therefore, we track only part of

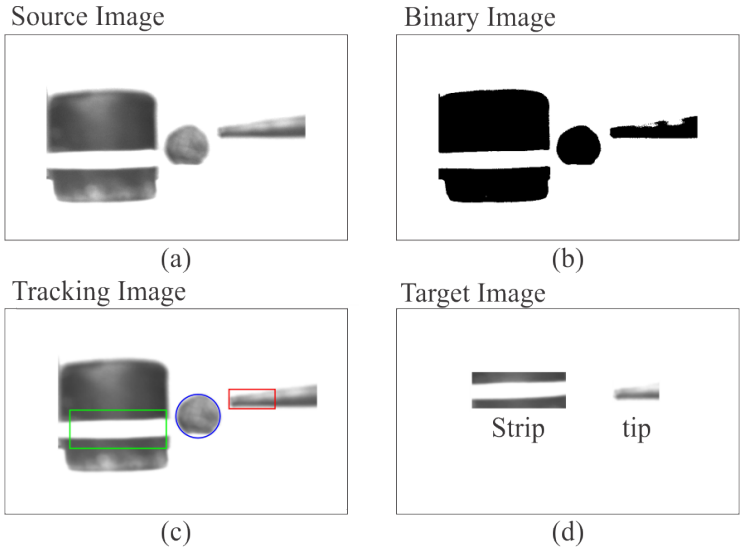

Figure 4.12: Processing of images captured by CCD camera, (a) source image, (b) binary image for detecting object, (c) Manipulators tracking using correlation-based pattern matching, (d) target images of MNM and micromanipulator.

the MNM by wrapping a thin white strip on the lower part of the MNM. The edge position of the strip is the location of the contact point between the MNM and the manipulated object. Similarly, only part of the micromanipulator end-effector is tracked to reduce the computation time for motion tracking.

It should be mentioned that the image processing component of the cooperative manipulation system is aimed to detect the dimensions and location of the object being manipulated, and to guide the two micromanipulators toward the desired pick up location with visual feedback. Once the micromanipulator end-effectors are in contact with the object, the position feedback obtained from the motorized motion stage encoder and laser-beam sensors are used for navigating the two micromanipulators.

4.6.2 Manipulation Process

The manipulation of the small object in this research is conducted in the xoz plane. Before the manipulation, calibration is executed to prevent misalignment of the MNM, the object, and the end-effector of the MM in the y-direction of the coordinate system as shown in figure 2.5. During the manipulation, the object to be manipulated is first manually placed on the operation platform and in the image capture range of a CCD camera. The manipulation procedure is then completed in two separate phases which are defined as

the *approaching phase* and the *translation phase*. In the *approaching phase*, the camera first determines the location of the object and manipulators in the workspace using image processing algorithms. Then the MNM is levitated at a height in the z-direction such that the z-axis position of the bright strip on the MNM is the same as the z-axis position of the object center. The horizontal navigation command x_L of the MNM is determined based on the kinematic relation expressed in equation 4.9. For the end-effector of the MM, its motion command x_M, z_M are generated based on the kinematic relation shown in equation 4.10. The *translation phase* starts when both micromanipulators are in contact with the object. The translation is finished in three steps: *picking up* the object in the z-direction, *transporting* the object in the x-direction, and *releasing* the object in the z-direction at the desired location. During the translation, the reference motion trajectory in both x- and z- directions are commanded to the motion controller of the MM. To guarantee the success of the translation and to protect the object from being damaged, navigation of the MNM in the x-direction is switched to force control mode, while in the z-direction, position control mode is maintained. A desired holding force in the x-direction is pre-set, and is sent to the force controller of the MNM as the reference holding force.

4.6.3 Control Strategy

In this study, a simple master/slave control mechanism is incorporated to complete cooperative manipulation tasks. The master manipulator is the MM. Its motion trajectory is predefined according to the manipulation strategy. The slave manipulator is the MNM. No motion command is assigned directly to the slave manipulator in the x-direction. The motion trajectory of the MNM is calculated from a position based impedance controller. The impedance controller maintains a desired holding force on the manipulated object based on the measured contact force at the end-effector of the MNM.

4.6.3.1 Motion control

Both the MNM and the MM are position controlled in the three directions of the Cartesian coordinate space. Force/torque control modes are not available at the joint space of each manipulator. PID controllers are implemented to control the motion of both manipulators with high accuracy in three-degrees-of-freedom.

In the approaching phase, the end-effectors of the two micromanipulators are navigated in the x-z plane. The reference position of the micromanipulators are obtained based on the real position of the object and are calculated using the kinematic relation expressed in equation 4.22-4.23. In the levitation coordinate system,

$$\begin{bmatrix} x_{Lr} \\ z_{Lr} \end{bmatrix} = \begin{bmatrix} x_C - R - R_m + x_{LC} \\ z_C + z_{LC} \end{bmatrix} \tag{4.22}$$

In the micromanipulator coordinate system:

$$\begin{bmatrix} x_{Mr} \\ z_{Mr} \end{bmatrix} = \begin{bmatrix} x_C + R + x_{MC} \\ z_C + z_{MC} \end{bmatrix} \tag{4.23}$$

where R is the thickness of the manipulated object. x_L, z_L are the reference positioning command to the MNM in the x- and z- directions; x_{Mr}, z_{Mr} are the reference positioning command to the motorized micromanipulator in the x- and z- directions.

In the *translation phase*, it is assumed that the manipulators hold the object tightly. No slip motion occurs during the manipulation. When a hard-shell object is translated, it is also acceptable to neglect the change of its output profile. Therefore, the motion trajectory of the object can be mapped into the trajectory of the master micromanipulator's end-effector motion trajectory. For the MNM on the slave side, a position-based impedance controller is implemented to calculate the reference motion trajectory of the PID controller in the x-direction, while in the z-direction, a position command is directly given to the PID controller. The control schematic of the manipulation process is shown in figure 4.13

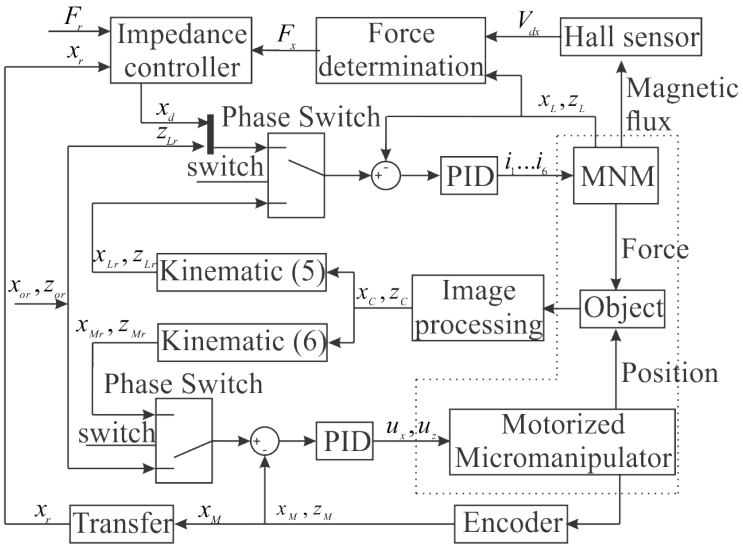

Figure 4.13: Controller schematic for cooperative manipulation. x_{Or} and z_{Or} are the reference trajectory of the object in the translation phase.

4.6.3.2 Off-board force determination with moving environment

The force determination method presented in chapter 3 is valid if and only if the MNM is in contact with a stable environment, which means that there is only one initial contact

point. However, in the cooperative manipulation in this research, the manipulated object is translated in the workspace. This indicates that the location of the contact point between the MNM and its environment (the object) is moving. Then the force model in equations 3.11 and 3.12 is not valid in the cooperative manipulation. The parameters of the magnetic flux modeling are not repeatable at different initial contact points. This is explained in figure 4.14.

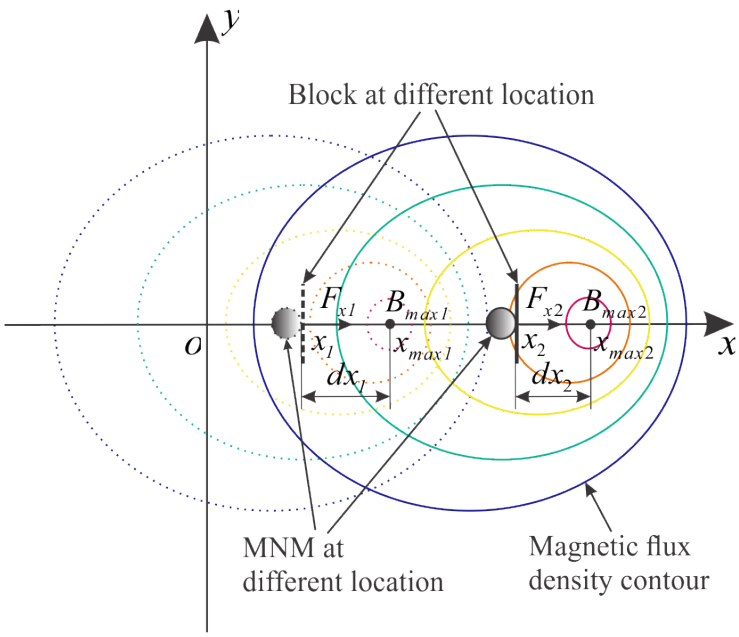

Figure 4.14: Mechanism of magnetic force produced at different initial contact points

Based on the experimental measurement results shown in figure 4.15(a)-(c), while the location of the environment is changing, the off-board force using Hall-effect sensors output in the x-z plane is modeled as:

$$F_x = (az^2 + bz + c)V_{dx} + (dz^2 + ez + f)x + g \tag{4.24}$$

where F_x is the off-board force in the x-direction, a, b, c, d, e, f, g are constant coefficients determined from experimental measurements. x and z are the real time position of the MNM in the x- and z- axis of the coordinate system defined in figure 2.5. V_{dx} is the output of the Hall-effect sensors, which represents the magnetic flux measurement. In order to obtain the best coefficients, the minimum mean square error method was used in curve fitting.

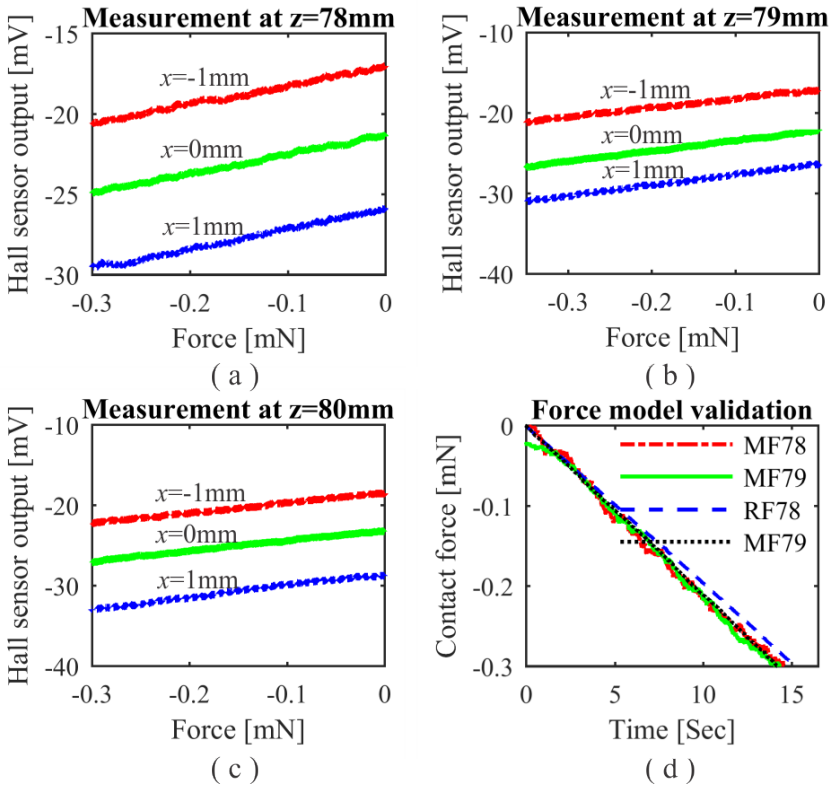

Figure 4.15: Measured force using an Aluminum cantilever beam versus Hall-effect sensors output at different contact point location in x-direction on different planes: (a) Measurement at $z = 78mm$ below the iron pole-piece; (b) Measurement at $z = 79mm$ below the iron pole-piece; (c) Measurement at $z = 80mm$ below the iron pole-piece; (d)Force model validation at $x = 2mm$ on different planes. MF78 represents magnetic force at $z = 78mm$. RF78 represents real force at $z = 78mm$

The accuracy of the force model shown in equation 4.24 was experimentally validated by comparing the real contact force and the magnetic flux measurement-based magnetic force. In the experiment, the real contact force between the MNM and an aluminum cantilever beam was measured by detecting the deflection of the cantilever beam using a high-accuracy laser beam sensor. As presented in figure 4.15(d), the magnetic flux measurement-based force determination mechanism provides good accuracy with a maximum error of 0.02mN. The accuracy of the off-board force determination can be improved by using high resolution Hall-effect sensors and the high-order cantilever beam deflection model.

4.7 Experimental Validation

Experiments were conducted to show the performance of the proposed cooperative micromanipulation system. The experiment setup is shown in figure 4.16. As mentioned above, for proof of concept, the translation of small objects was conducted in two directions in the x-z plane. For simplicity, the translation speed was set as constant $0.5mm/s$ during the cooperative manipulation. The MNM in this research is an N42 permanent magnet with $1.29T$ remnant magnetic flux density. The dimensions of the MNM are $10mm$ diameter and $10mm$ height. The diameter of the MM's end-effector is 1mm. The manipulation was conducted at y=0 plane in the magnetic levitation coordinate system. The area of the captured image in the workspace is $30mm \times 18mm$. Two objects with different stiffnesses were manipulated.

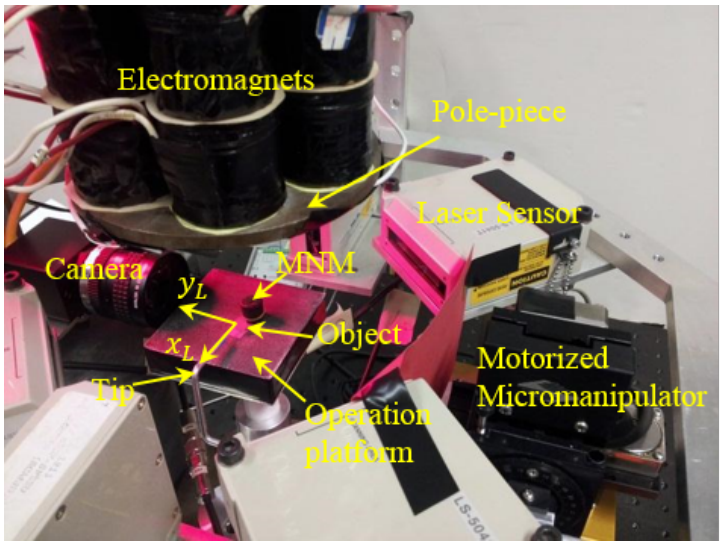

Figure 4.16: Experiment setup for cooperative micromanipulation

4.7.1 Translation of a Hard-shell Object

The first experiment aims to translate a hard-shell object from its initial position to a desired location. The manipulation was conducted in the x-z plane of the MNM coordinate system. The manipulation procedure presented in figure 4.17 includes (a) detecting the position of the MNM, the MM, and the object (marked with a rectangular shape color marker, using a CCD camera), (b) navigating the two manipulators towards the object using the camera position feedback, and holding the object with predefined grasping force,

(c) picking up the object from the operation platform (the lifting height is 2mm in z-direction), (d) translating the object in the x-direction for 2mm distance, (e) placing the object down on the operation platform, and (f) releasing the object.

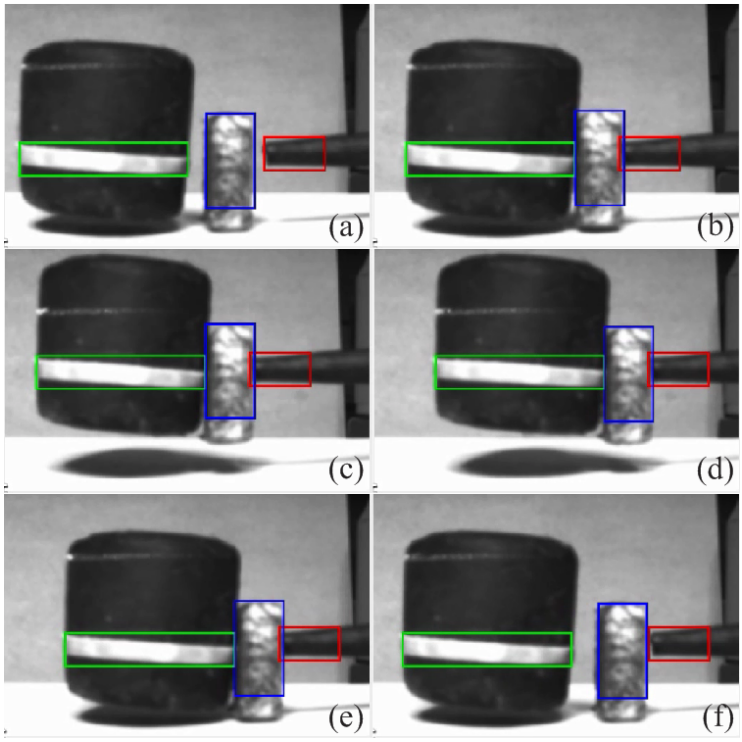

Figure 4.17: Cooperative translation of a small object in the x-z plane with position and force control. The green rectangle marks part of the MNM. The blue rectangle marks part of the object. The red rectangle marks part of the MM end-effector

The object being translated is a small box-shaped foam with dimensions of $8mm \times 6mm \times 3mm$. Its weight is $0.045g$. It should be noted that the MNM was first levitated and positioned to make sure the center of the MNM in the y-direction is lined up with the object and the MM's end-effector The parameters of the position-based impedance controller gains were $M = 1Ns^2/m$, $B = 20Ns/m$, $K_f = 40$. Different stiffnesses K of the impedance controller were selected at different stages of the manipulation task, and can be understood using the following analysis. Assume that the stiffness of the environment that the MNM in contact with is K_e. Using the environment stiffness, the real contact force is expressed as:

$$F = K_e(x - x_e) \tag{4.25}$$

where x is the real position of the MNM, x_e is the non-contact state position of the environment, and $x - x_e$ indicates the environment deflection under the pushing force by the MNM.

Combining the desired impedance model in equation 4.13 and 4.25, we obtain the steady state position and force error of the impedance controller:

$$e_P = (K - K_f K_e)^{-1}[K_f K_e(x_r - x_e) - K_f F_r \tag{4.26}$$

$$e_f = K_f^{-1} K e_p \tag{4.27}$$

where e_P is the position error in navigating the MNM, and e_f is the force error of the impedance control. Equation 4.27 indicates that by choosing different force parameter K_f and stiffness K, the impedance controller emphasizes position and force control.

In this experiment, the impedance controller was firstly setup to emphasize position control to guarantee a tight holding of the object. The impedance stiffness $K = 100N/m$ was used for motion tracking. Then it was switched to $K = 1.2N/m$ to emphasize force tracking. The experimental results are presented in figure 4.19 and figure 4.18. Figure 4.19 shows the motion trajectory of the MNM, the MM's end-effector, and the object in the manipulation process. The position data was collected after the manipulators approached the object. Figure 4.19a is the motion trajectory of the MNM. From 0sec to 19sec, the MNM was in free levitation state. After 19 seconds, the position-based impedance controller was activated. From 19 sec to 33 sec, the impedance controller emphasized position control to guarantee that the MNM is grasping the object. After 33 sec, the impedance controller was switched to emphasize force control. A $0.1mN$ reference force was assigned for initial force control. Once the system was stable, a $0.4mN$ reference holding force was assigned at 55sec as shown in figure 4.18. When the operation time came to 105 sec, the object was lifted up $2mm$ in the z-direction from the operation platform as shown in figure 4.19. As soon as the whole system came to a steady state at 133sec, the object was translated 2mm in the x-direction. Then the object was placed on the platform at 185sec. In order to release the object, the holding force was set to $0.1mN$ at 210 sec. Finally, the impedance controller was deactivated to release the object at 225sec as shown in figure 4.18.

4.7.2 Cooperative Manipulation of Soft Object: A Demo Experiment For Microinjection

The proposed cooperative micromanipulation system has potential application in the field of microinjection as the size of the magnetically navigated microrobotics downscaled to

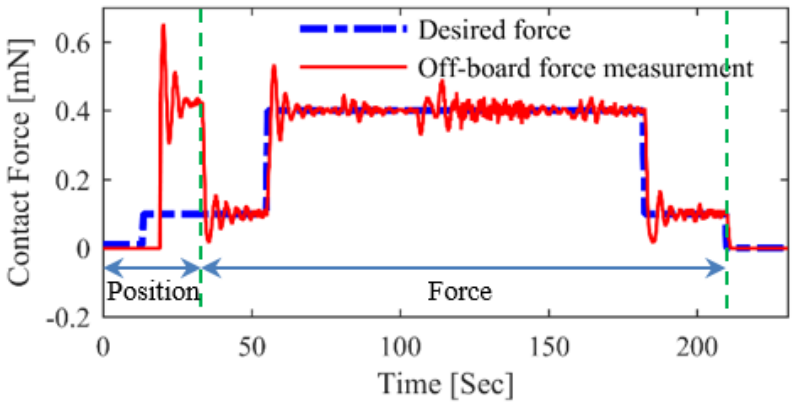

Figure 4.18: Reference holding force on the object and the real holding force obtained using off-board force determination mechanism

micrometers. Conventionally, a microinjection system includes a cell holding equipment and an injector. A microscope with a digital camera is used to detect the micro-injector and the cell. The contact force between the injector and the micro object is determined using the changing of the cell shape. This type of system is complex in the sense of developing the holding equipment and measuring the force.

For the proposed cooperative micromanipulation system to be used in microinjection in the future, the MNM can be used as the holding equipment, while the motorized micromanipulator can be used as the holder of the injector. In addition, the magnetic-flux-measurement-based off-board force determination mechanism reduces the effort of force measurement using a microscope. A demo experiment showing the concept of microinjection using the proposed system was conducted in this section.

In this experiment, a soft object that mimics a bio cell was pushed by the MNM and a glass needle. The glass needle functioned as the injector and was held by the motorized micromanipulator. Figure 4.20 shows the experimental setup and real time pictures of the microinjection process. Before the microinjection, the needle first approached the cell with the assistance of the motorized micromanipulator. Then a haptic device was used to command the MNM to push the cell for needle insertion. There is an impedance controller implemented to the haptic. The off-board force was fed back to the haptic device so the operator could feel the real time pushing force. During the injection, the glass needle stayed at the same place throughout the process.

Figure 4.21 shows the results of force measurement and the MNM position detection in the injection demo experiment. Two continuous attempts were recorded. A maximum

of 0.25mN was recorded in this process.

4.8 Discussion

The pushing force plot in figure 4.18 shows lots of oscillation during the manipulation. There are two reasons for this. First, the position-based impedance controller parameters are not well tuned for this application. Second, at each manipulation step, there is a new position command to the controller, but the slow response of the controller takes time to be stabilized. Therefore, an adaptive force tracking of the MNM is presented in Chapter 5 to smooth the force tracking.

Although the cooperative manipulation of small objects is achieved in this thesis, if we want to apply the system to more general applications, there is much work left to be done. For example, the current system setup is capable of manipulation in a 2D vertical plane. However, the object shape is limited to regular blocks. The end-effectors is also required to have surface contact with the manipulated object. In addition, the rotation of the object along its vertical central axis is not controllable, which means the manipulators' end-effector and object has to be lined up precisely before the manipulation. Therefore, in future work, a top camera should be installed to let the system has object orientation detection, such that the trajectories of both manipulators can be adjusted correspondingly.

As mentioned in the demo experiment section, the proposed system has potential application in biomedical engineering. Since the current size of the MNM and MM end-effectors are very large compare with micro scale objects, the system cannot be applied to micromanipulation tasks with the current setup. As part of future work, a micro scale MNM should be designed and controlled with sub-micrometer accuracy to validate the performance in biomedical applications.

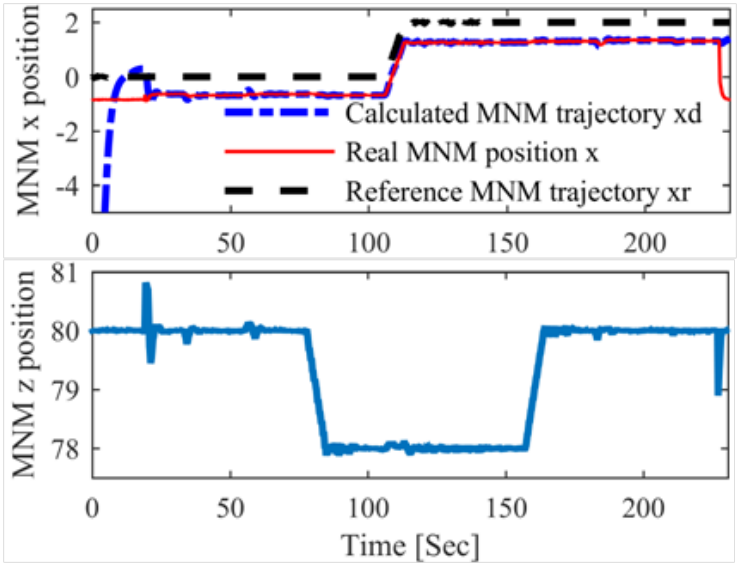

(a)

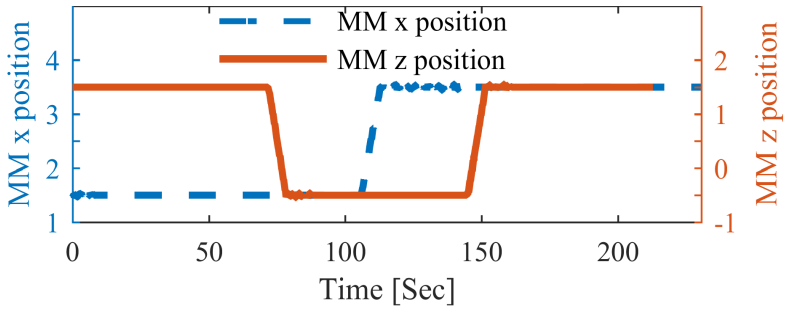

(b)

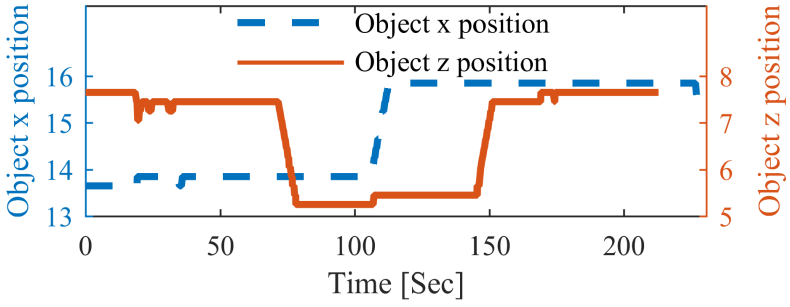

(c)

Figure 4.19: Motion trajectory of the MNM, the MM end-effecter, and the object in the x-direction and z-direction in their corresponding coordinate system. Position unit is millimeters.

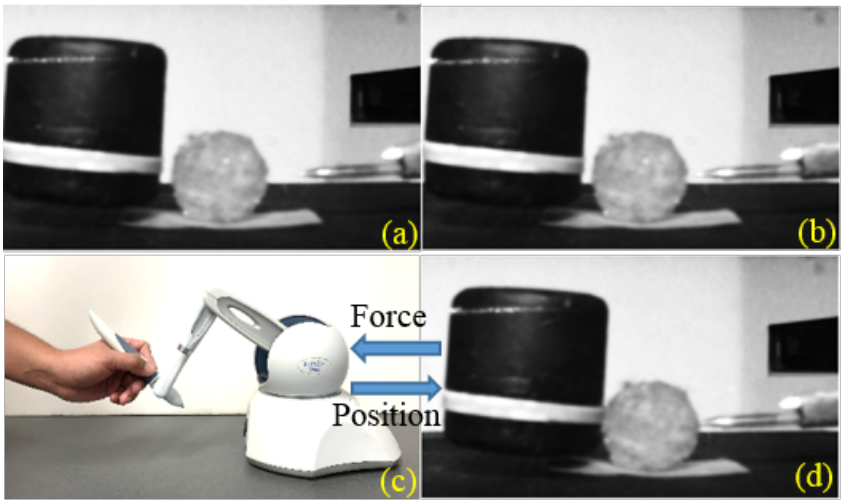

Figure 4.20: Pictures for cell manipulation demo: (a) experiment setup that is ready for micromanipulation; (b) the motorized micromanipulator was navigated towards the soft object; (c) a haptic device was used to generate motion command for the MNM; (d) the MNM was commanded to push the object for injection, contact force was measured and was feedback to the haptic device.

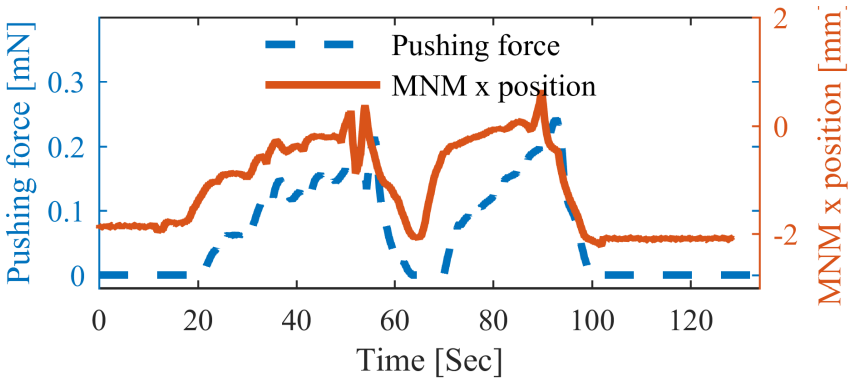

Figure 4.21: Demo experiment results

Chapter 5

Compliant Motion Control of a Magnetically Navigated Microrobot in Contact with Uncertain Environments

5.1 Introduction

Force control is important to robust and dexterous manipulation when a manipulator works in a constrained environment. Manipulators with force control capability have been implemented for macro and micro manipulation tasks, such as surgical assistance [109], painting [58], peg-in-hole operations [64], cell injection [103], and microsurgery [47]. With force control the simultaneous protection of the manipulator and its environment is achieved.

Many researchers have studied force control of manipulators by implementing various controller algorithms. Generally, these algorithms are categorized into hybrid position/-force control [12][26] and impedance control [42]. Within the impedance control framework, a desired second order model is assigned to a manipulator. The desired model enforces a relation between the position error dynamic and the force tracking error. A steady-state zero force error is obtainable if the reference position trajectory of the impedance controller is well designed. Generally, the reference position trajectory can be designed based on known environmental parameters, i.e., the non-touch state position and the stiffness of the environment. However, in real applications, the environment is not known or only partially known. Therefore, a perfect reference position trajectory is not always obtainable,

leading to steady-state force tracking errors. Numerous attempts to deal with environmental uncertainty in force tracking have been reported in the literature [52][66][45]. In [53], an adaptive impedance controller was proposed to solve the force tracking problem when a manipulator is in contact with an unknown environment. Zero manipulator stiffness was used to realize the steady-state zero force tracking error, while the adaptive law utilized the force tracking error to update the impedance parameter of the desired impedance model. Seraji [89] proposed direct and indirect adaptive impedance controllers for force tracking in an uncertain environment. For the direct controller, a model reference adaptive control law was applied to update the reference trajectory of the impedance controller. For the indirect controller, the reference motion trajectory was calculated after estimating the environment stiffness and position, both updated based on force tracking error. Advanced control methods, such as neural networks, were also applied to improve the force tracking performance of manipulators in an uncertain environment [100], but this type of controller requires a huge amount of training data, which is not always easy to collect. The research in the literature was conducted only on manipulators that had a mechanical joint. The adaptive force tracking issue has not been studied for magnetically navigated manipulators.

Magnetically navigated microrobotics is an emerging technique that uses magnetic energy to remotely guide a microrobot. Thanks to its dust-free and non contact manipulation features, the magnetically navigated microrobot has a promising potential in biomedical applications, such as invasive microsurgery and drug delivery. Several magnetic navigation prototypes have been developed for future implementation in biomedical applications [54][27][59][67][36]. However, the published research concentrates merely on the precise positioning of magnetically navigated microrobots. The contact force on the microrobot was not considered, which would result in failure of levitation or damage to the structures that the microrobot works with.

In this chapter, a position-based impedance control mechanism is implemented to achieve the active tracking of a reference force when a magnetically navigated microrobot is in contact with its environment. Since the active force regulation requires force feedback from a force sensor, the dual-axial off-board force determination method presented in chapter 3 is implemented to overcome the common limitation of installing a force sensor on a tiny levitated microrobot [71]. In addition, the force tracking problem is solved by adopting an adaptive law that ensures asymptotic stability. The reference position trajectory is calculated from the estimated stiffness and the position of the contact surface. The experimental results are presented to show the adaptive force tracking performance of the levitated microrobot. The technique proposed has great potential for application in biomedical microsurgery.

In order to have a better understanding of the research in this chapter, please refer to

chapter 2 for the magnetic levitation system description, and find the principle of magnetic levitation.

5.2 Dynamics of the Magnetically Navigated Microrobot in Contact with Environments

Based on the magnetic levitation system dynamic modeling presented in chapter 2 and our previous study in [71], the dynamics of a magnetically navigated object in three dimensional directions are expressed as:

$$\begin{aligned} m\ddot{x} =& 3xI_0\left(a_x + a_y\right) \\ &+ b_x\left(i_1 - i_3 + i_4 - i_6\right) + F_{ex} \end{aligned} \tag{5.1}$$

$$\begin{aligned} m\ddot{y} =& 3yI_0\left(a_x + a_y\right)\left(a_{yz}z_0 + b_{yz}\right) \\ &+ b_y\left(i_1 + 2i_2 + i_3 - i_4 - 2i_5 - i_6\right) + F_{ey} \end{aligned} \tag{5.2}$$

$$m\ddot{z} = a_z I_0 z + \left(a_z z_0 + b_z\right)\left(i_i + i_2 + i_3 + i_4 + i_5 + i_6\right) + F_{ez} \tag{5.3}$$

where m is the mass of the microrobot, and x, y and z are real three dimensional positions of the microrobot in the workspace. I_0 is the current in all electromagnets while the microrobot is levitated at the center of the workspace. The parameters $a_x, a_y, a_z, b_x, b_y, b_z$ are evaluated from experimental measurements. While $i_j (j = 1, ...6)$ are the perturbed current of the j^{th} electromagnet shown in Fig. 1. F_{ex}, F_{ey}, F_{ez} are the three-dimensional contact forces exerted by the environment. Since designing a controller that has six outputs is much more complex than a controller with only three outputs, three virtual inputs u_x, u_y, u_z are assigned for three dimensional translational motion control of a feed-forward plus a proportional-integral-derivative (PID) controller. The feed-forward controller provides the fundamental levitation current, while the PID controller regulates the perturbation caused by disturbance. The transformation from three virtual inputs to six current inputs using pseudo-inverse guarantees the least energy consumption. The position controller schematic is shown in figure 5.1. The motion controller provides $10\mu m$ positioning accuracy.

5.3 Adaptive Force Tracking Control of the MNM in Uncertain Environment

The generalized target impedance controller is rewritten as:

$$M(\ddot{Y}_r - \ddot{Y}_d) + B(\dot{Y}_r - \dot{Y}_d) + K(Y_r - y_d) = K_f(F - F_r) \tag{5.4}$$

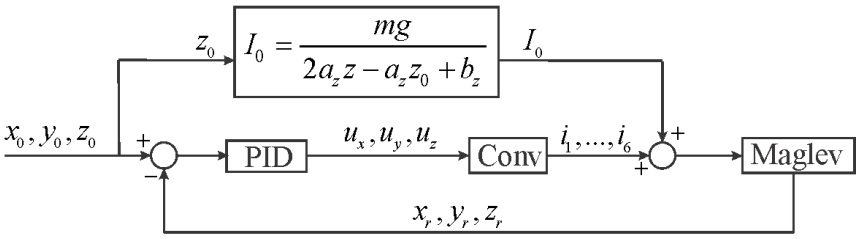

Figure 5.1: PID plus feed-forward motion tracking controller for the magnetic navigation system

where M, B, K, and K_f are target impedance parameters. Y_r and Y_d represent the reference and actual position of the MNM. F and F_r are defined as the actual and reference contact force. The desired position trajectory is available by solving the target impedance model 4.12:

$$Y_d = Y_r + K_d^{-1}[M(\ddot{Y}_r - \ddot{Y}_d) + B(\dot{Y}_r - \dot{Y}_d) - K_f(F - F_r)] \tag{5.5}$$

In real applications, the actual force can be obtained from the parameters of the environment:

$$F = K_e(Y - Y_e) \tag{5.6}$$

where K_e and Y_e are respectively the stiffness and original location of the environment, Y is the actual position of the microrobot, and $Y = Y_d$ if the microrobot has accurate position tracking capability. Let $E_f = F_r - F$ denote the force tracking error. The actual microrobot position can be expressed as:

$$Y = Y_e + K_e^{-1}F = Y_e + K_e^{-1}(F_r - E_f) \tag{5.7}$$

Substituting equation 5.7 into equation 5.4 resulting in obtaining the following steady-state force tracking error expression:

$$E_f = (K_d K_e^{-1} + K_f)^{-1}[K_d K_e^{-1} F_r + K_d(Y_e - Y_r)] \tag{5.8}$$

From equation 5.8, in order to closely track the reference force trajectory, the reference position trajectory should be selected as:

$$Y_r = Y_e + K_e^{-1}F_r \tag{5.9}$$

However, in reality the values K_e and Y_e of the environment are not always known precisely. Therefore, an adaptive law is presented in the following to compensate for parameter uncertainty.

Let $x_r, x_d, x_e, k_e, k, f_r, f$ be the elements of $Y_r, Y_d, Y_e, K_e, F_r, F$. Here, only one dimensional situation is considered. The multi-dimensional force tracking can be achieved in the same way.

Let $\hat{k}_e$ and $\hat{x}_e$ be the estimation of k_e and x_e respectively. Replacing with the estimated value in equation 5.7 and 5.9, one gets:

$$x = \hat{x}_e + \frac{f}{\hat{k}_e} = \hat{x}_e + \frac{1}{\hat{k}_e}(fr - e_f) \tag{5.10}$$

$$x_r = \hat{x}_e + \frac{f_r}{\hat{k}_e} \tag{5.11}$$

Then the error between reference input and actual position is:

$$x_r - x = \frac{e_f}{\hat{k}_e} \tag{5.12}$$

Substituting the error expression into the impedance dynamic model 5.4, the force tracking error dynamic model is obtained as:

$$m_d\ddot{e}_f + b_d\dot{e}_f + (k_d + \hat{k}_e k_f)e_f = 0 \tag{5.13}$$

where m_d, b_d, k_d, k_f are elements of M_d, B_d, K_d, K_f. It shows that equation 5.13 is asymptotically stable if all its parameters are positive definite. The force tracking error converges to zero as time goes to infinity.

Letting $\hat{f} = \hat{k}_e(x - \hat{x}_e)$ be the estimated contact force. Using estimated parameters allows the estimated parameters $\hat{k}_e$ and $\hat{x}_e$ to be updated such that the estimated force converges to real contact force f. The level of convergence is denoted using the error expression between estimated force and real force:

$$\hat{f} - f = \hat{k}_e(x - \hat{x}_e) - k_e(x - x_e) = (\hat{k}_e - k_e)x + (k_e x_e - \hat{k}_e\hat{x}_e) \tag{5.14}$$

Defining $\tilde{k}_e = \hat{k}_e - k_e$ as the estimation error of environment stiffness, the convergence of estimated values to real values is guaranteed if the parameters estimation error converges to zero as time elapses.

Consider the following Lyapunov function candidate:

$$V = \tilde{k}_e^T w_1 \tilde{k}_e + (k_e x_e - \hat{k}_e\hat{x}_e)^T w_2 (k_e x_e - \hat{k}_e\hat{x}_e) \tag{5.15}$$

where w_1 and w_2 are constant positive numbers that make V nonnegative. As presented in [89], if the estimations of $\hat{k}_e$ and $\hat{x}_e$ are updated using the following algorithm, the estimation values will finally converge to the real value of environmental parameters:

$$\dot{\hat{k}}_e = -\frac{1}{w_1} x(\hat{f} - f) \tag{5.16}$$

$$\dot{\hat{x}}_e = \frac{\hat{f} - f}{\hat{k}_e}(\frac{1}{w_1} x\hat{x}_e + \frac{1}{w_2}) \tag{5.17}$$

Then the time derivative of V is expressed as:

$$\dot{V} = 2\tilde{k_e}^T w_1 \dot{\hat{k}}_e - 2(\hat{k}_e \hat{x}_e + \frac{1}{w_2}) \tag{5.18}$$

The constant property of k_e, x_e is used when deriving the derivative of the Lyapunov function. Substituting equations 5.16 and 5.17 into equation 5.18, and simplifying by some algebraic operation, we can reduce equation 5.18 to:

$$\dot{V} = -2(\hat{f} - f)^2 \tag{5.19}$$

which is negative semi-definite. Equations 5.15 and 5.19 indicate that, if update laws in equations 5.16 and 5.17 are applied, the estimation parameters converge to their real values as evolution continues. This implies that the reference force is tracked, since equations 5.9 and 5.11 indicate an optimal trajectory is generated using the estimated values. The resultant adaptive controller schematic is presented in figure 5.2

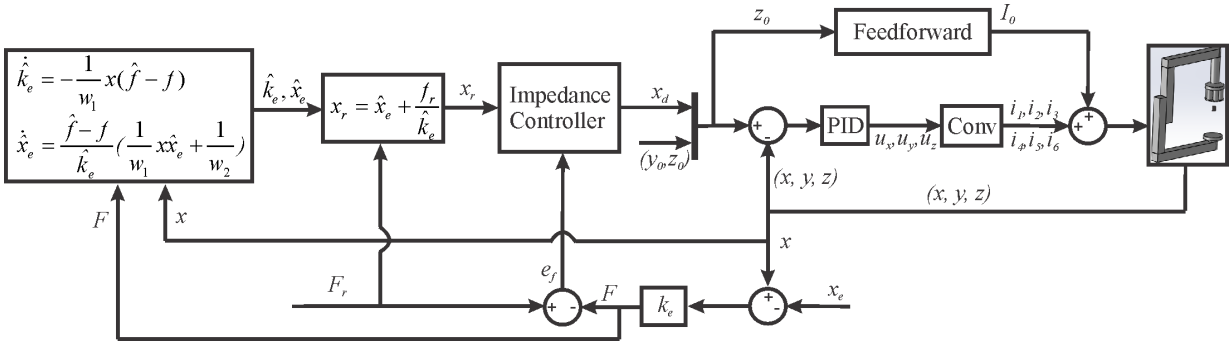

Figure 5.2: Force tracking control system schematic with adaptive environmental parameter estimation and impedance control[111]

5.4 Experimental Validation

In this section, the force tracking performance of the magnetically navigated microrobot using the proposed algorithm is validated experimentally. For the purpose of showing the concept, only one-dimensional force tracking is studied in this paper. Specifically, we study the force tracking in the x-direction relative to the coordinate system shown in figure 2.5. In order to implement the proposed impedance algorithm and the adaptive parameter estimation law on to a digital controller, the equations 5.5, 5.16, and 5.17 are discretized into the discrete time form:

$$\begin{aligned} x_d(n) =&(\frac{m_d}{T^2}+\frac{b_d}{T}+k_d)^{-1}(\frac{m_d}{T^2}(x_r(n-2)-x_d(n-2)) \\ &-(\frac{2m_d}{T^2}+\frac{b_d}{T})(x_r(n-1)-x_d(n-1))-k_f(F(n)-F_r(n)))+x_r(n) \end{aligned} \tag{5.20}$$

$$\hat{k}_e(n) = -\frac{T}{w_1}y(n-1)(\hat{f}(n-1)-f(n-1))+\hat{k}_e(n-1) \tag{5.21}$$

$$\hat{x}_e(n) = T\frac{\hat{f}(n-1)-f(n-1)}{\hat{k}_e(n)}(\frac{1}{w_1}x(n-1)\hat{x}_e(n-1)+\frac{1}{w_2})+\hat{x}_e(n-1) \tag{5.22}$$

where T is the sampling rate of real time system. In this study, the sampling rate was set as $1ms$. n denotes the nth time step.

To demonstrate the performance of the proposed controller, experiments were conducted using the maglev microrobotic system. The first experiment was conducted to validate the force tracking ability of the robot. The microrobot is a cylindric permanent magnet $10mm$ in diameter, $10mm$ in height, and $10.86g$ in weight. The permanent magnet has $1.29T$ remenant magnetic flux density. In this experiment, the microrobot was commanded to push a beam constrained at its two ends (See figure 5.3). The beam was a bent thin 6061 Aluminum alloy sheet $50mm$ in length, $0.051mm$ in thickness, and $3mm$ in width. The exact location and stiffness of the beam are unknown. The experiment was conducted while the microrobot was levitated at $z = 79mm$ below the iron pole-piece. The force tracking performance was validated in the x-direction on the horizontal plane. While in the y-direction, position tracking accuracy is guaranteed. The parameters were chosen to satisfy an over-damped levitation that improved the robustness of navigation. The parameters for the adaptive control law were $w_1 = w_2 = 1$. The initial values of parameters estimation were $k_e = 0.2N/m$ and $x_e = -0.001m$.

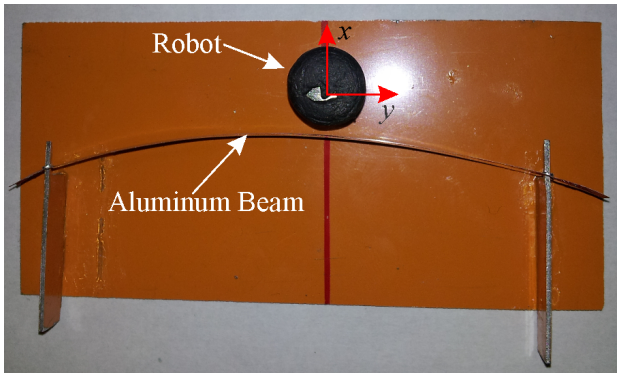

Figure 5.3: Experimental setup for force tracking validation, the two ends of the bended aluminum beam is not fixed[111]

The experimental result is shown in figure 5.4. The experiment was divided into four phases. In the first phase, a very small reference contact force $F_r = 0.01mN$ was assigned to the impedance controller. The purpose of the small reference force was to maintain an initial contact between the navigated microrobot and the unknown surface. In the second phase, a ramp type reference force trajectory was assigned for the microrobot to track. In the third phase, the robot was commanded to move in y-direction, while the maximum commanded contact force was maintained in x-direction. Meanwhile, the controller adjusted the desired x position. In the fourth phase, another ramp type reference force trajectory was assigned for the microrobot to track until the initial $0.01mN$ contact force was obtained again. This experiment demonstrated that the proposed algorithm exhibits good force tracking in the presence of environmental uncertainty. However, it should be noted that there was vibration while the reference force was $0.01mN$. This was because the force was too light to stabilize the beam. In order to clearly show the described procedure, real pictures while the microrobot was working are shown in figure 5.5.

The performance of the controller is related to the parameters of the adaptive control law and the impedance controller. A desired performance is achievable by carefully tuning these parameters. For example, Figure 5.6 shows the effect of the desired impedance damping coefficient on the response speed and overshoot in step force trajectory tracking. Figure 5.6a is the step response with relative small damping $b_d = 5Ns/m$. By comparing with the step response with larger damping $b_d = 20Ns/m$ in figure 5.6b, we can see that small damping results in more overshoot, longer stable time, and more oscillation. The presented technique can be applied to biomedical microsurgery using a MNM. One of the applications is using the microrobot with a very thin blade attached on it to cut delicate tissues. This is a process that does not require a large force compared to $0.5mN$.

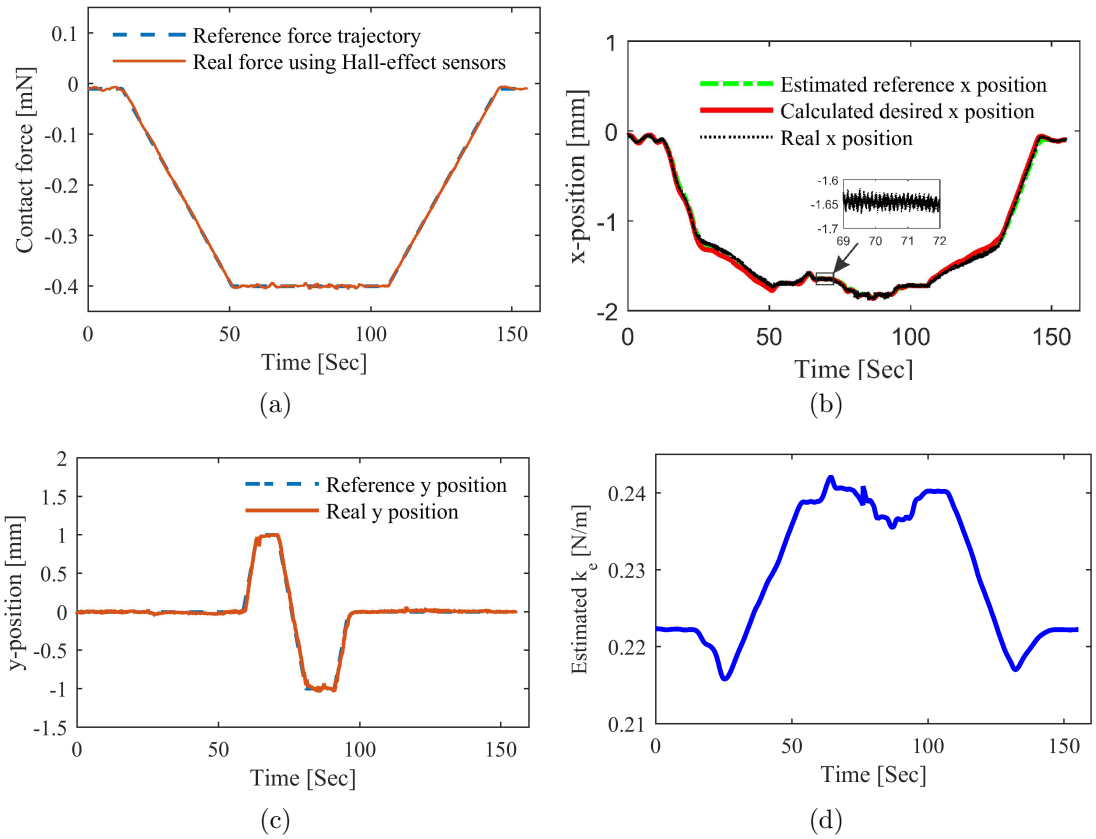

Figure 5.4: Ramp force trajectory tracking performance of the magnetically navigated microrobot[111]

To show the adaptive force tracking performance of the MNM in multi axes, a second experiment which considered the step response of force tracking in the y-direction was conducted. In this experiment, the MNM was navigated to push the same aluminum beam in the first experiment. To start, a small reference force $0.01mN$ guaranteed the initial contact between the MNM and the beam. Then the MNM was commanded to track the step force trajectory. The parameters of the impedance controller in this experiment were set as $m_d = 1Ns^2/m$, $b_d = 20Ns/m$, $k_d = 1.2N/m$, $k_f = 40$. The experiments results are presented in figure 5.7. Figure 5.7a is the force tracking performance. It shows that the adaptive controller provides $1.63\mu N$ force tracking error in steady state. Figure 5.7b shows the motion trajectory of the MNM in the y-direction. The estimated reference y position is obtained from the position estimator in equation 5.11. The calculated desired y position is obtained from the position-based impedance controller. The real y position is obtained

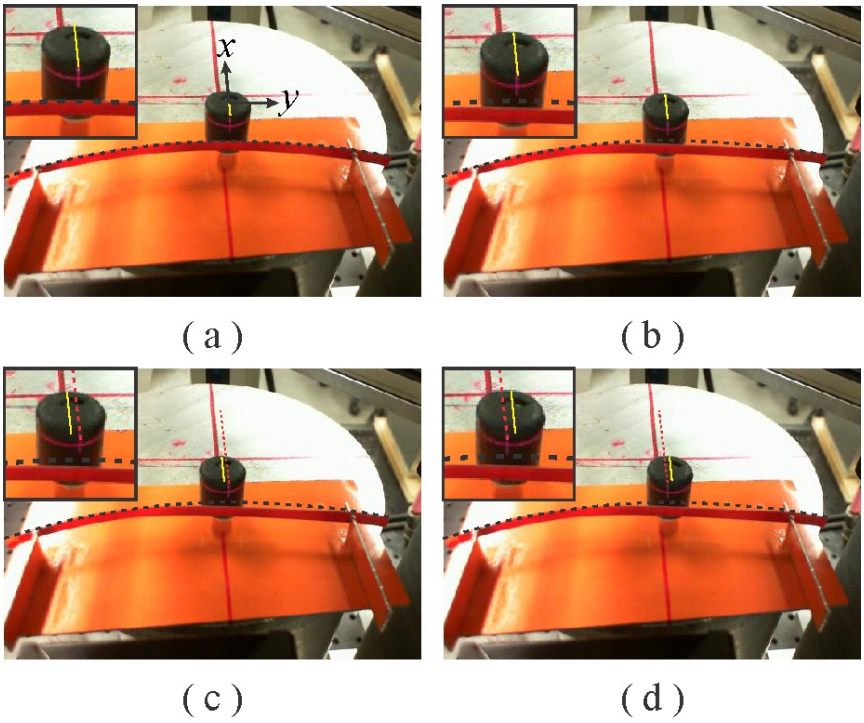

Figure 5.5: The navigated microrobot pushing an Aluminum beam with controlled contact force in x-direction: (a) The microrobot started pushing with $0.01mN$ force; (b) The contact force was set as $0.4mN$; (c) The microrobot was moved to y=1mm while contact force in x-direction was kept as $0.4mN$; (d) The mocrirobot was moved to $y = -1mm$ while contact force in x-direction was kept as $0.4mN$[111]

by reading the laser-beam sensor.

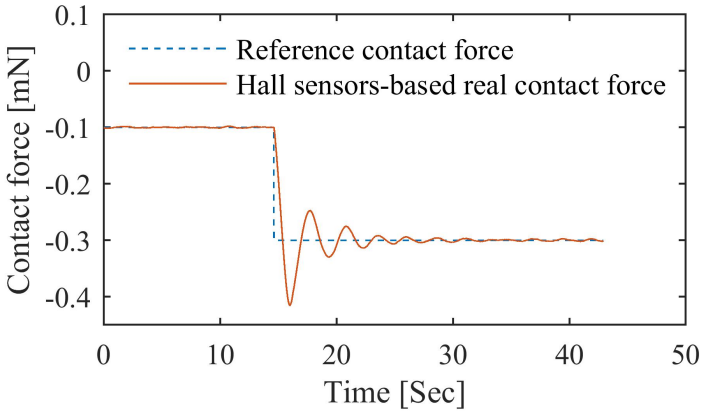

(a)

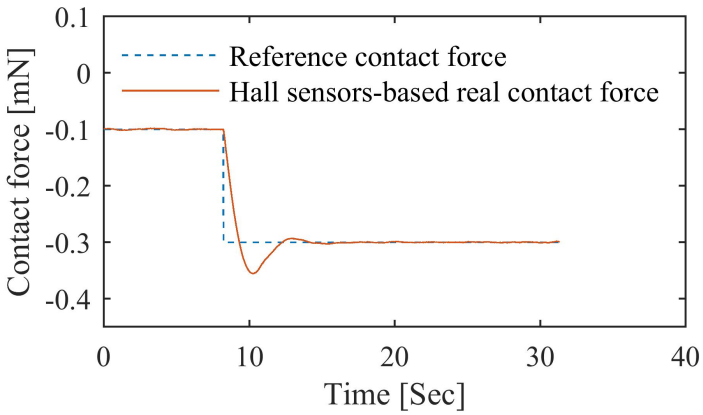

(b)

Figure 5.6: Step response of force tracking with different impedance control damping: (a) $b_d = 5Ns/m$; (b) $b_d = 20Ns/m$[111]

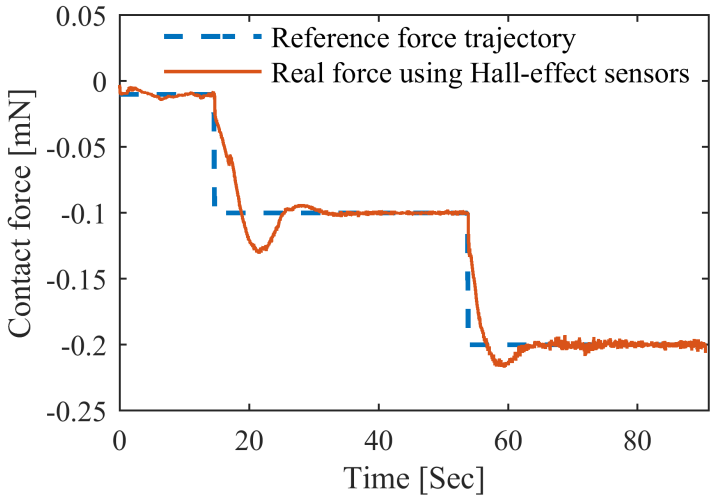

(a)

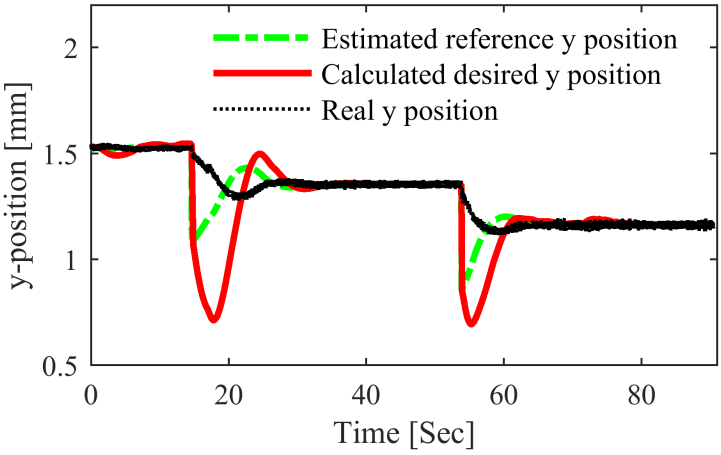

(b)

Figure 5.7: Step response of adaptive force tracking in y-direction: (a) force tracking performance; (b) position trajectories of the MNM in the y-direction. In (b), the calculated desired y position from the position-based impedance controller has relatively larger overshoot. This is because a small k_d was chosen in equation 5.5 for force tracking.[111]

Chapter 6

Conclusion and Recommendation

6.1 Conclusions

This thesis aims to achieve cooperative manipulation using a magnetically navigated microrobot (MNM) and a motorized micromanipulator (MM). This is a new technique that has never been studied in the literature. Although cooperative manipulation using arm-type manipulators has been among popular research topics, it is absolutely new to use an MNM. The MM is a commercialized product with three-degrees-of-freedom translation in a Cartesian coordinate system. The MNM used for the cooperative manipulation is a cylindric permanent magnet with 1.3T remnant magnetic flux density, 10mm diameter, and 10mm height.

The external magnetic field used for levitating a magnetized object in this thesis is generated by six pairs of iron core electromagnets. The electromagnets are connected by a disc shape soft-iron pole piece. The pole-piece not only forms a uniform magnetic field in the workspace, but also increases the strength of the magnetic field significantly. To design a controller for the magnetic levitation, modeling of the magnetic field in the workspace is conducted. Owing to the complexity and high nonlinearity caused by the iron yoke and iron core electromagnets, a closed-form analytical model is very challenging. An experimental measurement data-driven technique was applied to develop the dynamic model of the levitated object in three degrees of freedom. The dynamic model was then used to design PID controllers for high precision motion control. A small permanent magnet (1.3T remnant magnetic flux density) with a 5 millimeter diameter and a 5 millimeter height was levitated to validate the designed controller. An accuracy of 20 μm was obtained in the motion control. However, it was found that a cross coupling effect exists between the

horizontal motion and the vertical motion.

One of the benefits of using a magnetic navigation technique is the remote manipulation of a magnetized object. Therefore, it is a good choice for manipulations in invasive environments. The challenge to realize remote manipulation of the MNM in invasive environments is detecting the real time position of the MNM. In this thesis, we studied the navigation of the MNM in the workspace without using optical/laser beam sensors. The magnetic flux density measurement method was adopted. A set of four Hall-effect sensors was installed at the bottom of the iron pole piece to measure the magnetic flux passing through the workspace. The position of the MNM was mapped into the flux measurement. This technique was applied to navigate the MNM in horizontal planes (2-D degree of freedom) with an accuracy of root mean square error 0.4 mm. This technique is not appropriate for levitation of the MNM in the vertical direction, since the magnetic flux measurement method does not detect the dynamics of the MNM.

It is challenging to install an on-board force sensor to detect the contact force while the MNM is pushing its environment. The magnetic flux measurement using four Hall-effect sensors was used to develop the off-board force determination mechanism. The principle of the off-board force determination mechanism is that the contact force is linearly related to the distance between the location of the B_{max} point and the real position of the MNM. The dual-axial off-board force model was developed and validated on a horizontal plane in the workspace. The force model is validated using two aluminum cantilever beams. Both force models in the x- and the y- directions provide very good accuracy. Specifically, an accuracy of 0.54 μN in the x-direction was obtained. The accuracy of both position and force determinations using magnetic flux measurement is highly related to the performance of the Hall-effect sensors and the accuracy of position detection equipment while the models are calculated.

The proposed cooperative manipulation system has a master/slave control strategy in the manipulation process. The MM was the master side and was commanded the desired location of the manipulated object. The MNM was the slave side. It was commanded a desired holding force while a position-based impedance controller was used to calculated the position command to the MNM. A new force model which considers the moving contact environment of the MNM was derived and implemented in the process. During the cooperative manipulation process, a maximum of 0.4 mN reference holding force was commanded. To monitor the manipulation process and improve the success rate, a CCD camera was introduced in the process to monitor the real time position of the MNM, the MM, and the object. Although some vibration and noise existed, the overall control system provided good performance. The experimental results on both a hard-shell object and a soft-shell object validate the feasibility of the proposed cooperative manipulator. To

further explore its application, multi-degree of position monitoring using a digital camera and multi-degree of off-board force could be adopted. Owing to the limitation of the system setup in this thesis, the shape of the manipulated object is limited regular blocks. In addition, to guarantee the rigid and stable holding, the contact type between manipulators and object should be surface.

The compliant contact force control of an MNM is achieved using the developed off-board force determination mechanism. A position-based impedance controller is suitable for position-controlled manipulators because it enforces a relation between the position and contact force. The compliant motion control of the MNM in uncertain environments was achieved by implementing an adaptive position based impedance controller. The controller estimates the stiffness of the environment and the contact force with Lyapunov asymptotic stability. The force tracking capability of the proposed controller was validated by commanding the MNM to push a thin aluminum beam whose stiffness is unknown. It provides good force tracking results. However, the performance of the controller relies on the choice of impedance controller parameters which determine the response speed and convergence. In addition, the accuracy of the off-board force also significantly affects the tracking results.

6.2 Recommendations

Cooperative manipulation using the MNM and an MM has promising potential in micromanipulation and biomedical applications. A two-degree-of-freedom manipulation was conducted in this thesis. However, much research could be done in the sense of improving the system performance.

First, the force determination mechanism relies on the magnetic flux measurement using Hall-effect sensors. However, the experience in this thesis noticed the poor repeatability of this method owing to the changing of the soft-iron temperature. A perfect force model should take the temperature into account as a factor to compensate for this non-repeatability.

Second, the experimental results in this thesis concludes that a smooth contact force control was obtained if the environment is flexible. When the MNM is touching a hard-shell object, such as the hard-shell object in the cooperative manipulation experiment, force noise and MNM vibration affects tight holding performance. Therefore, future research could be conducted to solve the adaptive holding of objects with various stiffness.

Third, the three-degrees-of-freedom object manipulation is reasonable if more than one digital camera is integrated to provide a real-time position of the manipulated object. By adding more cameras, the contact force between an object and its environment can be achieved, which then facilitates advanced operations, such as peg-in-hole.

Letter of Copyright Permission

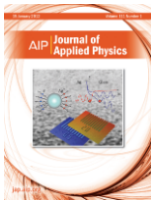

Thank you for your order!

Dear Mr. Xiaodong Zhang,

Thank you for placing your order through Copyright Clearance Center's RightsLink® service.

Order Summary

Licensee:	Mr. Xiaodong Zhang
Order Date:	Sep 30, 2017
Order Number:	4199130665312
Publication:	Journal of Applied Physics
Title:	Diamagnetic levitation: Flying frogs and floating magnets (invited)
Type of Use:	Thesis/Dissertation
Order Total:	0.00 CAD

View or print complete details of your order and the publisher's terms and conditions.

Sincerely,

Copyright Clearance Center

How was your experience? Fill out this survey to let us know.

Tel: +1-855-239-3415 / +1-978-646-2777
customercare@copyright.com
https://myaccount.copyright.com

Springer
the language of science

Thank you for your order!

Dear Mr. Xiaodong Zhang,

Thank you for placing your order through Copyright Clearance Center's RightsLink® service.

Order Summary

Licensee:	Mr. Xiaodong Zhang
Order Date:	Sep 30, 2017
Order Number:	4199130947579
Publication:	Springer eBook
Title:	Magnetically Driven Microrobotics for Micromanipulation and Biomedical Applications
Type of Use:	Thesis/Dissertation
Order Total:	0.00 CAD

View or print complete details of your order and the publisher's terms and conditions.

Sincerely,

Copyright Clearance Center

How was your experience? Fill out this survey to let us know.

Tel: +1-855-239-3415 / +1-978-646-2777
customercare@copyright.com
https://myaccount.copyright.com

Copyright Clearance Center RightsLink®

Springer
the language of science

Thank you for your order!

Dear Mr. Xiaodong Zhang,

Thank you for placing your order through Copyright Clearance Center's RightsLink® service.

Order Summary

Licensee:	Mr. Xiaodong Zhang
Order Date:	Sep 30, 2017
Order Number:	4199130505940
Publication:	Microsystem Technologies
Title:	Motion control of a magnetically levitated microrobot using magnetic flux measurement
Type of Use:	Thesis/Dissertation
Order Total:	0.00 CAD

View or print complete details of your order and the publisher's terms and conditions.

Sincerely,

Copyright Clearance Center

How was your experience? Fill out this survey to let us know.

Tel: +1-855-239-3415 / +1-978-646-2777
customercare@copyright.com
https://myaccount.copyright.com

Copyright Clearance Center RightsLink®

Thank you for your order!

Dear Mr. Xiaodong Zhang,

Thank you for placing your order through Copyright Clearance Center's RightsLink® service.

Order Summary

Licensee:	Mr. Xiaodong Zhang
Order Date:	Sep 30, 2017
Order Number:	4199110281152
Publication:	Robotics and Autonomous Systems
Title:	Control of two manipulation points of a cooperative transportation system with two car-like vehicles following parametric curve paths
Type of Use:	reuse in a thesis/dissertation
Order Total:	0.00 CAD

View or print complete details of your order and the publisher's terms and conditions.

Sincerely,

Copyright Clearance Center

How was your experience? Fill out this survey to let us know.

Tel: +1-855-239-3415 / +1-978-646-2777
customercare@copyright.com
https://myaccount.copyright.com

References

[1] Srg bearing co., ltd, 2015. [Online], Available: http://www.buyskfonline.com/bearingproduct/magnetic xii, 9

[2] Praveen Kumar Agarwal and Satish Chand. Fuzzy logic control of four-pole active magnetic bearing system. In *International Conference on Modeling, Identification and Control*, pages pp. 533–538, 2010. 10

[3] Yasser H. Anis, Holl Mark R, and Deirdre R. Meldrum. Automated selection and placement of single cells using vision-based feedback control. *IEEE/ASME Transactions on Automation Science and Engineering*, Vol. 7:pp.598–606, 2010. 84

[4] Ferreira Antoine, Jol Agnus, Nicolas Chaillet, and J-M. Breguet. A smart microrobot on chip: design, identification, and control. *IEEE/ASME Transactions on Mechatronics*, Vol. 9:pp.508–519, 2004. 84

[5] Sylvain Arlot and Alain Celisse. A survey of cross-validation procedures for model selections. *Statistics Surveys*, Vol.4:pp. 40–79, 2010. 55

[6] Marcin Balicki, Tian Xia, Min Yang Jung, Anton Deguet, and Balazs Vagvolgyi. Prototyping a hybrid cooperative and telerobotic surgical system for retinal microsurgery. *The MIDAS Journal-Systems and Architectures for Computer Assisted Interventions*, 2011(815). 2

[7] Todd D. Batzel and Kwang Y. Lee. Slotless permanent magnet synchronous motor operation without a high resolution rotor angle sensor. *IEEE Transactions on Energy Conversion*, Vol. 15(4):pp. 366–371, 2000. 47

[8] Magnus Bjerkeng, Johannes Schrimpf, Torstein Myhre, and Kristin Y. Pettersen. Fast dual-arm manipulation using variable admittance control: Implementation and experimental results. In *IEEE/RSJ International Conference on Intelligent Robotsccc and Systems*, Chicag, IL, USA, 2014. 2

[9] Robert G. Bonita and T. C. Hsia. Internal force-based impedance control for cooperating manipulators. *IEEE Transactions on Robotics and Automation*, Vol. 12(1):pp. 78–89, February 1996. 4, 71, 73

[10] Robert G. Bontiz and T.C. Hsia. Force decomposition in cooperating manipulators using the theory of metric spaces and generalized inverses. In *IEEE International Conference on Robotics and Automation 1994 Proceedings*, pages pp. 1521–1527, 1994. 74

[11] Fabrizio Caccavale, Pasquale Chiacchio, Alessandro Marino, and Luigi Villani. Six-dof impedance control of dual-arm cooperative manipulators. *IEEE Transactions on Mechatronics*, Vol. 13(5):pp. 576–586, October 2008. xii, 2, 4

[12] L. M. Capisani and A. Ferrara. Trajectory planning and second-order sliding mode motion/interaction control for robot manipulators in unknown environment. *IEEE Transactions on Industrial Electronics*, Vol. 59:pp.3189–3198, 2012. 97

[13] Federico Carpi, Nathan Kastelein, Michael Talcott, and Carlo Pappone. Magnetically controllable gastrointestinal steering of video capsules. *IEEE Transactions on BioMedical Engineering*, Vol. 58(2):pp. 231–234, 2010. 47

[14] Federico Carpi, Nathan Kastelein, Michael Talcott, and Carlo Pappone. Magnetically controllable gastrointestinal steering of video capsule. *IEEE Transactions on Biomedical Engineering*, Vol. 58(2):pp. 231–234, 2011. 5

[15] S. P. Chan and H. C. Liaw. Generalized impedance control of robot for assembly tasks requiring compliant manipulation. *IEEE Transactions on Industrial Electronics*, Vol. 43:pp.453–461, 1996. 79

[16] Hung-Cheng Chen and Sheng-Hsing Chang. Genetic algorithm based optimization design of a pid controller for an active magnetic bearing. *International Journal of Computer Science and Network Security*, Vol. 6(12):pp. 95–99, 2006. 10

[17] Mei-Yung Chen, Tzuo-Bo Lin, Shao-Kang Hung, and Li-Chen Fu. Design and experiment of a macro-micro planar maglev positioning system. *IEEE Transactions on Industrial Electronics*, Vol. 59(11):pp. 4128–4139, 2012. 11

[18] S. Y. Chen, Jianwei Zhang, Houxiang Zhang, N. M. Kwok, and Y. F. Li. Intelligent lighting control for vision-based robotic manipulation. *IEEE/ASME Transactions on Industrial Electronics*, Vol. 59:pp.3254–3263, 2012. 84

[19] Seng-Chi Chen, Van-Sum Nguyen, Dinh-Kha Le, and Ming-Mao Hsu. Anfis controller for an active magnetic bearing system. In *IEEE International Conference on Fuzzy Systems (FUZZ)*, pages pp. 1–8, 2013. 10

[20] Shyh-Leh Chen. Nonlinear smooth feedback control of a three-pole active magnetic bearing system. *IEEE Transactions on Control System Technology*, Vol. 19(3):pp. 615–621, 2011. 10

[21] Shyh-Leh Chen and Chan-Tang Hsu. Optimal design of a three-pole active magnetic bearing. *IEEE Transactions on Magnetics*, Vol. 38(5):pp. 3458–3466, 2002. 10

[22] Syuan-Yi Chen and Faa-Jeng Lin. Robust nonlinear terminal sliding-mode control for nonlinear magnetic bearing system. *IEEE Transactions on Control System Technology*, Vol. 19(3):pp. 636–643, 2011. 10

[23] H. Chetouani, C. Jeandey, V. Haguet, H. Rostaing, C. Dieppedale, and G. Reyne. Diamagnetic levitation with permanent magnets for contactless guiding and trapping of microdroplets and particles in air and liquids. *IEEE/ASME Transactions on Magnetics*, Vol. 42:pp.3557–3559, 2006. 7

[24] P-Y. Couzon and J. Der Hagopian. Neuro-fuzzy active control of rotor suspended on active magnetic bearing. *Journal of Vibration and Control*, Vol. 13(4):pp. 365–384, 2007. 10

[25] Eugene E. Covert, Morton Finston, Milan Vlajinac, and Timothy Stephens. Magnetic balance and suspension systems for use with wind tunnels. *Progress in Aerospace Sciences*, Vol. 14:pp. 27–94, 1973. 5

[26] G. Duchemin, P. Maillet, P. Poignet, E. Dombre, and F. Pierrot. A hybrid position/-force control approach for identification of deformation models of skin and underlying tissues. *IEEE Transactions on Biomedical Engineering*, Vol. 52:pp.160–169, 2005. 97

[27] C. Elbuken, M. B. Khamesee, and M. Yavuz. Design and implementation of a micro-manipulation system using a magnetically levitated mems robot. *IEEE Transactions on Mechatronics*, Vol. 14:pp.434–445, 2009. xii, 13, 14, 98

[28] S. Erhart and S. Hirche. Internal force analysis and load distribution for cooperative multi-robot manipulation. *IEEE Transactions on Robotics*, Vol. 31:pp. 1238–1243, 2015. 71

[29] Jiancheng Fang, Yun Le, Jinji Sun, and Kun Wang. Analysis and design of passive magnetic bearing and damping system for high-speed compressor. *IEEE Transactions on Magnetics*, Vol. 48(9):pp. 2528–2537, 2012. 10

[30] L. F.C. Figueredo, B. V. Adorno, J. Y. Ishihara, and G. A. Borges. Switching strategy for flexible task execution using cooperative dual task-space framework. In *IEEE/RSJ International Conference on Intelligent Robotscccc and Systems*, Chicag, IL, USA, 2014. 1

[31] Jonathan Fink, Nathan Michael, Soonkyum Kim, and Vijay Kumar. Planning and control for cooperative manipulation and transportation with aerial robots. *The International Journal of Robotics Research*, 30:pp. 324–334, 2011. 1

[32] Antonio Franchi, Antonio Petitti, and Alessandro Rizzo. Distributed estimation of the inertial parameters of an unknown load via multi-robot manipulation. In *53rd IEEE Conference on Decision and Control*, Los Angeles, CA, 2014. 4

[33] Yamato Fukuta, Yves-Andre Chapuis, Yoshio Mita, and Hiroyuki Fujita. Design, fabrication, and control of mems-based actuator arrays for air-flow distributed micromanipulation. *Journal of Microelectromechanical System*, Vol. 15(4):pp. 912–926, 2006. 5

[34] W. Gueaieb, F. Karray, and A. S. Salah. A robust hybrid intelligent position/force control scheme for cooperative manipulation. *IEEE/ASME Transactions on Mechatronics*, Vol. 12:pp. 109–125, 2007.

[35] Wail Gueaieb, Fakhri Karray, and Salah Al-Sharhan. A robust adaptive fuzzy position/force control scheme for cooperative manipulators. *IEEE Transactions on Control Systems Technology*, Vol. 11(4):pp. 516–528, July 2003. 3, 4, 71

[36] Jan D. J. Gumprecht, Tim C. Lueth, and Mir Behrad Khamesee. Navigation of a robotic capsule endoscope with a novel ultrasound tracking system. *Microsystem Technology*, Vol. 19:pp. 1415–1423, 2013. 47, 98

[37] Shuxiang Guo, Qinxue Pan, and Mir Behrad Khamesee. Development of a novel type of microrobot for biomedical application. *Microsystem Technology*, Vol. 14:pp. 307–314, 2008. 12

[38] Youguang Guo, Jian Xun Jin, Jian Guo Zhu, and Hai Yan Lu. Design and analysis of a prototype linear motor driving system for hts maglev transportation. *IEEE Transactions on Applied Superconductivity*, Vol. 17(2):pp. 2087–2090, 2007. 5

[39] A. Hamler, V. Gorican, B. STumberger, M. Jesenik, and M. Trlep. Passive magnetic bearing. *Journal of Magnetism and Magnetic Materials*, Vol. 272-276(3):pp. 2379–2380, 2004. 10

[40] D. Heck, D. Kostic, A. Denasi, and H. Nijmeijer. Internal and external force-based impedance control for cooperative manipulation. In *European Control Conference*, 2013. 72

[41] B. Heinrichs, S. Nariman, and A. B. Thornton-Trump. Position-based impedance control of an industrial hydraulic manipulator. *IEEE Control System*, Vol. 17:pp. 46–52, 1997. 79

[42] N. Hogan. Impedance control: An approach to manipulation: Part ii- implementation. *Journal of Dynamic System, Measurement, and Control*, Vol. 7:pp.8–16, 1985. 97

[43] Saman Hosseini, Moein Mehrtash, and Mir Behrad Khamesee. Design, fabrication and control of a magnetic capsule-robot for the human esophagus. *Microsystem Technology*, Vol. 17:pp. 1145–1152, 2011. 12

[44] Haibo Huang, Dong Sun, James K. Mills, and Shuk Han Cheng. Robotic cell injection system with position and force control: Toward automatic batch biomanipulation. *IEEE/ASME Transactions on Robotics*, Vol. 25:pp.727–737, 2009. 84

[45] L. Huang, S. S. Ge, and T. H. Lee. An adaptive impedafnce control scheme for constrained robots. *International Journal of Computers, Systems, and Signals*, Vol. 5:pp.17–26, 2004. 98

[46] G. Hwang, P. T. Szemes, N. Ando, and H. Hashimoto. Development of a single-master multi-slave tele-micromanipulation system. *Advanced Robotics*, Vol. 21:pp. 329–349, 2007.

[47] I. Iordachita, Z. Sun, M. Balicki, J. U. Kang, S. J. Phee, J. Handa, P. Gehlback, and R. Taylor. A sub-millimetric, 0.25mn resolution fully integrated fiber-optic force-sesing tool for retinal microsurgery. *International Journal of Computer Assisted Radiology and Surgery*, Vol. 4:pp.383–390, 2009. 97

[48] Tatsuzo Ishida. Force control in coordination of two arms. In *Proceedings of 5th International on Artificial Intelligence*, pages pp. 717–722, 1977. 3

[49] Li Ji, Longxiang Xu, and Chaowu Jin. Research on a low power consumption six-pole heteropolar hybrid magnetic bearing. *IEEE Transactions on Magnetics*, Vol. 49(8):pp. 4918–4926, 2013. 10

[50] M. Jian, J. Tal, Y. S. Luh, and Y. F. Zheng. Compliant coordination control of two moving industrial robots. *IEEE Transactions on Robotics and Automation*, Vol. 6:pp. 186–191, 1990. 71

[51] Qimi Jiang and Vijay Kumar. The inverse kinematics of cooperative transport with multiple aerial robots. *IEEE Transactions on Robotics*, Vol. 29(1):pp. 136–145, February 2013. xii, 1, 2

[52] S. Jung and Hsia T. C. Robust neural force control scheme under uncertainties in robot dynamics and unknown environment. *IEEE Transactions on Industrial Electronics*, Vol. 47:pp.403–412, 2000. 98

[53] S. Jung, Hsia T. C, and R. G. Bonitz. Force tracking impedance control of robot manipulation under unknown environment. *IEEE Transactions on Control Systems Technology*, Vol. 12:pp.474–483, 2004. 98

[54] Mir Behrad Khamesee, Norihiko Kato, Yoshihiko Nomura, and Tatsuya Nakamura. Design and control of a microrobotic system using magnetic levitation. *IEEE/ASME Transactions on Mechatronics*, Vol. 7(1):pp. 1–14, 2002. 12, 25, 98

[55] Mir Behrad Khamesee and Ehsan Shameli. Pole piece effect on improvement of magnetic controllability for non-contact micromanipulation. *IEEE Transactions on Biomedical Engineering*, Vol. 43(2):pp. 533–542, 2007. 25

[56] Ha-Yong Kim and Chong-Won Lee. Design and control of active magnetic bearing system with lorentz force-type axial actuator. *Mechatronics*, Vol. 16:pp. 13–20, 2006. 5

[57] Won-Jong Kim, David L. Trumper, and Jeffrey H. Lang. Modeling and vector control of a planar magnetic levitator. In *IEEE Industry Applications Conference*, pages pp. 349–356, 1997. 11

[58] S. Kudoh, K. Ogawara, M. Ruchanurucks, and K. Ikeuchi. Painting robot with multi-fingered hands and stereo vision. *Robotics and Autonomous Systems*, Vol. 57:pp.279–288, 2009. 97

[59] Michael P. Kummer, Jake J. Abbott, Bradley E. Kratochvil, Ruedi Borer, Ali Sengul, and Bradley J. Nelson. Octomag: An electromagnetic system for 5-dof wireless micromanipulation. *IEEE Transactions on Robotics*, Vol. 26(6):pp. 1006–1017, 2010. xii, 9, 12, 98

[60] Hyung-Woo Lee, Ki-Chan Kim, and Ju Lee. Review of maglev train technologies. *IEEE Transactions on Magnetics*, Vol. 42(7):pp. 1917–1925, 2006. 5

[61] Kaite A. Lilienkamp and Kent Lundberg. Low-cost magnetic levitation project kits for teaching feedback system design. In *American Control Conference*, pages pp. 1308–1313, 2004. 55

[62] H. Lim, A. S. Samuel, and A. Takanishi. Position-based impedance control of a biped humanoid robot. *Advanced Robotics*, Vol. 18:pp.415–435, 2004. 79

[63] Zhi Liu, Ci Chen, Yun Zhang, and C. L. Philip Chen. Coordinated fuzzy control of robotic arms with actuator nonlinearities and motion constraints. *Information Science*, Vol. 296(1):pp. 1–13, March 2015. 1

[64] A. Lopes and F. Almeida. A force-impedance controlled industrial robot using an active robotic auxiliary device. *Robotics and Computer Integrated Manufacturing*, Vol. 24:pp.299–309, 2008. 97

[65] I. F. Lyuksyutov, D. G. Naugle, and K. D. D. Rathnayaka. On-chip manipulation of levitated femtodroplets. *Applied Physics Letters*, Vol. 85(10):pp. 1817–1819, 2004. 6, 7

[66] V. Mallapragada, D. Erol, and N. Sarkar. A new method of force control for unknown environments. In *Proceedings of the IEEE/RSJ International Conference on Intelligent Robots and Systems*, 2006. 98

[67] S. Martel, J-B. Mathieu, O. Felfoul, A. Chanu, E. Aboussouan, S. Tamaz, P. Pouponneau, L. Tahia, G. Beaudoin, G. Soulez, and M. Mankiewicz. Automatic navigation of an untethered device in the artery of a living animal using a conventional clinical magnetic resonance imaging system. *Applied Physics Letters*, Vol. 90:pp.114105–1–114405–3, 2007. 98

[68] Ignacio Mas and Christopher Kitts. Object manipulation using cooperative mobile multi-robot systems. In *Proceedings of the World Congress on Engineering and Computer Science*, San Francisco, USA, Oct. 2012. 2

[69] Uchiyama Masaru, Naotoshi Iwasawa, and Kyojiro Hakomori. Hybrid position/force control for coordination of a two-arm robot. In *IEEE International Conference on Robotics and Automation*, volume 4, pages 1242–1247, 1987. 3

[70] Koichi Matsuda, Yoichi Kanemitsu, and Shinya Kijimoto. Optimal number of stator poles for compact active radial magnetic bearings. *IEEE Transactions on Magnetics*, Vol. 43(8):pp. 3420–3427, 2007. 10

[71] M. Mehrtash, X. Zhang, and M. B. Khamesee. Bilateral magnetic micromanipulation using off-board force sensor. *IEEE/ASME Transactions on Mechatronics*, Vol. 20:pp.3223–3231, 2015. 78, 98, 99

[72] Moein Mehrtash and Mir Behrad Khamesee. Design and implementation of lqg / ltr controller for a magnetic telemanipulation system-performance evaluation and energy saving. *Microsystem Technologies*, pages pp. 1135–1143, 2011. 44

[73] Moein Mehrtash and Mir Behrad Khamesee. Micro-domain force estimation using hall-effect sensors for a magnetic microrobotic station. *Journal of Advanced Mechanical Design, Systems, and Manufacturing*, Vol. 7:pp. 2–14, 2013.

[74] Moein Mehrtash, Mir Behrad Khamesee, Naoaki Tsuda, and Jen-Yuan Chang. Motion control of a magnetically levitated microrobot using magnetic flux measurement. *Microsystem Technology*, Vol. 18:pp. 1417–1424, 2012. xiv, 13, 48, 50, 51

[75] Moein Mehrtash, Naoaki Tsuda, and Mir Behrad Khamesee. Bilateral macro-micro teleoperation using magnetic levitation. *IEEE/ASME Transactions on Mechatronics*, Vol. 16:pp. 459–469, 2011. 48

[76] Nathan Michael, Jonathan Fink, and Vijay Kumar. Cooperative manipulation and transportation with aerial robots. In *Proceedings of Robotics: Science and Systems*, Seattle, USA, June 2009. 2

[77] Muneaki Miyasaka and Peter Berkelman. Magnetic levitation with unlimited omnidirectional rotation range. *Mechatronics*, Vol. 24(3):pp. 252–264, 2014. 12

[78] Tatsuya Nakamura and Mir Behrad Khamesee. A prototype mechanism for three-dimensional levitated movement of a small magnet. *IEEE/ASME Transactions on Mechatronics*, Vol. 2(1):pp. 41–50, 1997. 5

[79] Eiji Nakano and Shotaro Ozaki. Cooperational control of the anthropomorphous manipulator 'melarn'. In *Proceedings of the 4th International Symposium on Industrial Robots*, pages 251–260, Tokyo Japan, 1974. 3

[80] Vu Huy Nguyen and Won jong Kim. Design and control of a compact lightweight planar positioner moving over a concentrated-field magnetic matrix. *IEEE/ASME Transactions on Mechatronics*, Vol. 18(3):pp. 1090–1099, 2013. 11

[81] Motoharu Ono, Shunsaku Koga, and Hisao Ohtsuki. Japans superconducting maglev train. *IEEE Instrumentation and Measurement Magazine*, Vol. 5(1):pp. 9–15, 2002. 6, 8

[82] Vikas Panwar, Naveen Kumar, N. Sukavanam, and Jin-Hwan Borm. Adaptive neural controller for cooperative multiple robot manipulator system manipulating a single rigid object. *Applied Soft Computing*, Vol. 512:pp. 216–227, 2012. 4

[83] Jose Luis Perez-Diaz, Ignacio Valiente-Blanco, Efren Diez-Jimenez, and Juan Sanchez-Garcia-Casarrubios. Superconducting noncontact device for precision positioning in cryogenic environments. *IEEE/ASME Transactions on Mechatronics*, Vol. 19(2):pp. 598–605, 2014. 6, 8

[84] Marc H. Raibert and John J. Craig. Hybrid position/force control of manipulators. *Journal of Dynamic Systems, Measurement, and Control*, Vol. 103(2):pp. 126–133, 1981. 3

[85] Alexandre Schammass, Raoul Herzog, Philioo Buhler, and Hannes Bleuler. New results for self-sensing active magnetic bearings using modulation approach. *IEEE Transactions on Control System Technology*, Vol. 13(4):pp. 509–516, 2005. 10

[86] Stanley A. Schneider and Robert H. Cannon. Object impedance control for cooperative manipulation: Theory and experimental results. *IEEE Transactions on Robotics and Automation*, Vol. 8(3):pp. 383–394, June 1992. 4

[87] Christian Schott, Robert Racz, Fredy Betschart, and Radivoje S. Popovic. A new two-axis magnetic position sensor. In *Proceeding IEEE Sensors*, pages pp. 911–915, 2002. 47

[88] Ludwig Schultz, Oliver de Haas Verges, Christoph Beyer, Steffen Rohlig, Henning Olsen, Lars Kuhn, Dietar Berger, Ulf Noteboom, and Ullrich Funk. Superconductively levitated transport system-the supratrans project. *IEEE Transactions on Applied Superconductivity*, Vol. 15(2):pp. 2301–2305, 2005. xii, 6

[89] H. Seraji and R. Colbaugh. Force tracking in impedance control. *The International Journal of Robotics Research*, Vol. 16:pp.97–117, 1997. 98, 102

[90] Huzefa Shakir and Won-Jong Kim. Nanoscale path planning and motion control with maglev positioners. *IEEE/ASME Transactions on Mechatronics*, Vol. 11(5):pp. 625–633, 2006. xii, 9, 11

[91] Ehsan Shameli. Design, implementation and control of a magnetic levitation device. *University of Waterloo PhD Thesis*, 2008. 21

[92] Ehsan Shameli, David G. Craig, and Mir Behrad Khamesee. Design and implementation of a magnetically suspended microrobotic pick-and-place system. *Journal of Applied Physics*, 99(8), 2006. 12

[93] Mark Siebert, Ben Ebihara, and Ralph Jansen. A passive magnetic bearing flywheel. In *36th Intersociety Energy Conversion Engineering Conference*, 2001. 10

[94] M. D. Simon and A. K. Geim. Diamagnetic levitation: Flying frogs and floating magnets (invited). *Journal of Applied Physics*, Vol. 87(9):pp. 6200–6204, 2000. xii, 6, 7

[95] Glauco R. Souza, Jennifer R. Molina, Robert M. Raphael, Michael G. Ozawa, Danel J. Stark, Carly S. Levin, Lawrence F. Bronk, and Jeyarama S. Ananta. Three-dimensional tissue culture based on magnetic cell levitation. *Nature Nanotechnology*, Vol. 5:pp. 291–296, 2010. 5

[96] M. Strasik, P. E. Johnson, A. C. Day, J. Mittleider, M. D. Higgins, J. Edwards, J. R. Schindler, K. E. McCrary, C. R. McIver, D. Carlson, Gonder J. F, and J. R. Hull. Design, fabrication, and test of a 5-kwh/100-kw flywheel energy storage utilizing a high-temperature superconducting bearing. *IEEE Transactions on Applied Superconductivity*, Vol. 17(2):pp. 2133–2137, 2007. 5

[97] B. Tamadazte, E. Marchand, S. Dembele, and N. Le Fort-Piat. model-based tracking and 3d visual-based control for mems microassembly. *The International Journal of Robotics Research*, Vol. 29:pp.1416–1434, 2010. 84

[98] David L. Trumper, Sean M. Olson, and Pradeep K. Subrahmanyan. Linearizing control of magnetic suspension systems. *IEEE Transactions on Control Systems Technology*, Vol. 5(2):pp. 427–438, 1997. 47

[99] Yoshikawa Tsuneo and Xin-Zhi Zheng. Coordinated dynamic hybrid position/force control for multiple robot manipulators handling one constrained object. *The International Journal of Robotics Research*, Vol. 12(3):pp. 219–230, 1993. 3

[100] H. Wang, K. H. Low, and M. Y. Want. Reference trajectory generation for force tracking impedance control by using neural network-based environment estimation. In *IEEE Conference on Robotics, Automation and Mechatronics*, 2006. 98

[101] Sheng-He Wang and Mi-Ching Tsai. Implementation and analysis of noncontact acoustic tweezers using quasi-standing waves. *IEEE/ASME Transactions on Mechatronics*, Vol. 18(3):pp. 1019–1026, 2013. 5

[102] Zongyao Wang and Dongbing Gu. Cooperative target tracking control of multiple robots. *IEEE Transactions on Industrial Electronics*, Vol. 59(8):pp. 3232–3240, August 2012. 1

[103] Y. Xie, D. Sun, and C. Liu. A force control approach to a robot-assisted cell microinjection system. *The International Journal of Robotics Research*, Vol. 29:pp.1222–1232, 2010. 97

[104] Fengqiu Xu, Xianze Xu, Zhongbing Li, and Liang Chu. Numerical calculation of the magnetic field and force in cylindrical single-axis actuator. *IEEE Transactions on Magnetics*, Vol. 50(10), 2014. 11

[105] Q. Xu. Precision position/force interaction control of a piezoelectric multimorphmicrogripper for microassembly. *Transactions on Automation Science and Engineering*, Vol. 10:pp.503–514, 2013. 79

[106] Hiroaki Yamaguchi, Ai Nishijima, and Atsushi Kawakami. Control of two manipulation points of a cooperative transportation system with two car-like vehicles following parametric curve paths. *Robotics and Autonomous Systems*, Vol. 63:pp. 165–178, January 2015. 1, 2

[107] Mitsuhiro Yamano, Jin-Soo Kim, and Masaru Uchiyama. Hybrid position/force control for two cooperative flexible manipulators working in 3d space. In *IEEE International Conference on Robotics and Automation*, Leuven, Belgium, May 1998. 3

[108] Sheng-Ming Yang and Chien-Lung Huang. A hall sensor-based three-dimensional displacement measurement system for miniature magnetically levitated rotor. *IEEE Sensors Journal*, Vol. 9(12):pp. 1872–1878, 2009. 47

[109] P-L Yen and B. L. Davies. Active constraint control for image-guided robotic surgery. In *Proceeding of the Institution of mechanical engineering*, 2010. 97

[110] Wen Yu and Xiaoou Li. A magnetic levitation system for advanced control education. In *The InternationalFederation of Automatic Control*, pages pp. 9032–9037, 2014. 5

[111] X. Zhang and M. B. Khamesee. Adaptive force tracking control of a magnetically navigated microrobot in uncertain environments. *IEEE/ASME Transactions on Mechatronics*, DOI: 10.1109/TMECH.2017.2705523, 2017. xv, xvii, 70, 102, 104, 105, 106, 107, 108

[112] X. Zhang, M. Mehrtash, and M. B. Khamesee. Dual-axial motion control of a magnetic levitation system using hall-effect sensors. *IEEE/ASME Transactions on Mechatronics*, Vol. 21:pp.1129–1139, 2016. xii, xiii, xiv, 23, 48, 49, 50, 51, 54, 56, 57, 59, 60, 61, 62

[113] Xiaodong Zhang and Behrad Khamesee. *Advanced Mechatronics and MEMS Devices II*, chapter Magnetically driven microrobotics for micromanipulation and biomedical applications. Springer International Publishing, 2017. xii, xiii, 21, 26, 27, 29

[114] Haiyue Zhu, Tat Joo Teo, and Chee Khiang Pang. Conceptual design and modeling of a six degree-of-freedom unlimited stroke magnetically levitated positioner. In *IEEE/ASME International Conference on Advanced Intelligent Mechatronics (AIM)*, pages pp. 1569–1574, 2014. 11

Appendix A - List of Publications

1 Zhang, Xiaodong, Moein Mehrtash, and Mir Behrad Khamesee. "Dual-axial motion control of a magnetic levitation system using hall-effect sensors." IEEE/ASME Transactions on Mechatronics 21.2 (2016): 1129-1139.

2 Zhang, Xiaodong, and Mir Behrad Khamesee. "Adaptive force tracking control of a Magnetically Navigated Microrobot in Uncertain Environments." IEEE/ASME Transactions on Mechatronics 22.4 (2017): 1644-1651.

3 Zhang, Xiaodong, and Mir Behrad Khamesee. "Magnetically Driven Microrobotics for Micromanipulation and Biomedical Applications." Advanced Mechatronics and MEMS Devices II. Springer International Publishing, 2017. 613-635.

4 Zhang, Xiaodong, and Mir Behrad Khamesee. "Modeling and Motion Control of a Magnetically Navigated Microrobotic System." Proceedings of the 3rd International Conference on Control, Dynamic Systems, and Robotics (CDSR16) Ottawa, Canada, May 9-10, 2016